ScuDo
Scuola di Dottorato ∽ Doctoral School
WHAT YOU ARE, TAKES YOU FAR

Doctoral Dissertation
Doctoral Program in Energetics (29thcycle)

Analysis of injection, mixture formation and combustion processes for innovative CNG Engines

By

Ludovico Viglione

******

Supervisor(s):
Prof. Daniela Misul
Prof.Mirko Baratta

Doctoral Examination Committee:

Politecnico di Torino
2017

Declaration

I hereby declare that, the contents and organization of this dissertation constitute my own original work and does not compromise in any way the rights of third parties, including those relating to the security of personal data.

Ludovico Viglione
2017

* This dissertation is presented in partial fulfillment of the requirements for **Ph.D. degree** in the Graduate School of Politecnico di Torino (ScuDo).

Acknowledgements

I would like to thank all the research group of Prof. Ezio Spessa for the possibility they gave me.
In particular I wish to express all my gratitude to my supervisors Prof. Daniela Misul and Prof. Mirko Baratta; It has been an honour working with them throughout my Ph.D. both professionally and personally.
I am also grateful to Dr. Juergen Schneider (AVL List GmbH) for the interesting discussion and his valuable help in understanding the software ’AVL FIRE^{TM}’.
My acknowledge goes to all the colleagues that worked with me during my research project: Ing. Sergio Tosi, Ing. Juan San Primitivo, Ing. Jaijie Xu, and to the Politecnico staff.
My gratitude also goes to the graduate students Giuseppe Scaldaferri, Giorgio De Costanzi and Paolo De Angelis, I really appreciate their valuable and fair contribution to the work.
A special thanks goes to Ing. Samir Kumar and Ing. Prashant Goel their support went far beyond the technical help, I found true friends that supported me during the writing of this thesis. I want to express my gratitude to my girlfriend Ilaria Scavuzzo because she supported me during this Ph.D. and tolerated all my frustration relate to the job.
Last but not least I express all the gratitude to all my family that always supported me, in particular I would mention my uncle Antonio Viglione that helped me since the beginning of my university career.

Abstract

Natural gas is a promising alternative fuel for internal combustion engines application due to its low carbon content and high knock resistance. The work presented in this thesis deals with the fluid dynamics, experimental study and optimization of different technologies aimed at exploiting the potentials of such fuel at best. The first section of the work is aimed at the combustion chamber optimization with the focus on the combustion stability. The engine considered in the study is a prototype specifically dedicated to CNG. It features a variable valve actuation system and has been released with different and very high compression ratios ranging from 12 to 14. An innovative experimental methodology based on hot wire anemometry (HWA) purposely developed by Centro Ricerche Fiat (CRF) has been adopted for the characterization of the steady-state tumble. The HWA method has been validated against the well-known Ricardo method and is used as a basis for the development and validation of a numerical "virtual flow bench". The numerical model has been used to gain a deeper insight into the fluid dynamic phenomena and to replace the experimental campaign considering a head variant and quantifying its tumbling and volumetric performances. A transient 3D CFD analysis for the complete engine cycle has been performed in order to evaluate the effect on the combustion process of different compression ratios and head designs.The results showed that the HWA technique represents a factual alternative to the integral technique for the tumble characterization. The "Virtual flow box" model turned out to be accurate enough to evaluate the main flow motions induced by the head design and to be a valid tool complementary to the experimental method. Finally, the transient model used in combination with the ECFM-3z combustion model is fairly accurate for the comparative analysis between different engine designs and/or valve actuations.

Despite the main findings of the flow model activity, importance should also be placed onto advanced technologies for natural gas engines such as direct injection. Thus, the second section is aimed at the numerical study of a natural gas direct injection engine. The numerical complexity caused by the high pressure ratio at nozzle exit has been faced using an accurate mesh procedure able to correctly capture the formation of shocks structures. Moreover, the actual needle geometry and the realistic needle movement has been taken into account in order to correctly simulate the opening and closing transient. The final mix and turbulence level has been evaluated comparing two engine prototypes and considering several injection strategies. Finally, a qualitative validation of the computational model has been performed comparing the simulation results with the

available experimental data obtained through the PLIF procedure on an equivalent optical engine. The CFD model resulted to be accurate in the prediction of the mixing quality and it shows to be a reliable tool for the analysis of the main mixing mechanism and so for the assessment of the best injection strategy.

Contents

List of Figures

List of Tables

Chapter 1

1.1 Introduction

Energy is a fundamental requirement of human race since it discovered how to make fire. With the spread of society, the need for energy has been widespread. Movement of people has become a necessity and thus the energy demand for it. Energy consumption in transport sector is increasing at an average rate of 1.4% annually expected to be 155 quadrillion Btu in 2040. [10]. As more countries are in the phase of development, more is the need for transportation energy. Non-OECD countries are expected to account for 61% of global transportation energy consumption by 2040. The future transport demand will come from Non-OECD countries.

Petroleum and other liquid fuels are major source of transportation energy, although their share of total energy transportation energy is expected to decline from 96% to 88% in 2012-2040 period. In this, Motor gasoline remains the largest transportation fuel followed by diesel. The share of natural gas as transportation fuel grows from 3% to 11% in 2012-2040 period. Major increase in the use of natural gas is projected for the large trucks from 1% to 15% in 2012-2040 period. In addition to this, natural gas share in bus energy consumption is projected to be 50% in 2040 as well as 17% freight rail, 7% of light-duty vehicles and 6% domestic marine vessels.

1.2 Environmental impact of transportation sector

Transport sector is the second largest contributor to the global energy related CO2 emissions with 24% share. It is expected that transport sector will contribute 9.4Gt of CO2 emissions by 2040 from 7.5Gt today and its share in global energy related CO2 emissions will grow by two percentage points to 26% in 2040 [10]. The reasons being:

I Demand for mobility grows, mainly from the developing countries, which are expected to double the number of total passenger vehicle stock to around 2 billion vehicles by 2040.

II Demand for road freight transport grows strongly due to the strong economic activities in developing countries as a result of consumer demand. (Around one-third of net global oil demand growth is expected to come from trucks by 2040).

III Demand in other areas, such as aviation and international shipping also increases.

Transport sector consists of 4 subsectors: Road, Sea, air and rail transport. Road is the largest sector in size accounting for around 73% of total transport GHG emission followed by aviation and navigation mode as shown in Fig1.1

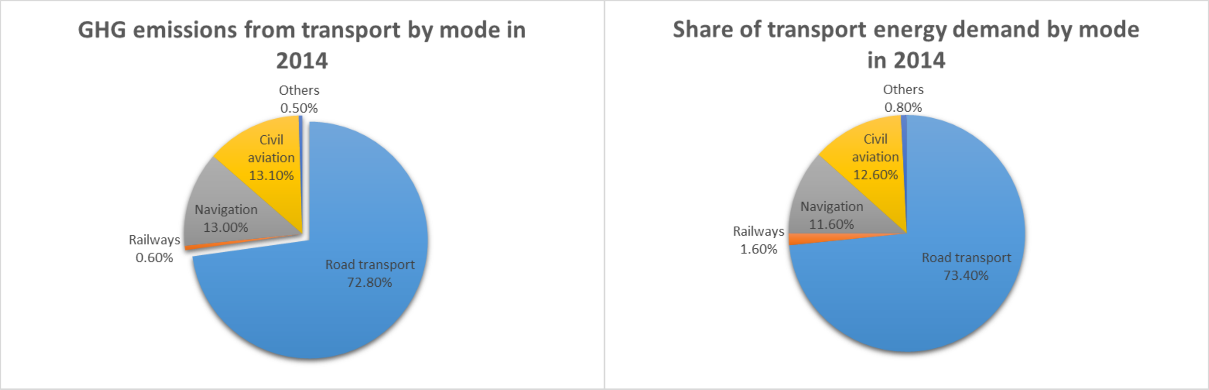

Fig. 1.1 (a)GHG emissions (b) Energy demand, in different transport modes

Road transport sector all emissions should be taken into account and thus “well-to-wheel”, including emissions related to the production of fuel (“well-to-tank”) and fuel combustion emissions (“tank-to-wheel”). The “tank-to-wheel” emissions accounts for around 88% of the total emissions by road sector. In the Paris Agreement on climate change, which entered into force in November, 2016, transport sector emission reduction is at the very centre. The focus points are:

I Increasing the efficiency of the transport system by extensive use of digital technologies, and further encouraging the shift to lower emission transport modes

II Development of low-emission alternative energy transport, such as biofuels, electricity, hydrogen and removing obstacles to the electrification of the transport

III Moving towards zero emission vehicles

To achieve these goals, the short term and long term plans need to be realized and implemented. In short term goals (keeping 2020+ emission targets in mind) the use of alternative fuels such as natural gas and biofuels, which has less impact on environment can be adopted along with the improvement in the engine efficiency. In long term goals (keeping 2040+ emission targets in mind), electric vehicles with zero emission have to be realized to meet the promise of reducing CO2 emissions. Natural gas is one of the options for short term emission goals. Anticipating this approach, natural gas demand in transport sector is expected to increase globally by over 160bcm in 2040, primarily spurred by the road transport which accounts for two-thirds of the additional gas demand in the transport sector. This increase is due to the potential of natural gas as low GHG emission can be achieved over conventional fuel, depending on vehicle type, drive cycle and engine calibration. In addition, using natural gas may reduce some types of tailpipe emissions. The emissions of primary concern are unburned hydrocarbons, oxides of nitrogen (NOx), carbon monoxides (CO), as well as carbon dioxide (CO2). The technological advancement in the use of natural gas in engine such as direct injection, Variable valve lift, turbocharging and higher compression ratio can be helpful in meeting the future emission targets (both homologation and fleet emissions).

1.3 Internal combustion engine optimization for SI/NG engines

1.3.1 Properties of Natural gas

Natural gas which is mainly composed of methane, and is regarded as one of the most promising alternative fuels due to its interesting chemical properties such as high octane number (about 130) and high H/C ratio. This gives an advantage to allow combustion at higher compression ratio without knocking. Also, natural gas has relatively high flammability limits. The lower peak combustion temperatures under ultra-lean combustion in comparison to stoichiometric conditions [1] leads to a lower knock tendency, allowing a higher power for the same engine displacement by increasing the boost level [2]. The use of higher compression ratio, high EGR circulation or lean burn mixture in NG engines would be expected to outperform gasoline engines in performance [3,4] and also lower engine out emissions can be achieved with an improvement in the thermal efficiency [4]. However, the laminar flame speed of natural gas is lower than that of gasoline due to its higher activation energy. This effect is significant during lean burn conditions. To compensate lower burning velocity of lean mixtures it is important to increase the turbulence and charge density to attain a rapid burning rate[16].

1.3.2 Expected emission improvements with NG engine over gasoline engines

Due to lower flame speeds and low combustion temperatures of NG engines, operating under lean conditions and higher compression ratio or turbocharged, engine out NOx emissions can be expected to be lower than in gasoline engines. Furthermore the gaseous nature of the fuel prevents the problem of wall wetting in the intake manifold and in the cylinder liner,especially during cold operating conditions, with further benefits on fuel economy and unburned hydrocarbons emissions.

1.4 Operating envelope of lean burn engine

1.4.1 Limitations of lean mixtures

To achieve the full benefits of the NG engine, its operation on lean burn conditions is important thus making the air-fuel ratio a critical parameter to control. Too much lean mixture can lead to increase in the heat transfer to the cylinder walls thus decreasing the thermal efficiency [17]. Also during lean burn operation, slow flame propagation can cause combustion instability with high cycle to cycle variation[18]. This condition can also lead to misfiring and thus resulting in higher HC emissions [19]. So there is a very important need to understand the factors which can affect the air-fuel ratio near the lean burn limits. These factors include in-cylinder air motion, available ignition energy, natural gas composition, mixture temperature at ignition, residual fraction, laminar flame speed of the mixture and its modification due to residual fraction etc. Also the effect of mixture preparation on the homogeneity of the cylinder charge is important.

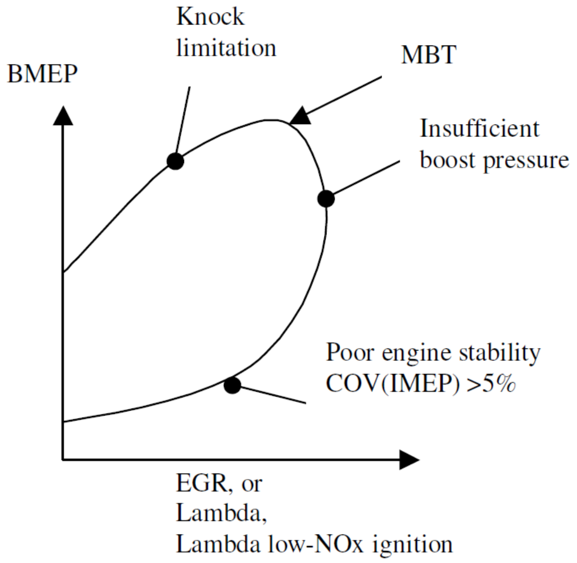

Fig. 1.2 Limitations in load and dilution for the engine mapping

The plot in figure 1.2 shows the operating range under different conditions [5], the curve reports the qualitative evolution of brake mean effective pressure (BMEP) as function of the lambda value. The λ (Lambda) value is given by equation 1.1

$$\lambda = \frac{\alpha_{actual}}{\alpha_{stoichiometric}} \tag{1.1}$$

where α is the air-fuel ratio. The BMEP is an index with pressure dimension that represents the engine work at the wheel divided by the engine displacement, it is usually employed in the engine field in order to compare the engine capability to provide work independently by the engine displacement. The lambda limits for natural gas engine are limited by the misfiring and NOx under lean burn conditions and by the level of knock under fuel rich conditions. Both the cases have negative impact on the fuel consumption. Moreover, extremely lean mixtures could lead to flame quenching, partial burn and combustion instability. Dilution due to residuals from the previous cycle, under low and medium load condition, also limits the engine combustion.

1.4.2 Achievement of stable combustion at lean burn

Previous research has shown that the air-methane mixture has low burning velocity compared to air-gasoline mixture [6,7]. Homogeneous lean burn mixtures result in lower flame propagation, occurrence of misfire, low mixture distribution quality in multi-cylinder engines and high unburned hydrocarbon emissions. High compression ratio, high energy ignition system, increased turbulence are required for the successful implementation of a lean burn strategy to NG engines.

Fluid flow characteristics should be carefully modelled to promote combustion under all operating conditions [20,21]. Increasing the organised charge motion in the cylinder leads to increased turbulence levels [22], which speeds up the combustion process [23] [24] and thus reducing cycle to cycle variation [22]. The combustion chamber design has a significant impact on the turbulence level. Intake ducts and valve lift dominates this list of design improvements. In this research topic the effects and potential benefits of the intake port masking on turbulence and combustion stability will be evaluated as far as the optimization of compression ratio by means of experimental and numerical approach.

1.4.3 Influence of direct injection

In now a day's application of natural gas engines, there are two operating modes. First, homogeneous charge mode, the homogeneous mixture of natural gas and air is ignited by spark plug as in conventional port fuel injection systems. The major drawback of this mode is the loss in volumetric efficiency as natural gas occupies a larger faction of the intake change. Also, the homogeneous charge combustion makes it difficult to burn the lean mixture as natural gas has narrow flammability limit. Furthermore, this mode has lower thermal efficiency due to knock restrictions and unavailable throttling at part loads. The second operating mode is dual fuel mode, in which the homogeneous natural gas is ignited by pilot injection of diesel fuel before TDCf. This mode has its own complexities in terms of dual fuel supply systems. Also, HC emissions are high even at part loads in this mode [8]. With the advancement in the direct injection system and combustion development in the gasoline engine, this method can be effectively replicated in natural gas engines. Due to the charge stratification and turbulence in the combustion chamber, lean combustion can be realised without high cycle to cycle variation. This system can be utilized to avoid the loss in volumetric efficiency, as natural gas is directly injected in to the cylinder. It is flexible in mixture preparation as stratified mixture can be prepared at low loads and thus improving the fuel efficiency. The ability to increase the compression ratio further improves the engine performance. In this study, the direct injection is modelled and studied using the 3D CFD simulation. This study includes the effect of turbulence in mixture preparation, the effect of the location of injector and injection timing.

Chapter 2

Literature Review

2.1 Introduction to Numerical methods

This section introduces basic concepts on computational fluid dynamics (CFD) focusing the attention on the application to internal combustion engines.

The Navier-Stokes equations have been known for over a century but the complex nature of their mathematical formulation make it possible to obtain an analytical solution only for few specific or very simplified cases. Although the analytical solutions for these special conditions are useful for the comprehension of flow behaviour in ideal cases they are not directly applicable in the engineering analysis and design. This limitation leaded to the development of different numerical methods for the resolution of partial differential equations (PDE's). Some mathematical tools for the numerical solution of PDE, like the Finite Difference Method, were developed centuries in advance respect to the development of electronic computers but the bigger impulse in this research field is registered after the development of the first computer around the 1950. Moreover the continuous increase in computational power and the relative cost decrease made the CFD analysis possible and convenient for many companies and researchers. An even harder task is related to the numerical simulation of turbulent combustion. In this field two challenging phenomena like simulation of chemistry and simulation of turbulent flow are coupled and the complexity of the overall process and the related computational cost is highly increased. The final procedure on this topic is far to be assessed and many researchers faced this challenging task proposing different approaches varying from a pure DNS procedure that is not feasible on real scale problem to a very simplified scheme that totally neglect the turbulence effect as the Arrhenius approach [13].In this chapter one of the method developed for RANS simulations, the ECFM model, will be briefly described to let the readers familiarize with the terms used in the following sections where such a model is applied.

2.2 Basic equations of Fluid Flow, Navier-Stokes equation

Fluid flow equations are made essentially of differential equations representing the interrelationship between the flow variables and their evolution in time and in space. These equations are complemented by algebraic relations such as the equation of state for compressible flow.

The Navier-Stokes and continuity equations provide the foundations for modelling fluid motion. The laws of motion that apply to solids are valid for all matter including liquids and gases. A principal difference, however, between fluids and solids is that fluids distort without limit. For example, if a shear stress is applied to a fluid, then layers of the fluid particles will move relative to each other and the particles will not return to their original position if application of the shear force is stopped. Analysis of a fluid needs to take account of such distortions.

A fluid particle responds to a force in the same way that a solid particle will. If a force is applied to a particle, acceleration will result as governed by Newton's second law of motion, which states that the rate of change of momenum of a body is proportional to the unbalanced force acting on it and takes place in the direction of the force. It is useful to consider the forces that a fluid particle can experience. These include:

- Body forces such as gravity and electromagnetism
- Force due to pressure
- Force due to viscous action
- Forces due to rotation

Assuming that the shear rate in a fluid is linearly related to shear stress, and that the fluid flow is laminar, Navier (1823) derived the equations of motion for a viscous fluid from molecular considerations. Stokes (1845) also derived the equations of motion for a viscous fluid in a slightly different form and the basic equations that govern fluid flow are now generally known as the Navier-Stokes equations of motion. The Navier-Stokes equations can also be used for turbulent flow, with appropriate modifications. The Navier-Stokes equations can be derived by considering the dynamic equilibrium of a fluid element.

For example the temperature distribution of a flow in a straight pipe, where the velocity is fixed by pumping a fixed volume flow rate into the pipe. Assume also that the flow velocity is not altered by the change in temperature. The temperature distribution T(x,t) in the pipe as a function of the pipe axial coordinate x is given by the following differential equation:

$$\frac{\partial T}{\partial t} + u\frac{\partial T}{\partial x} - \alpha\frac{\partial^2 T}{\partial x^2} = 0 \tag{2.1}$$

Where u is the flow velocity which is assumed constant across the pipe, t is time and α is the thermal diffusivity. In the above equation the first term is the time derivative expressing the temperature gradient with time. The second term is called the advection term which is responsible for the transport of any temperature disturbance with the flow without any distorsion. The third term is called the diffusion term, which is responsible for the spread of any disturbance in all directions.

If the thermal diffusivity is assumed to be negligible equation 2.1 reduces to:

$$\frac{\partial T}{\partial t} + u\frac{\partial T}{\partial x} = 0 \tag{2.2}$$

A temperature disturbance entering the pipe from the left at time $t = 0$ will be convected without any distorsion after a while to the right. If the velocity is zero equation 2.1 reduces to:

$$\frac{\partial T}{\partial t} - \alpha\frac{\partial^2 T}{\partial x^2} = 0 \tag{2.3}$$

2.2.1 Navier-Strokes equation for compressible flow

Once the Navier-Stokes equations are derived those could be arranged in a simplified form for both compressible or incompressible fluid flow. In this section the equations for compressible fluid flows will be analyzed.

The flow governing equations are the continuity equation, momentum equation (Navier- Stokes) and energy equation.

The continuity equation:

$$-\frac{\partial \rho}{\partial t} = \frac{\partial(\rho u)}{\partial x} + \frac{\partial(\rho v)}{\partial y} + \frac{\partial(\rho w)}{\partial z} \tag{2.4}$$

The Navier-Stokes equation:

$$\rho\Big(\frac{\partial u}{\partial t} + u\frac{\partial u}{\partial x} + v\frac{\partial u}{\partial y} + w\frac{\partial u}{\partial z}\Big) = -\frac{\partial p}{\partial x} + \mu\Big(\frac{\partial^2 u}{\partial x^2} + \frac{\partial^2 u}{\partial y^2} + \frac{\partial^2 u}{\partial z^2}\Big) + F_x \tag{2.5}$$

$$\rho\Big(\frac{\partial v}{\partial t} + u\frac{\partial v}{\partial x} + v\frac{\partial v}{\partial y} + w\frac{\partial v}{\partial z}\Big) = -\frac{\partial p}{\partial y} + \mu\Big(\frac{\partial^2 v}{\partial x^2} + \frac{\partial^2 v}{\partial y^2} + \frac{\partial^2 v}{\partial z^2}\Big) + F_y \tag{2.6}$$

$$\rho\Big(\frac{\partial w}{\partial t} + u\frac{\partial w}{\partial x} + v\frac{\partial w}{\partial y} + w\frac{\partial w}{\partial z}\Big) = -\frac{\partial p}{\partial z} + \mu\Big(\frac{\partial^2 w}{\partial x^2} + \frac{\partial^2 w}{\partial y^2} + \frac{\partial^2 w}{\partial z^2}\Big) + F_z \tag{2.7}$$

The energy equation:

$$\rho c_p\Big(\frac{\partial T}{\partial t}+u\frac{\partial T}{\partial x}+v\frac{\partial T}{\partial y}+w\frac{\partial T}{\partial z}\Big)=\phi+\frac{\partial}{\partial x}\Big(k\frac{\partial T}{\partial x}\Big)+\frac{\partial}{\partial y}\Big(k\frac{\partial T}{\partial y}\Big)+\frac{\partial}{\partial z}\Big(k\frac{\partial T}{\partial z}\Big)+\Big(u\frac{\partial p}{\partial x}+v\frac{\partial p}{\partial y}+w\frac{\partial p}{\partial z}\Big) \tag{2.8}$$

Where ϕ is the dissipation function, u, v, w are the velocity components in the x, y, z directions, ρ is the density, T is the temperature, p is the pressure, μ is the viscosity and c_p is the specific heat at constant pressure.

The continuity equation is an expression representing the mass conservation law; per unit volume, the sum of all masses flowing in and out per unit time must be equal to the change of the mass due to change in density per unit time.

The continuity equation applies to all fluids, compressible and in-compressible flow, Newtonian and non-Newtonian fluids. It expresses the law of conservation of mass at each point in a fluid and must therefore be satisfied at every point in a flow field. It is worthwhile to offer brief comment on the physical significance of equations (2.6-2.8). The terms on the left side are often referred to as inertial terms, and arise from the momentum changes. These are countered by the pressure gradient, $\partial p/\partial x$, viscous forces which always act to retard the flow, and if present, body forces. The inertial term gives a measure of the change of velocity of one fluid element as it moves about in space. The term $\partial/\partial t$ gives a measure of the change of velocity at a fixed point and it is known as the local derivative. The remaining three terms of the inertial term are grouped together and known as the convective terms or convective differential.

Assuming constant properties of viscosity and specific heat, the above system of equations contains six unknowns. With only five equations available, a further equation is needed to close the system. Usually this is provided by a constitutive relation for the pressure. For example, for an ideal gas, the relation between temperature and pressure is given by $p=\rho RT$, where R is the gas constant.

2.3 Turbulent flow

There are two radically different states of flows that are easily identified and distinguished: laminar flow and turbulent flow. Laminar flows are characterized by smoothly varying velocity fields in space and time in which individual "laminae" (sheets) move past one another without generating cross currents. These flows arise when the fluid viscosity is sufficiently large to damp out any perturbations to the flow that may occur due to boundary imperfections or other irregularities. These flows occur at low-to-moderate values of the Reynolds number.

In contrast, turbulent flows are characterized by large, nearly random fluctuations in velocity and pressure in both space and time. These fluctuations arise from instabilities that grow until nonlinear interactions cause them to break down into finer and finer whirls that eventually are dissipated (into heat) by the action of viscosity. Turbulent flows occur in the opposite limit of high Reynolds numbers.

The equations governing a turbulent flow are precisely the same as for a laminar flow, however, the solution is clearly much more complicated in this regime. The approaches to solving the flow equations for a turbulent flow field can be roughly divided into two classes. Direct Numerical Simulations (DNS) use the speed of modern computers to numerically integrate the Navier-Stokes equations, resolving all of the spatial and temporal fluctuations, without resorting to modelling. In essence, the solution procedure is the same as for laminar flow, except the numerics must contend with resolving all of the fluctuations in the velocity and pressure. DNS remains limited to very simple geometries (e.g., channel flows, jets and boundary layers) and is extremely expensive to run.

The alternative to DNS found in most CFD packages (including STAR®) is to solve the Reynolds Averaged Navier Stokes (RANS) equations or, less widespread, the Large Eddy Simulation (LES) which takes in account the energy of the largest eddy. RANS equations govern the mean velocity and pressure. Because these quantities vary smoothly in space and time, they are much easier to solve; however, as will be shown below, they require modelling to “close” the equations and these models introduce significant error into the calculation. To demonstrate the closure problem, we consider fully developed turbulent flow in a channel of height 2H. Recall that with RANS we are interested in solving for the mean velocity $\overline{u}(y)$ only.

If we formally average the Navier-Stokes equations and simplify for this geometry, we arrive at the following

$$\frac{\partial \overline{u'v'}}{\partial y} + \frac{1}{\rho}\frac{\partial \overline{p}}{\partial y} = \frac{\partial^2 \overline{u}(y)}{\partial y^2} \tag{2.9}$$

Subject to the boundary condition

$$\frac{\partial \overline{u}}{\partial y} = 0 \qquad for \quad y = 0 \tag{2.10}$$

$$\overline{u} = 0 \qquad for \quad y = H \tag{2.11}$$

The quantity $\overline{u'v'}$ called Reynolds stress, is a higher-order moment that must be modeled in terms of the knowns (i.e.,$\overline{u}(y)$ and its derivatives). This is referred to as the “closure” approximation. The quality of the modelling of this term will determine the reliability of the computations. Turbulence modelling is a rather broad discipline and an in-depth discussion is beyond the scope of this introduction. Here we simply note that the Reynolds stress is modelled in terms of two turbulence parameters, the turbulent kinetic energy k and the turbulent energy dissipation rate ε

defined below. This method is usually known as k-ε method.

$$k = \frac{1}{2}(\overline{u'} + \overline{v'} + \overline{z'}) \tag{2.12}$$

$$\varepsilon = v\Big[\Big(\frac{\partial u'}{\partial x}\Big)^2 + \Big(\frac{\partial u'}{\partial y}\Big)^2 + \Big(\frac{\partial u'}{\partial z}\Big)^2 + \Big(\frac{\partial v'}{\partial x}\Big)^2 + \Big(\frac{\partial v'}{\partial y}\Big)^2 + \Big(\frac{\partial v'}{\partial z}\Big)^2 + \Big(\frac{\partial w'}{\partial x}\Big)^2 + \Big(\frac{\partial w'}{\partial y}\Big)^2 + \Big(\frac{\partial w'}{\partial z}\Big)^2\Big] \tag{2.13}$$

Where (u, v, w') is the fluctuating velocity vector. The kinetic energy is zero for laminar flow and can be as large as 5 % of the kinetic energy of the mean flow in a highly turbulent case. The family of models is generally known as k-ε and they form the basis of most CFD packages.

2.3.1 The k-ε Turbulence Model

Traditionally, RANS models use an effective turbulent viscosity to model the Reynolds stress term. Thus, additional turbulent diffusion (i.e., diffusive mixing) models the turbulent convective mixing. The modeled Reynolds stress for the Standard k-e and RNG models is given by

$$\tau_{ij} = -\bar{\rho}\,\widetilde{u'_i u'_j} = 2\mu_t S_{ij} - \frac{2}{3}\delta_{ij}\Big(\rho k + \mu_t \frac{\partial\,\widetilde{u'_i}}{\partial x_i}\Big) \tag{2.14}$$

The turbulent kinetic energy, k, is defined as half of the trace of the stress tensor:

$$k = \frac{1}{2}\,\widetilde{u'_i u'_j} \tag{2.15}$$

Where the turbulent viscosity, μ_t is given by

$$\mu_t = c_\mu \rho \frac{k^2}{\varepsilon} \tag{2.16}$$

In the previous equation, c_μ is a model constant that can be tuned for a particular flow and ε is the dissipation of turbulent kinetic energy. The mean strain rate tensor S_{ij} is given by

$$S_{ij} = \frac{1}{2}\Big(\frac{\partial\,\widetilde{u'_i}}{\partial x_j} + \frac{\partial\,\widetilde{u'_i}}{\partial x_j}\Big) \tag{2.17}$$

The models use turbulent diffusion and turbulent conductivity terms to account for the presence of turbulence in mass transport and energy transport. The turbulent diffusion and conductivity terms are given by

$$D_t = \left(\frac{1}{Sc_t}\right)\mu_t \tag{2.18}$$

$$K_t = \left(\frac{1}{Pr_t}\right)\mu_t c_p \tag{2.19}$$

where Sc_t is the turbulent Schmidt number, Pr_t is the turbulent Prandtl number, D_t is the turbulent diffusion, and K_t is the turbulent conductivity. For the standard k-ε and RNG k-ε models, additional transport equations are needed to obtain the turbulent viscosity given by equation **??**. One equation is needed for the turbulent kinetic energy, k, and one for the dissipation of turbulent kinetic energy, ε. The turbulent kinetic energy transport equation is given by

$$\frac{\partial \rho \varepsilon}{\partial t} + \frac{\partial \rho u_i k}{\partial x_i} = \tau_{ij}\frac{\partial u_i}{\partial x_j} + \frac{\partial}{\partial x_j}\frac{\mu}{Pr_k}\frac{\partial k}{\partial x_j} - \rho\varepsilon + \frac{c_s}{1.5}S_s \tag{2.20}$$

In the previous equation, the factor of 1.5 is an empirical constant. The transport equation for the dissipation of turbulent kinetic energy is given by

$$\begin{aligned}\frac{\partial \rho \varepsilon}{\partial t} + \frac{\partial \rho u_i \varepsilon}{\partial x_i} = \frac{\partial}{\partial x_i}\left(\frac{\mu}{Pr_k}\frac{\partial \varepsilon}{\partial x_j}\right) + c_{\varepsilon 3}\rho\varepsilon\frac{\partial u_i}{\partial x_i} + \left(c_{\varepsilon 1}\frac{\partial u_i}{\partial x_j}\tau_{ij} - c_{\varepsilon 2}\rho\varepsilon + c_s S_s\right)\frac{\varepsilon}{k} \\ +S - \rho R\end{aligned} \tag{2.21}$$

where S is the user-supplied source term and S_s is the source term that represents interactions with discrete phase (spray). Note that these two terms are distinct. The $c_{\varepsilon i}$ terms are model constants that account for compression and expansion. In the previous equation, $R = 0$ for the standard k-ε model and

$$R = \frac{C_\mu \eta^3\left(1 - \frac{\eta}{\eta_o}\right)\varepsilon^2}{(1+\beta\eta^3)k} \tag{2.22}$$

for the RNG k-ε model. In Equation 2.23

$$\eta = \frac{k}{\varepsilon}|S_{ij}| = \frac{k}{\varepsilon}\sqrt{2S_{ij}S_{ji}} \tag{2.23}$$

The Rapid Distorsion RNG k-ε model uses the transport equation for ε given by

$$\begin{aligned}\frac{\partial \rho \varepsilon}{\partial t} + \frac{\partial \rho u_i \varepsilon}{\partial x_i} = \frac{\partial}{\partial x_i}\left(\frac{\mu}{Pr_k}\frac{\partial \varepsilon}{\partial x_j}\right) - \left[\frac{2}{3}c_{\varepsilon 1} - c_{\varepsilon 3} + \frac{2}{3}c_\mu c_\eta \frac{k}{\varepsilon}\frac{\partial u_k}{\partial x_k}\right]\rho\varepsilon\frac{u_i}{x_i} + \\ \left(c_{\varepsilon 1 - c_\eta}\frac{\partial u_i}{\partial x_j}\tau^*_{ij} - c_{\varepsilon 2}\rho\varepsilon + c_s S_s\right)\frac{\varepsilon}{k}\end{aligned} \tag{2.24}$$

where

$$c_\eta = \frac{\eta\left(1 - \frac{\eta}{\eta_o}\right)}{(1+\beta\eta^3)} \tag{2.25}$$

and

$$\tau^*_{ij} = \tau_{ij} - \frac{1}{3}\delta_{ij}\tau_{kk} = 2\mu_\tau\Big(S_{ij} - \frac{1}{3}\delta_{ij}\frac{\partial u_k}{\partial x_k}\Big) \tag{2.26}$$

The source term, S_s, in Equations 2.27, 2.28, **??** is included to account for the interactions of turbulence with the discrete phase. This term is modelled as

$$S_s = -\frac{\sum_p N_P (F'_{drag,i} u'_i)_p}{V} \tag{2.27}$$

where the summation is over all parcels in the cell, N_p is the number of drops in a parcel, V is the cell volume, u'_i is the fluctuating component of the gas-phase velocity, and

$$F'_{drag,i} = \frac{F_{drag,i}}{u_i + u'_i - v_i} \tag{2.28}$$

where $F_{drag,i}$ is the drag force on a drop. It is important to note that although the c_s model constant only appears in front of S_s in the transport equation, setting c_s to zero in the input files actually deactivates the source term in both the k and ε equations.

2.4 Combustion Models

In this section we will introduce the turbulence flame models and then understand the premixed turbulence combustion. Combustion requires that fuel and oxidizer be mixed at the molecular level. How this takes place in turbulence combustion depends on the turbulent mixing process. The general view is that once a range of different size eddies has developed, strain and stress will increase and thereby steepen the concentration gradients at the interface between reactants, which in turn enhances their molecular inter-diffusion. Molecular mixing of fuel and oxidizer, as a prerequisite of combustion, therefore takes place at the interface between small eddies.

Our interest in laminar flame speed is two folds: First, it is used to define the characteristics chemical reaction time of the mixture by Damkohler number:

$$Da = \frac{\tau_T}{\tau_L} = \Big(\frac{l_I}{\delta_L}\Big)\Big(\frac{S_L}{u'}\Big) \tag{2.29}$$

Second, a presumed consequence of the wrinkled thin-reaction-sheet turbulent-flame structure is that, locally, the sheet propagates at the laminar burning velocity.

The flame is initiated at the spark plug, However, it may move away from the plug during the early stage of its development. A_f is defined as the flame front area, r_f is the spherical surface radius coinciding with the leading edge of the flame contained within the chamber behind the flame front. r_b, the burned gas radius, is the radius of the spherical surface within the combustion chamber which would contain all the burned gas behind it; i.e.,

$$V_b(r_b, r_c, \alpha_c, z_c) = V_b(p, \theta) \tag{2.30}$$

Where r_c,α_c and z_c are the coordinates of the flame centre as shown in Figure 2.1

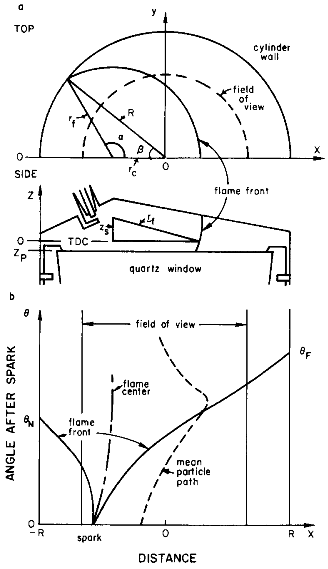

Fig. 2.1 Schematic diagram of combustion chamber geometry and spherical flame front. b) Angle versus distance plot showing qualitative trajectories for flame center, flame fronts, and gas particle [11]

The spherical burning area Ab is the area of this spherical surface; i.e..

$$A_b = \frac{\partial V_b(r_b, r_c, \alpha_c, z_c)}{\partial r_b} \tag{2.31}$$

The laminar burning area A_L is the surface area the flame would have if it burned at the laminar flame speed i.e.,

$$A_L = \frac{dm_b/dt}{\rho_u S_L} \tag{2.32}$$

Where S_L is the laminar flame speed in the unburned mixture ahead of the flame.
The mean expansion speed of the front u_f is given by

$$u_f = \frac{dA_S/dt}{L_S} \tag{2.33}$$

Where A_S is the “shadow” area enclosed by the “best fit” circle through the leading edge of the flame and

$$L_S = \frac{\partial A_S}{\partial r_f} \tag{2.34}$$

L_S the arc length within the chamber of this “best fit” circle. The mean expension speed of the burned gas u_b is

$$u_b = \frac{\partial V_b/\partial t}{A_b} \tag{2.35}$$

This derivation is taken with the piston position fixed since only burned gas volume changes due to combustion are of interest. The burning speed S_b is defined by

$$S_b = \frac{dm_b/dt}{\rho_u A_b} \tag{2.36}$$

The mean gas speed just ahead of the flame front u_g is

$$u_g = u_b - S_b \tag{2.37}$$

Combining above equations (2.32 -2.37) gives the relation

$$S_b A_b = S_L A_L \tag{2.38}$$

The difference between u_b and S_b is the unburned gas speed u_g just ahead of the flame front. The effect of the flame propagation on the flow field in the unburned mixture ahead of the flame is important because it is the turbulence just ahead of the flame that determines the local burning velocity.

Combustion, even without turbulence, is an intrinsically complex process involving a large range of chemical time and length scales. Some of the chemical phenomena controlling flames take place in short times over thin layers and are associated with very large mass fractions, temperatures and density gradients.The full description of chemical mechanisms in laminar flames may require hundreds of species and thousands of reactions leading to considerable numerical difficulties.

Turbulence itself is probably the most complex phenomenon in non-reacting fluid mechanics. Various time and length scales are involved and the structure and the description of turbulence remain an open question. Turbulent combustion results from the two-way interaction of chemistry and turbulence. When flame interacts with a turbulent flow, turbulence is modified by combustion and because of the large changes in kinematic viscosity associated with temperature changes. This mechanism may generate turbulence called “flame-generated turbulence” or damp it. On the other hand, turbulence alters the flame structure, which may enhance the chemical reaction but also, in extreme cases, completely inhibit it, leading to flame quenching.

2.4.1 Flamelet assumption

Under the flamelet assumption, chemistry is fast enough so that one can consider that the flow consists of two phases: the fresh gases and the burned gases. These two phases are separated by elements of flame called flamelets. In most flamelet models, one assumes also that each flamelet behaves like a laminar flame. This is not a necessary assumption: the only important assumption in flamelet modelling is related to the topology of the flow and to the fact that fresh and burned gases are separated by a relatively thin continuous region where chemical reactions take place. This region may have a laminar flame structure but it may also be thickened by small scale turbulence without invalidating the flamelet assumption.

Referring to the combustion regimes [12], flame quenching occurs when a flame front is submitted to external perturbations such as heat losses or sufficiently strong aerodynamic stretch to decrease the reaction rate to a negligible value, and, in some cases, to completely suppress the combustion process. For example, asymptotic studies of laminar stagnation point flame established by the counterflow of reactants and products, reveal that stretch may decrease the flame speed by a considerable amount. When no quenching occurs in a turbulent premixed flame, the flame zone is “active” everywhere and may be analysed as an interface separating fresh unburnt cold reactants from hot burnt products. This regime is called flamelet regime.

A turbulent premixed reacting flow is in a flamelet regime when a line connecting any point A in fresh gases to another point B in burnt products crosses (at least) one active flame front. Figure 2.2

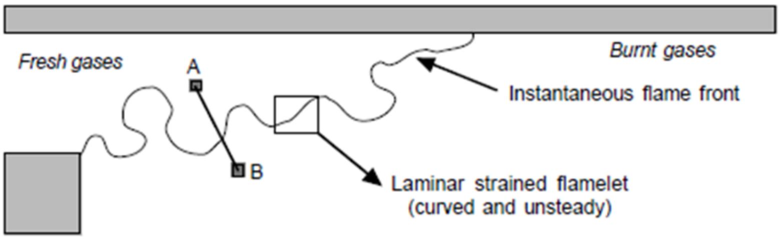

Fig. 2.2 Flamelet assumption: definition of flamelet regimes

When the local stretch induced by turbulent motions on the flame front becomes sufficiently large to quench the flame at a given location, combustion stops in the vicinity of this point and fresh reactants diffuse into the products without burning. In this situation, the description of the reacting flow becomes much more complex and standard flamelet approaches are no longer valid.

Therefore, quenching in a turbulent premixed flame determines the limit between two fundamentally different behaviours (i.e. flamelets or no flamelets) and appears as an important mechanism in the description and modelling of turbulent combustion. Flame elements are usually assumed to quench in turbulent flows for conditions similar to laminar stagnation point flames. The parameter controlling the similarity between turbulent flamelets and laminar stagnation point flames is flame stretch. This assumption is justified, once again, from asymptotic theories which show that, under certain assumptions (mainly low levels of stretch), the whole flame structure and many important flame parameters, such as displacement and consumption speeds, depend only on stretch.

2.4.2 Physical approach to model turbulent combustion

A proper turbulent combustion description cannot be based on a simple mathematical expansion around mean values. Therefore, reaction rate closures are generally developed from physical analysis, comparing chemical and turbulent time scales. According to Veynante and Vervisch [13], most turbulent combustion models are derived from one of the approaches reported in Figure 2.3. In the following section, the geometrical approach will be introduced since it is the approach adopted for the development of ECFM model.

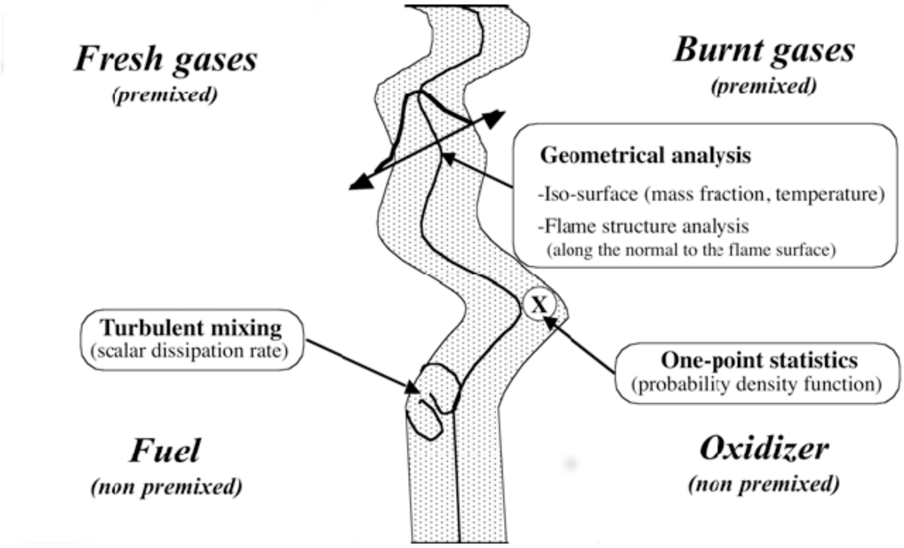

Fig. 2.3 Modelling approaches for turbulent combustion: geometrical analysis (the flame front is identified with a surface), mixing description (the reaction rate is assumed to be controlled by the mixing rate, i.e. the scalar dissipation rate) or pure statistical approach (probability density function formalism), following the analysis proposed by Veynante and Vervisch [13]

2.4.2.1 Influence of turbulence on combustion

The main effect of turbulence is to increase the combustion rate: it will be discussed by recalling premixed flame experimental results.

2.4.2.2 One dimensional turbulent premixed flames

Consider a statistically one-dimensional premixed flame propagating in a turbulent flow field as shown in Figure 2.4.

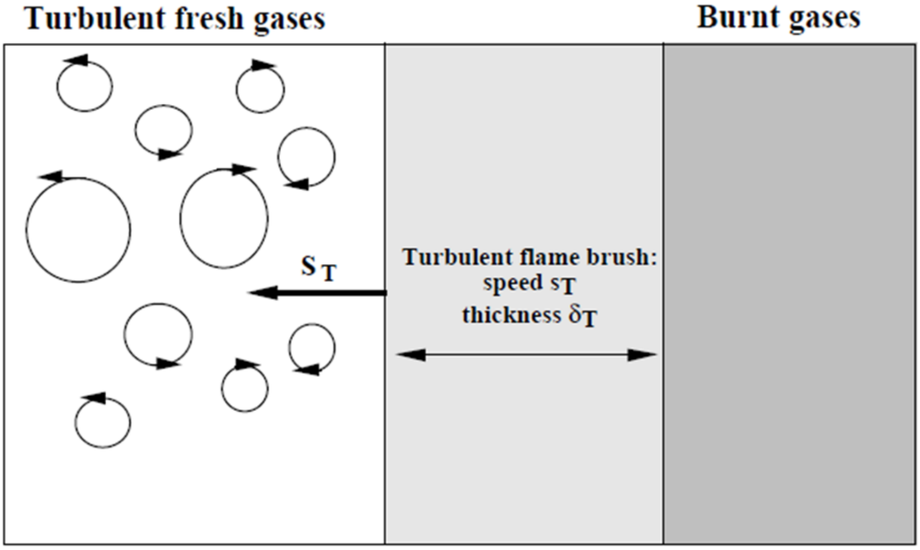

Fig. 2.4 Statistically one-dimensional premixed lame propagating in a turulent flow field [12]

In this situation, the “mean” flame brush is a planar flame, moving relatively to the flow field with a turbulent displacement speed s_T. Experimentalists have known for a long time that changing the turbulence level before starting combustion in a vessel may change the time needed for total combustion and, accordingly the turbulent flame speed. The combustion rate is maximum when the reactants are mixed in stoichiometric proportions and increases when the flow becomes turbulent (Figure 2.5). At that time, “the turbulent flame speed was always larger than two times the laminar flame speed.” The factor of two observed by Wheeler is not generic of all turbulent flames and more precise measurements lead to empirical relations such as Abdel-Gayed et al and Gulder

$$\frac{S_T}{S_L} \approx 1 + \frac{u'}{S_L} \tag{2.39}$$

where u’ is the rms (root mean square) of the velocity fluctuations (or the square root of the turbulent kinetic energy k). This approximate expression shows that premixed combustion is enhanced by turbulent motions. For large values of the velocity fluctuations, the turbulent flame speed S_T becomes roughly independent of the laminar flame speed S_L ($S_T \approx u_0$). Experiments also show that the mean turbulent flame brush thickness δ is always larger than the laminar flame thickness δ_L .

In this model the mean reaction rate based on the series expansion of the Arrhenius law can’t be retained because of the large number of unclosed quantities (correlation between species con-

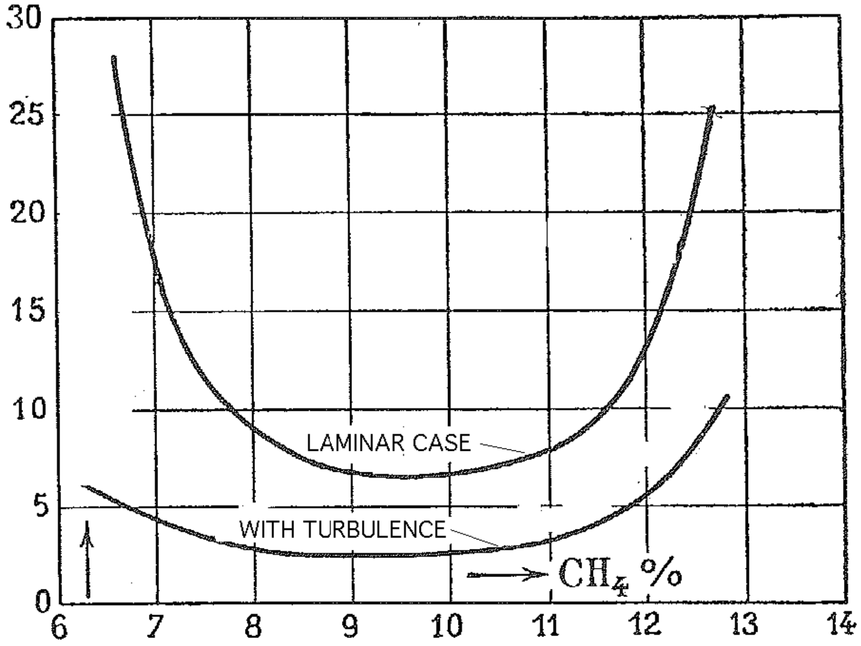

Fig. 2.5 The combustion time (the time needed to reach the maximum pressure in a closed vessel) for a methane/air flame with and without turbulence, plotted as a function of the proportion of CH_4 in the reactant mixture, corresponding to the equivalence ratio (stoichiometric proportions correspond to about 10 % of methane). [14] [15]

centration and temperature fluctuations) and of large truncated errors due to high non linearities. Therefore, the derivation of model must be based on physical analysis and comparisons of the various time and length scale involved in the combustion phenomena. These analyses lead to the so called "turbulent combustion diagrams" where various regimes are identified and delineated introducing non-dimensional characteristic numbers. Knowing the turbulent characteristics (integral length scale, turbulent kinetic energy and its dissipation rate among other characteristics), these diagrams indicate whether the flow contains flamelets (Thin reaction zones), pockets or distributed reaction zones. This information is essential in building the turbulent combustion model.

2.5 Premixed combustion models

Premixed combustion requires that the fuel and oxidizer species be completely mixed before combustion is allowed to take place. This premixing is possible only at sufficiently low temperatures where the chain-breaking mechanism that drives the reaction chain in hydrogen and hydrocarbon oxidation is unable to compete with the effect of three-body chain-breaking reactions.

Under such low-temperature conditions, combustion reactions are considered frozen. The frozen state is metastable because a sufficiently strong heat source, a spark for example, can raise the

temperature above the threshold and initiate combustion. Once the fuel and oxidizer species have been homogeneously mixed and a heat source is supplied, a flame front can propagate through the mixture.
Typically, the gas behind the flame front rapidly approaches the burned gas state close to chemical equilibrium. The mixture in front of the flame typically remains in the unburned state. Therefore, the combustion system contains two stable states: the unburned and the burned gas state as shown in Figure 2.6. In premixed combustion, both states concurrently exist in the system. They are spatially separated by the flame front, where the transition from one to the other takes place.

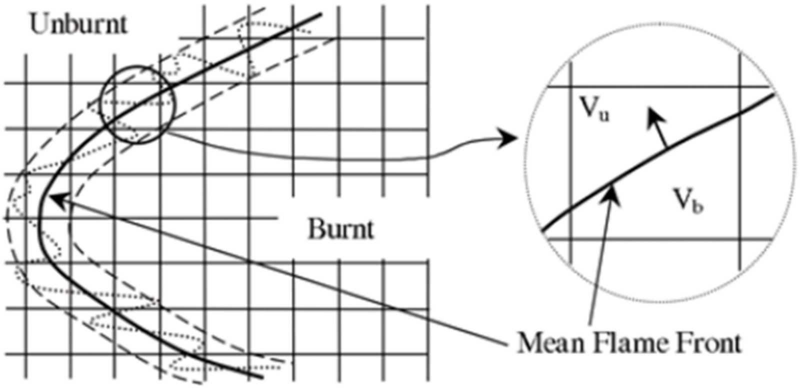

Fig. 2.6 A schematic illustrating the mean flame front and the turbulent flame brush superimposed on the computational mesh.

2.5.1 ECFM – Extended Coherent flame model

The ECFM [53] is a version of the flame surface density which allows the simulation of the premixed combustion modes, the Propagation Flame (PF) in Spark Ignition engines as well as Auto Ignition (AI) and pollutant formation even in highly stratified cases. In order to account for both mixing processes and for the Flame Diffusion (DF), each computational cell is subdivided in 3 zones: a pure fuel zone, a pure air zone (plus possible EGR) and a mixed zone. This structure allows to take into account the three main combustion modes (AI, PF and DF).
To determine the flame surface density, the ECFM uses the fuel/air equivalence ratio in fresh gases, the composition (including residual gases), and the temperature near the flame. The resulting flame surface density is used to describe large scale burned/unburned stratification.

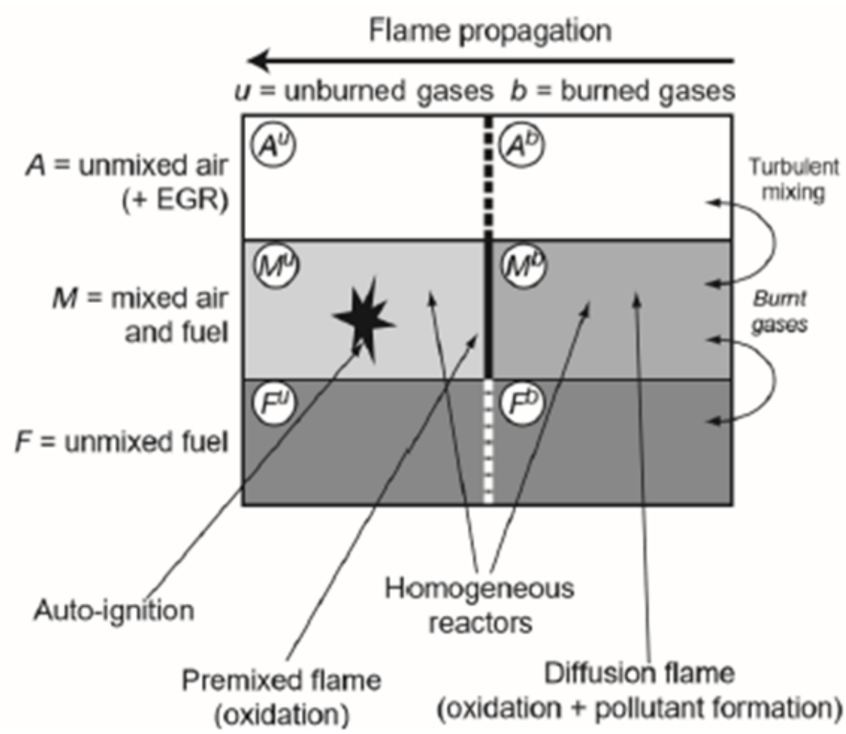

Fig. 2.7 Schematic of the ECFM-3Z model computational cell

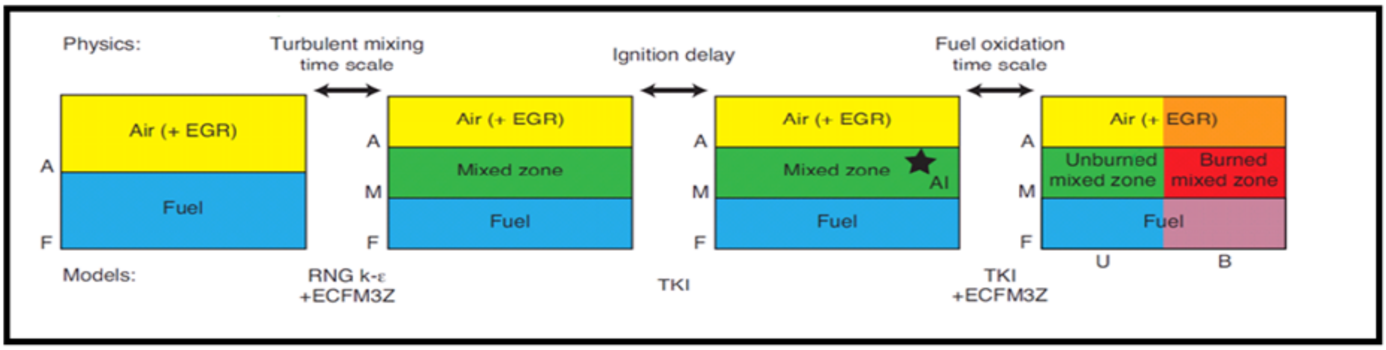

Fig. 2.8 Schematic approach for achieving ECFM-3Z Model

2.5.1.1 Tracking Flame Propagation

The flame surface density (S) is determined by the following transport equation:

$$\frac{\partial \Sigma}{\partial t} + \frac{\partial u_i \Sigma}{\partial x_i} = \frac{\partial}{\partial x_i}\left(\frac{\mu}{S_C}\frac{\partial(\Sigma/\overline{\rho})}{\partial x_i}\right) + (P_1 + P_2 + P_3)\sum - D + P_k \tag{2.40}$$

Where μ is the laminar viscosity, S_c is the Schmidt number, $P_1(=\alpha K_t)$ is the flame surface production by turbulent stretch, $P_2(=\frac{2}{3}\widetilde{\frac{\partial u_i'}{\partial x_i}})$ models the effects of the flame thermal expansion and curvature, $P_3(=\frac{2}{3}\overline{S_L}\frac{1-\widetilde{C}}{\widetilde{C}}\Sigma)$ is the production by mean flow dilation, $D(=\beta\overline{S_L}\frac{\Sigma^2}{1-\overline{C}})$ is a destruction due to consumption, P_k is the source term (such as a spark plug), S_L is the laminar flame speed, $\widetilde{C}$ is the mass progress variable and $\overline{C}$ is the volume progress variable.

2.5.1.2 Turbulent Stretch Model

The Intermittent Turbulent Net Flame Stretch (ITNFS) model shows how intermittent turbulence affects the distribution of stretch along the flame front. The ITNFS model is a library of the net flame stretch constructed. A curve fit method is used to implement the library. Turbulent stretch (K_t) is given as

$$\frac{K_t}{\varepsilon/k} = ITNFS_{factor} * f\left(\frac{u'}{S_L}, \frac{L}{l_F}\right) \tag{2.41}$$

where e is turbulent dissipation, k is turbulent kinetic energy, $u' = \sqrt{(2k/3)}$ is turbulence RMS velocity, S_L is the laminar flame speed, L is integral length scale, and l_F is the laminar flame thickness.

2.5.1.3 Imposed Stretch Spark Ignition Model

In all the other problems relative to the strong assumption and simplification made in all the combustion modelling, another important issue is relative to the initialization of the transported quantity. One possible approach that has been proposed by Colin et al is ISSIM model.

The main purpose of the ISSIM is to simulate the reaction rate due to the flame surface density (FSD) starting at the moment of ignition. This model simultaneously represents both the electrical circuit energy deposition and the flame surface and mass deposition.

The primary circuit includes the battery and the primary inductance. When the switch is open, the energy is stored in the primary inductance. Approximately 60% of the energy is transferred to the spark plug, while the remaining energy is dissipated by the secondary inductance. The ISSIM considers only the secondary part of the inductive ignition system.

The life of the spark is generally divided into three phases. The breakdown and arc phases, which last typically less than one microsecond, are taken into account by considering an instantaneous energy deposit in the gas given by:

$$E_{bd} = \frac{V_{bd}^2}{C_{bd}^2 d_{is}} \tag{2.42}$$

where V_{bd} is the breakdown voltage (approximated by Paschen's law [Reinmann and Saitzkoff, 1998]), C_{bd} is a constant, and d_{is} is the inter-electrode distance.

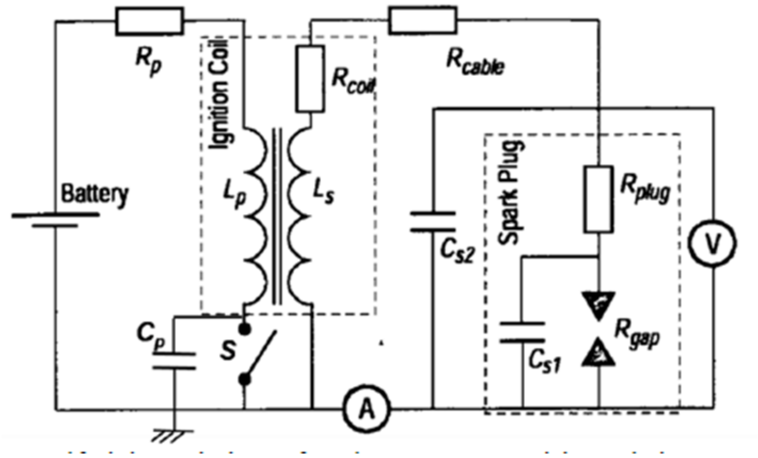

Fig. 2.9 The electrical scheme of the inductive system

The glow phase, which can last a few milliseconds, is modeled by solving the electrical circuit ODEs. During this phase, the spark voltage V_{ie} is equal to

$$V_{ie}(t) = V_{cf} + V_{af} + V_{(}gc) \tag{2.43}$$

where V_{cf} is the cathode fall voltage, V_{af} is the anode fall voltage, and V_{gc} is the gas column voltage.

When the spark voltage reaches the breakdown voltage (i.e., when $V_{ie} > V_{bd}$), the gas breaks down and becomes conductive.

The mean spark length is given by:

$$\frac{dl_{spk}^{mean}}{dt} = 2u_{conv} \tag{2.44}$$

In which u_{conv} is the mean convection, and the spark wrinkling is given by

$$\frac{dE_{spk}}{dt} = 2K_t \tag{2.45}$$

where K_t considers the turbulence wrinkling effect, which is similar to the ITNFS function in the flame surface density equation.

Chapter 3

In-cylinder Turbulence and Combustion Analysis

Part of the work described in this chapter and the relative outcomes have been already published in a research paper [25] and two other companion papers are currently being prepared. Here the contents will be reported and extended. The work described in the following section is part of a collaborative research activity performed by Politecnico di Torino and Fiat Research Center (CRF) in the framework of the “BIOMETHAIR” project, a Regional Research project promoted by Regione Piemonte, Italy (http://www.biomethair.it/index.php).

The scope of such a project was to develop an urban-mobility vehicle with a nearly nil environmental impact, the achievement of such a goal has been pursued by exploiting the potentiality of advanced technologies like Biofuels, in particular BioMethane, coupled with a mini hybrid propulsion system. The optimization of the powertrain system had a fundamental importance in the achievement of the above mentioned goal, in this context the contribution of Politecnico di Torino has been focused on the study and optimization of an innovative small displacement engine fueled with CNG.

The baseline engine adopted for the optimization study is derived from the TwinAir production engine (Table 3.1), it is a two cylinder turbocharged engine with a total displacement of 875 cm^3.The use of Variable Valve Actuation system (VVA) permits a fully flexible lift control reducing the pumping losses and improving the overall engine efficiency. Such engine commercially available for small and medium segment car, is normally fueled with gasoline or additionally in bi-fuel mode, i.e. Gasoline and Natural Gas.

Anyway the use of gasoline as the sole or the main fuel puts a limit on the maximum engine compression ratio because of its limited knock resistance, for this reason the commercial engine features a compression ratio of 10:1 that is found to be the maximum for a reliable engine use. Optimizing the engine for CNG it is possible to increase such ratio without the risk of knock and so avoiding possible damage to the engine structure.

Table 3.1 Biomethair Engine specifications

Parameters	Specifications
Displacement[cm^3]	875
Number of cylinders	2
Compression ratio	12-14 (Production engine: 10)
Turbocharger	WG-Controlled
Target torque	140Nm @ 2000rpm
Target Power	60Kw @ 5000rpm

3.1 Tumble analysis and optimization

As described in the paper [25] the work consisted in a combined experimental and numerical study where test bench data provided by CRF have been used as a validation basis for the numerical model development. The first step in the optimization phase was the study of two engine head variants with the aim of improving the in-cylinder turbulence and consequently the combustion stability.

The cylinder heads evaluated are shown in figure (figure 3.1), here it is possible to notice the difference in the intake port design.

The Design variant reported in figure 3.1-b presents a small “step” protrusion in proximity of the intake port. Such a protrusion called “Mask” is conceived in order to create a partial obstruction that produces a flow imbalance able to promote the tumble formation.

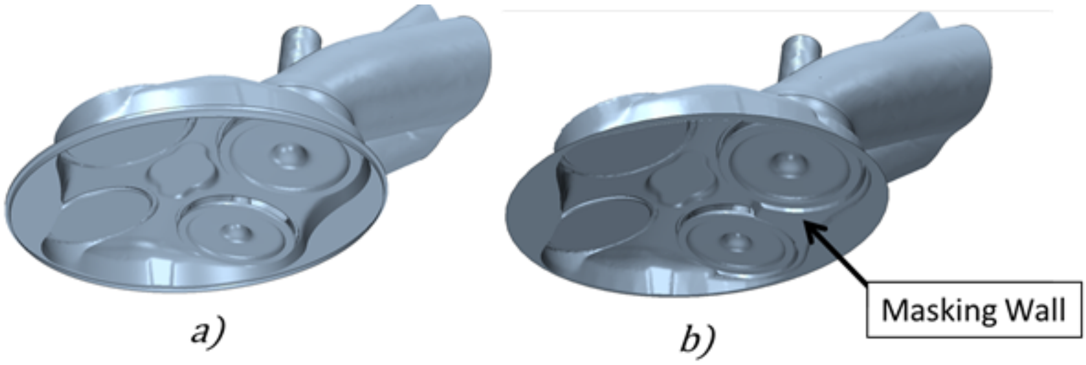

Fig. 3.1 Engine Head design a) No-Masked configuration b) Masked Configuration

The efficiency of the masking for the enhancement of tumble formation has been experimentally evaluated by means of two different methods: the well-established Ricardo Method and the Hot Wire Anemometry method that is a technique purposely developed by CRF for the present research.

The experimental test flow rig (figure 3.3) consists of a centrifugal multistage compressor capable to provide 1kg/s that enters air into plenum of 350L capacity, the plenum is in turn connected to the cylinder head mockup. During the tests the pressure ratio between the plenum and the downstream environment has been kept to 1.1 and the mass flow rate has been measured by means of a hot-film flow meter located downstream of the compressor.

A schematic of the two different methodologies adopted is given in Figure 3.2 - 3.3, the Ricardo method as previously described consists of a T-junction that converts the tumble motion to a swirling motion around the main axes of an extended perpendicular pipe. The flux of angular momentum is then evaluated measuring the torque applied on the honeycomb structures placed at the end of the extension pipe.

The rig tumble number with the Ricardo method is given by the formula:

$$N_T = \frac{8.(2T)}{\dot{m}.8.v_{is}} \tag{3.1}$$

where T is the torque applied on the honeycomb structures measured in one arm of the T-junction, vis is the isentropic mass-flow rate through the cylinder head and m is the mass flow rate through the cylinder head.

The experimental setup for the HWA technique is represented in figure 3.3. The tumbling flow is characterized by measuring the velocity component along the cylinder axis by means of a 1-D hot-wire probe.

This method has been purposely developed by CRF for the tumble characterization, based on the findings of Jante [26], and hence represents a strong innovative feature of the present research. In [26], a ‘comb’ of manometers was used to derive a dynamic pressure profile for the characterization of the scavenging flow in two-stroke engines. Similarly, the method developed by CRF exploits a two-dimensional assembly of small longitudinal tubes, from here on referred as “flow straightener”, placed between the probe and the upstream ‘flow box’. This flow box represents either the cylinder head to be tested or its rapid-prototype reproduction. The flow straightner is used in order to cancel the velocity components in the x and y directions, so that the ‘tumble’velocity can be measured by one-dimensional HWA sensors. The velocity is acquired as the probe continuously moves along the tumble axis direction (y axis), i.e., perpendicularly to the plane of figure 3.3 - left picture.

The spatial step of the acquisitions in the y direction is 0.05 mm. After each sweep the probe is displaced by 0.5 mm along the x direction until the whole ‘acquisition matrix’ gets completed (figure 3.3 - right picture). Raw data are hence postprocessed by means of a CRF proprietary code in order to generate two-dimensional velocity contours (figure 3.4). The same code produces a dimensionless measure of the tumble intensity according to the following formula:

$$N_T = \frac{-(\omega_{av,INT} + \omega_{av,EXH}).B}{V_{is}} \tag{3.2}$$

where $\omega_{av,INT}$ and $\omega_{av,EXT}$ are equivalent angular speeds referred to the intake and the exhaust side, respectively (see figure 3.4), and are given by:

$$\omega_{av,EXT} = \frac{\sum_{e=1}^{N_e} V_{z,e} X_e}{\sum_{e=1}^{N_e} X_e^2} \quad \text{and} \quad \omega_{av,INT} = \frac{\sum_{i=1}^{N_i} V_{z,i} X_i}{\sum_{i=1}^{N_i} X_i^2} \tag{3.3}$$

The definition of NT given by Eqs. (3.2) and (3.3) is based on the evaluation of the angular momentum of flow particles, according to a procedure similar to the differential methods discussed in [20–22].

According to the reference system reported in figure 3.2 and figure 3.3, the X axis is defined positive towards the intake side, so in case of positive (downwards) component of the vertical velocities $v_{z,e}$, $v_{z,i}$ (figure 3.2 and 3.3), $\omega_{av,EXH}$ is accouted as negative, due to the negative value of the X coordinate; on the contrary $\omega_{av,INT}$ is positive for positive value of $v_{z,i}$. It follows that the tumble definition is the result of the compensation between the direct tumble and the reverse tumble intensities, as expressed by $\omega_{av,INT}$ and $\omega_{av,EXH}$ respectively.

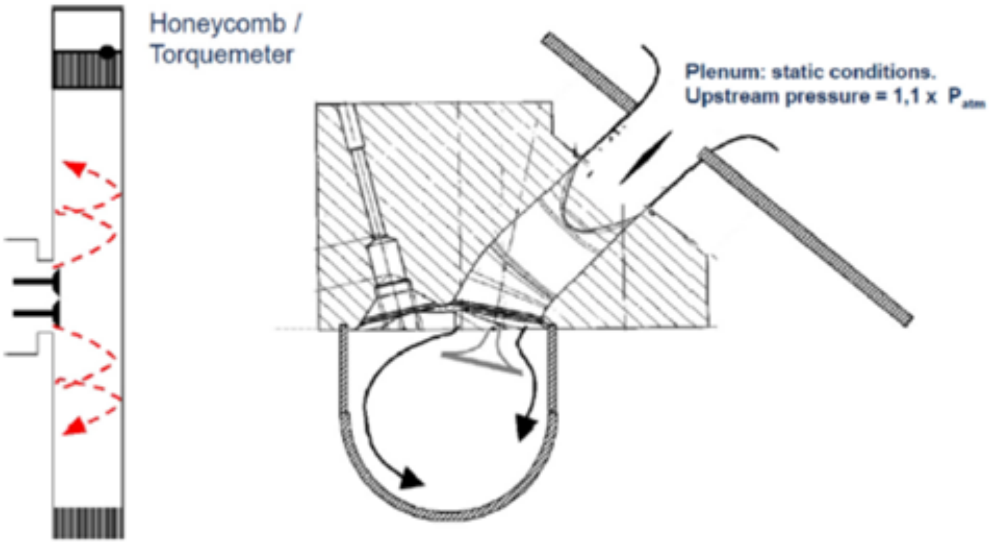

Fig. 3.2 Schematic of Ricardo Method Procedure

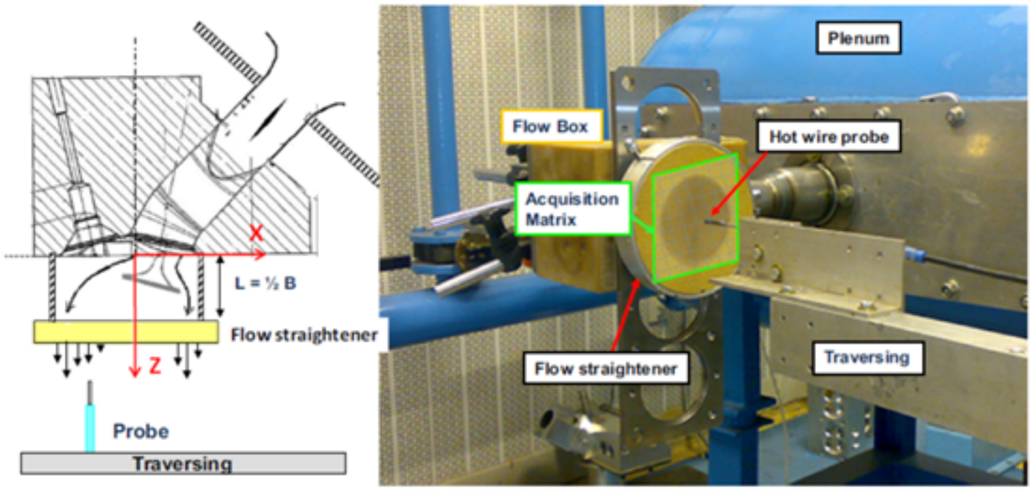

Fig. 3.3 HWA experimental procedure Scheme (left) - Experimental Flow rig test bench (right)

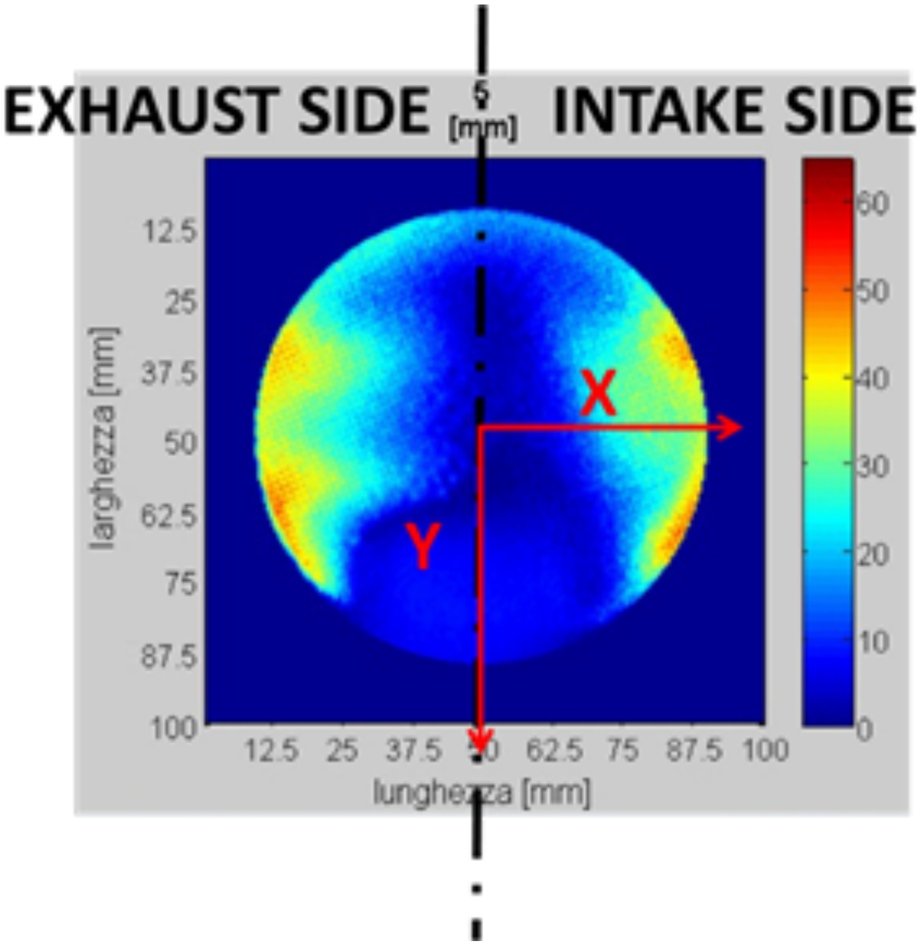

Fig. 3.4 Example output of HWA test with considered reference frame

3.1.1 Experimental HWA test procedure

figures 3.5 report the raw measurement of the tumble velocity obtained for the Biomethair cylinder head by means of the HWA technique. The measurement plane has been divided into four sectors and the position of the reference axes (which are the same as figures 3.3 and 3.4) has also been indicated for the reader's own convenience.

Based on Eqs. (3.2) and (3.3), the contribution to the tumble vortex intensity is given by sectors 2 and 4, corresponding to the exhaust side and the intake side, respectively. Given the symmetry of the intake-system configuration with respect to the x axis, the contribution from sectors 1 and 3 is ideally nil. In fact, any deviations from the symmetry is due to uncertainties in the measurement as well as to incertitude in component manufacturing and assembly. The measurements have highlighted that the 3 mm valve lift already causes the flow past the valve throat to be unevenly distributed (figure 3.5). Consistently, the mass-flow rate and the momentum pertaining to sector 3 are apparently higher than those of sector 4, thus leading to remarkable tumble intensity. This latter can easily be appreciated from figure 6 where the tumble number (evaluated according to Eqs. (3.2) and (3.3)) is reported as a function of the valve lift. The non-dimensional tumble intensity is virtually constant for lifts between 3 and 6 mm, thus denoting a remarkable and comparable deviation of the flow distribution from the symmetry. Such a behavior is mainly due to the properly designed masking surface on the intake side of the cylinder head. Further information on the intake-flow details can be inferred from the analysis of the CFD results and will be discussed later on.

As the valve lift further increases, the tumble rises and more apparent flow distribution unevenness is observed from the detailed measurements (see figure 3.7). Such behavior is to be ascribed to the combined effect of the port shape and of the flow inertia.

The Biomethair cylinder head has also been tested with the torque meter (Ricardo) method and the results obtained from the two techniques are compared in (figure 3.6 right). In order to guarantee for a larger consistency of the comparison, the results of two different prototype heads tested at CRF have also been included in the picture. (figure 3.6 right) shows that the Ricardo tumble number is comparable with the HWA one, the latter being on an average 10% smaller that the former one, thus assessing for similar abilities of the two techniques in capturing the 'integral' characteristics of the tumble motion. As a matter of fact, flow losses in the measurement devices affect the test results for both methods. In the Ricardo method setup [27], the tumble adaptor forces the flow to bend by 90 degrees, thus generating flow losses. Further friction losses occur in the conversion pipe between the adaptor and the honeycomb. On the other hand, with the HWA method the flow losses are mainly produced by the resistance offered by the flow straightener. It can be concluded that the HWA technique represents a factual alternative to the integral techniques for tumble characterization. Although it cannot be considered as a fully differential technique, it anyhow provides additional information about the flow distribution in planes perpendicular to the cylinder axis. Moreover, quantitative information on the unevenness of the flow distribution generated by the intake system is to be extracted from the measurements. Finally, as far as costs are concerned, the HWA apparatus and the Ricardo setup are almost equivalent.

3.1.2 Numerical Analysis

The HWA testing procedure is confirmed to be a suitable way for the experimental tumble measurement at test rig. Henceforth the goal of the work was to develop a numerical model based on the HWA test procedure and able to fit the experimental data. The production of a reliable numerical tool for the static tumble measurement is useful in order to have a deeper insight to the fluid dynamic phenomena and moreover gives the possibility to extend the experimental campaign such as testing different geometries.

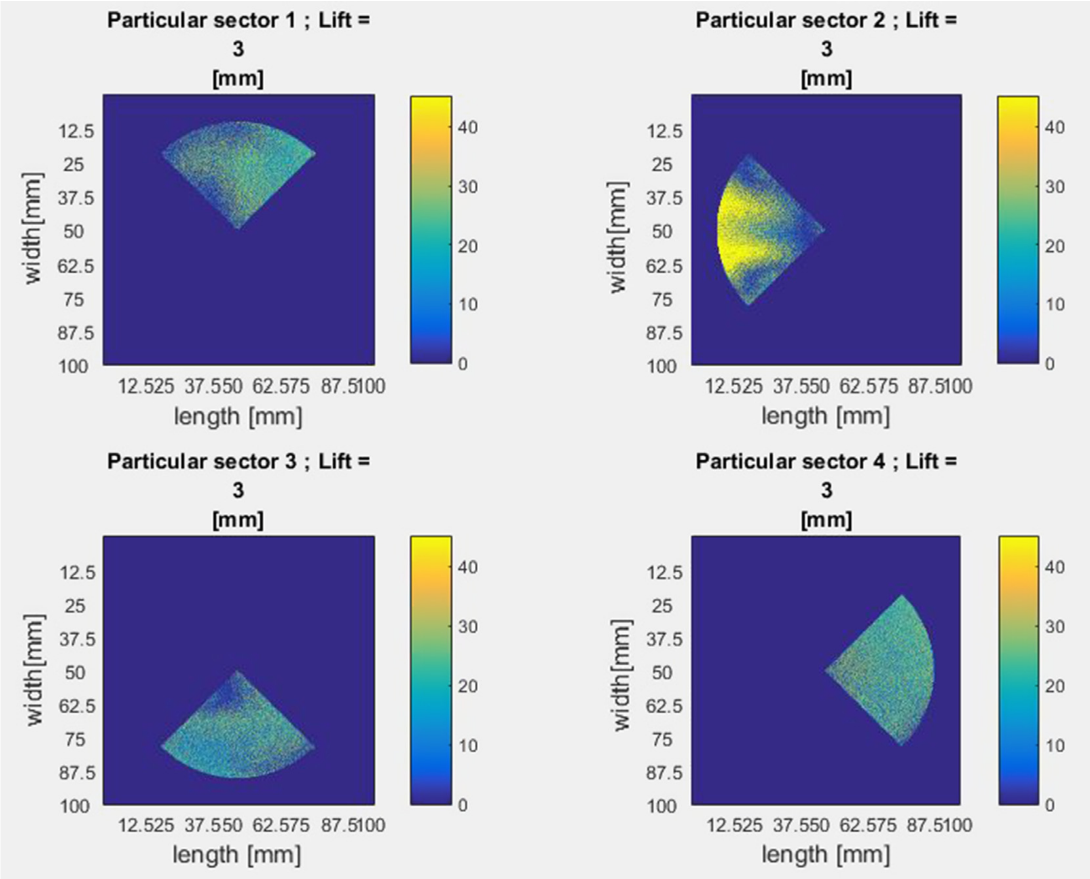

Fig. 3.5 Sectorwise Raw Tumble measurement through HWA technique, Valve Lift = 3mm

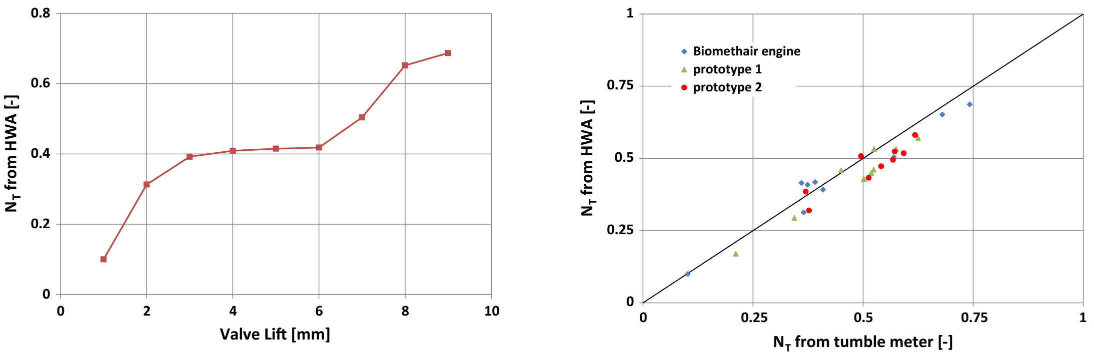

Fig. 3.6 Tumble Number value obtained by HWA procedure (left) - Ricardo method and HWA method comparison (right Figure)

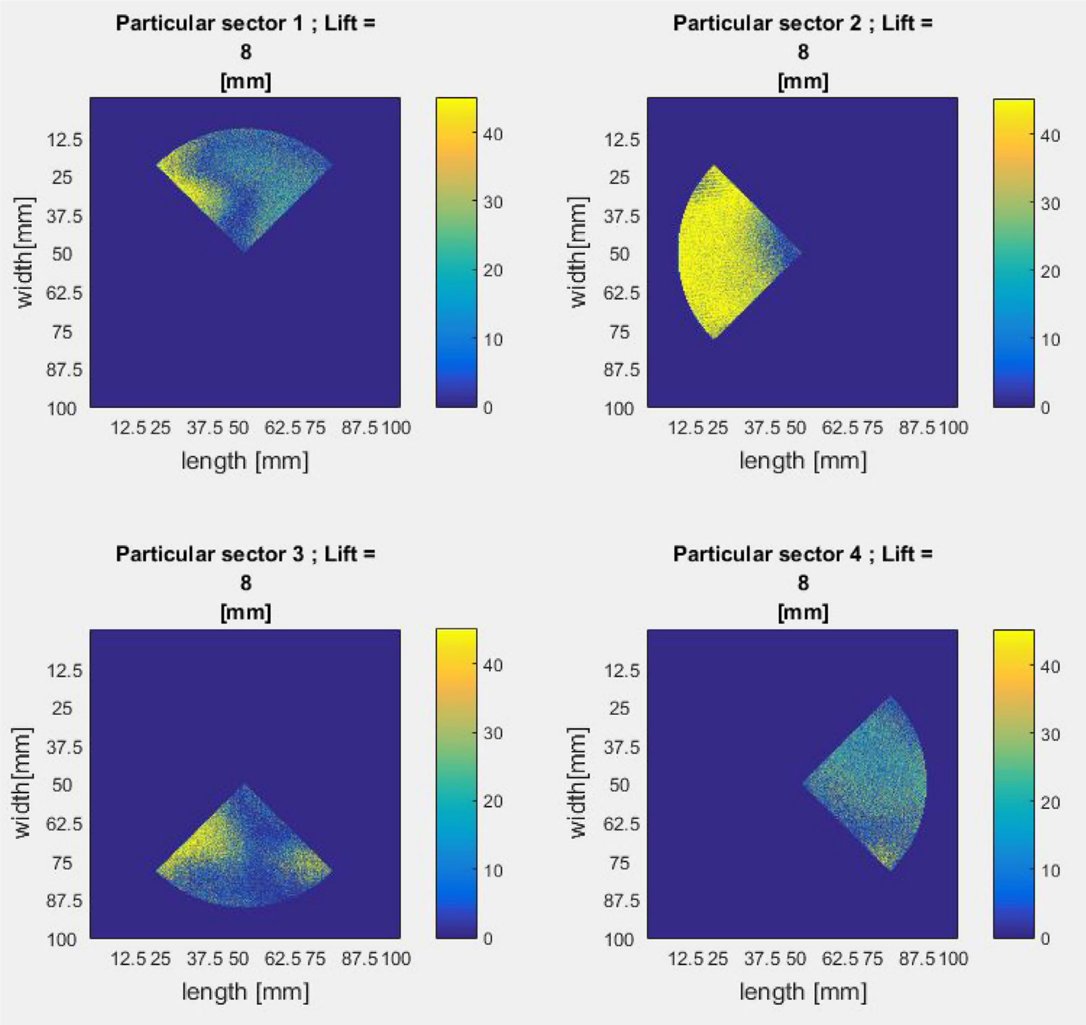

Fig. 3.7 Sectorwise Raw Tumble measurement through HWA technique, Valve Lift = 8mm

In the next section the complete model development, its validation based on the above mentioned experiments have been described. Finally such method for a preliminary study on the modified engine head has been applied.

3.2 Virtual flow bench Model

The CFD model for the simulation of the steady-state flow past the cylinder head, at fixed valve lift, has been developed within the Star-CCM + package [http://www.cd-adapco.com/products/starccm], version 8.06. figure 3.1 shows the CAD of the engine cylinder head, which has represented the starting point to derive the geometrical features of the ‘virtual flow box’ model. This model has been developed with specific reference to the experimental setup in figure 3.3. figure 3.8 reports the CAD representation of the fluid domain (figure 3.8 a) and the numerical grid that has been selected for the analyses (figure 3.8 b). The upstream plenum is represented by means of a spherical volume and the experimental stagnation conditions have been imposed at the inlet spherical surface (purple color in figure 3.8 a).

The flow straightener has in turn been represented in the model by means of an orthotropic porous region. The medium resistance along the X and Y directions (see Figs. 3.3 and 3.4) has in fact been set to extremely high values in order to mimic the behavior of the actual straightener. The computational volume extends beyond the straightener location up to a distance of 0.75 times the bore. Moreover, the region boundary conditions have been modified from a ‘wall’ to a ‘pressure’ boundary. The position of the HWA measurement plane is also indicated in figure 3.8 b.

Preliminary analyses have been carried out in order to optimize the model setup in terms of reliability of the solution algorithm. The available SIMPLE-type algorithm has been coupled to a ‘segregated flow’ solver [28] and to a transient formulation of the problem. More specifically, the pressure inside the computational domain has been initialized to the same pressure level as for the downstream environment and a ramp has been used to match the upstream stagnation pressure. The ramp duration is 0.1 s and the total simulation time is 1 s. This choice was made in order to maximize the model robustness. Still, the high nonlinearity of the flow equations can be difficult to be solved when coupled to complex physics and complicated geometries. Preliminary tests showed that the steady-state solver requires a careful flow initialization to allow for a reliable solution to be obtained. Such an initialization process can be iterative and time-demanding. Hence, it was decided to select a transient solver and to apply it to the abovementioned problem formulation. A second order upwind discretization scheme has been selected for the momentum, energy and turbulence equations. The second order scheme has actually been blended with a first order one with a factor of 0.5, whereas a first-order upwind has been adopted for the pressure evaluation. The detailed analysis of the grid independence as well as the investigation into the physics of the results is thoroughly presented in the Section 3.2.1

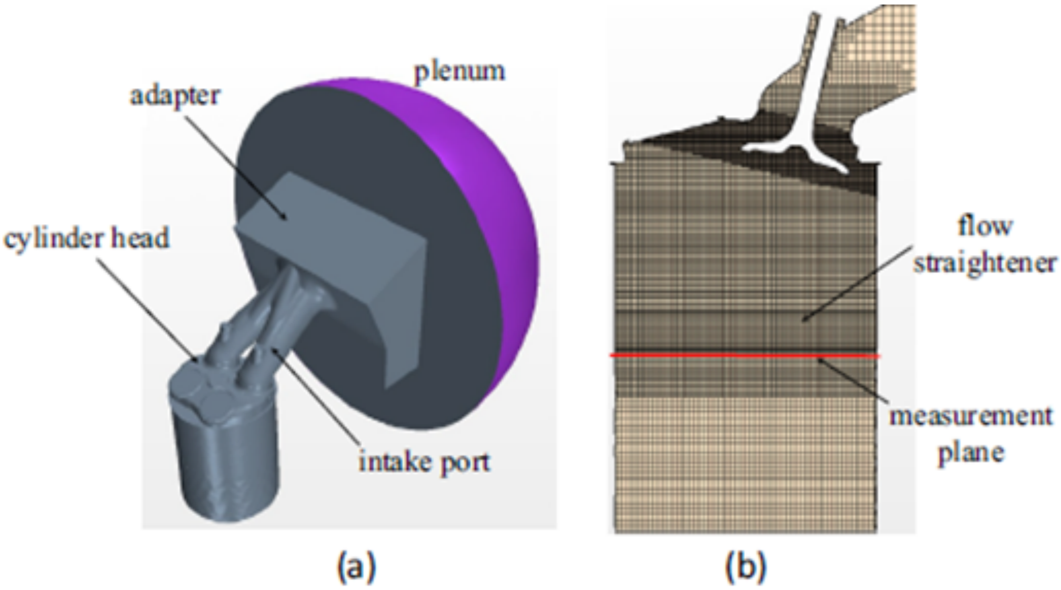

Fig. 3.8 a) Cad model of the 'Virtual flow box' b) Computational mesh view

Referring to the scheme in figure 3.8, the flow straightener has not been thoroughly modeled whereas its behavior has been reproduced by means of a proper porous region filled with an orthotropic medium. More specifically, a resistance tensor has been introduced, i.e., an appropriate 'resistance' term $\vec{S_P}$ was introduced in the momentum equations as a source term [28], such that,

$$\vec{S_P} = -(\widehat{P_V} + \widehat{P_i}.|\vec{V}|).\vec{V} \tag{3.4}$$

where $\widehat{P_V}$ and $\widehat{P_i}$ are the viscous and the inertial resistance tensors, respectively, and $\vec{V}$ is the local absolute fluid velocity. Referring to the frame of reference in Figs. 3.4, the straightener is hence meant to cancel the fluid velocity along the x and y directions. The z- component is only slightly reduced due to the friction effects. Accordingly, the resistance tensors of the equivalent orthotropic porous medium have been defined as follows:

$$\widehat{\mathbf{P}}_\mathbf{V} = \begin{bmatrix} 500 & 0 & 0 \\ 0 & 500 & 0 \\ 0 & 0 & 1 \end{bmatrix} \cdot p_V; \qquad \widehat{\mathbf{P}}_\mathbf{i} = \begin{bmatrix} 500 & 0 & 0 \\ 0 & 500 & 0 \\ 0 & 0 & 1 \end{bmatrix} \cdot p_i \tag{3.5}$$

The scalar coefficients in Eq. (3.5) should be calibrated based on the pressure drop in the real straightener. Given the lack of experimental measurements, a suitable CFD model of the straightener has been built up following the procedure shown in [29]. More in detail, the straightener honeycomb structure has been modeled and discretized in the code and the corresponding pressure drops have been derived through the CFD simulation of a 1D-like flow, for different velocities at the straightener inlet. Finally, the pressure gradients have been interpolated considering the following equation:

$$\frac{dp}{dx} = -(p_i.V^2 + p_V.V) \tag{3.6}$$

being V the 1-D velocity magnitude. The following coefficients have been obtained: pi = 200 kg/m3, pv = 1000 kg/m2/s. No additional calibration of the model was necessary, as detailed in Section 6.3.

3.2.1 Virtual flow box model validation

3.2.1.1 Turbulence model discussion

The correct prediction of the mean-flow and turbulence characteristics of an engine-like flow is a challenging task given the high level of anisotropy and recirculation as well as the wide range of length and time scales. Several approaches have been tested by many researchers in the last 20–25 years. The proposed modeling solutions range between the RANS (Reynolds-Averaged Navier Stokes) and LES (Large Eddy Simulation) frameworks.

In [30] the k-ζ-f model developed by Basara [31] was used for the steady-state simulation of the swirl or of the tumble flow through a cylinder head. The model proved to capture the numerical discharge coefficients with a 7–8% error with respect to the experimental ones. However, the model was able to capture the qualitative difference of the discharge coefficients measured by the swirl-meter and by the tumble-meter setup, respectively, for the same cylinder head. In [32] High Reynolds linear, non-linear and RNG-based k-ε models were used to simulate the intake flows, bridging the near-wall flow solution with wall functions. The EVM model constitutive relationship was found to be fundamental for predicting the flow characteristics as well as for evaluating the global performance parameters such as the discharge coefficients. Cubic stress-strain relation proved to provide the best agreement with the experimental data. In [34] High Reynolds and low-Reynolds cubic k-ε models were tested. The near wall treatment was found to play a key role in the prediction both of global flow patterns and performance parameters, such as the discharge coefficients, and of local flow pattern characteristics. The comparison with global and local experimental measurements at the steady flow bench was used to assess for the predictive capabilities of the models. The low- Reynolds approach, although increasing the computational demand of the simulations, was found to be fundamental to achieve a good agreement with the experimental data. In [34], steady state simulations of the intake system of a race engine head were carried out by using the Standard k-ε model with wall functions.

The results were considered to be satisfactory enough for the CFD model to be used to analyze and compare different test conditions. However, limitations of the considered approach were highlighted in the lack of application of low-Re formulations of the wall boundary layer, mainly to be ascribed to the required CPU and RAM resources.

The CFD activity here presented aims at characterizing the tumbling flow and its evolution in the HWA experimental setup as well as at providing a further contribution to the benchmarking of the state-of-the-art of turbulence models, with specific attention to the engine context. The turbulence model has hence been selected focusing not only on its potentialities in reproducing the specific features of the in-cylinder turbulence (e.g., anisotropy and flow curvature, unsteadiness, compressibility) but also on the feasibility of its implementation into the transient engine-chamber model. In particular, as far as the wall boundary layer treatment is concerned, the low-Re approach has not been considered. Such an approach would in fact require at least 15 cells close to the walls and would therefore turn out not to be feasible in a full in cylinder moving-mesh model. High CPU requirements and limitations of the current meshing tools can unluckily represent a serious constraint to CFD choices. 5 layers were thus defined at the walls and the two-layer approach [35] was followed for the boundary layer description. This solution was coupled to a 'blended' definition for the logarithmic wall functions [36], in order to guarantee a good modeling accuracy for all the possible y+ ranges. The thickness of the layer closest to the wall was selected so as the cell centroid falls within the laminar region. Two turbulence models have been selected and tested: the Realizable linear k-ε model [37] and the Standard cubic k-ε model [38]. Both models have been developed starting from the compressible version of the Standard k-ε model [39,40]. The Realizable model features a modified transport equation for the dissipation ε as well as strain-dependent formulations for the C_l and $C_{,}e1$ coefficients. Consequently, the model is able to account for the turbulence anisotropy and to meet the so called 'realizability constraints' for the normal stresses. The Cubic k-ε model extends the Boussinesq relation into a series expansion of the strain and rotation tensors so as to take the flow anisotropy into account. Specific attention has been paid to the effects of the streamline curvature on the turbulent stresses [41]. The RNG k-ε model [42] was not considered in this preliminary phase as it was not available in Star-CCM+ v. 8.06. Still, given the importance it retains for the simulation of IC engines [43,44,45], it has been considered within the STAR CD v4.20 package.

3.2.1.2 Grid independence analysis

In order to consider the dependence of the results on the computational grid, different models have actually been tested. The models are characterized by a few properly defined reference regions for the mesh refinement, as well as by the corresponding cell size (see figure 3.9). The considered cell size values are reported in Table 3.2. A first refinement region has been defined embracing the whole cylinder region and the intake ports ('Cylinder 1' in figure3.9) and the reference cell size has been set to 1.25 mm. The region labelled as ‘Cylinder 2’ includes the intake ports and the cylinder volume down to about 10 mm below the measurement plane. Finally, ‘Cylinder 3’ involves the valve curtain region.

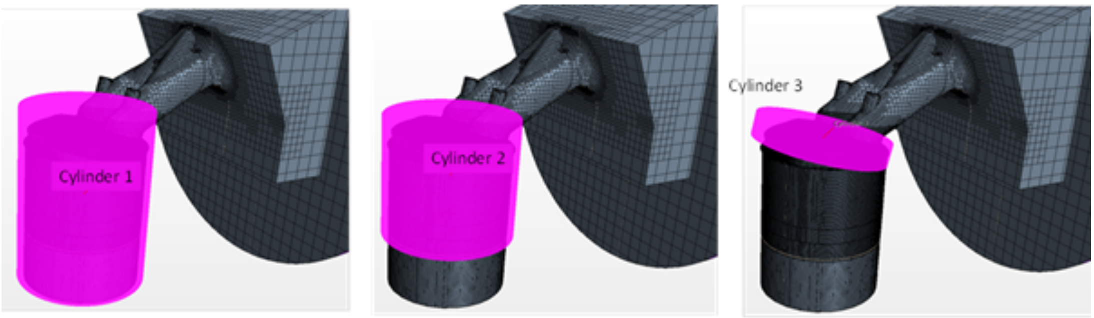

Fig. 3.9 Grid independence Test - Mesh refinement of various regions

The influence of the computational mesh on the code results will be shown in what follows with reference to a valve lift of 7 mm. The tests have been carried out to assess for the grid independence with both the Realizable and the Standard cubic k-ε models. The results are reported in figure 3.10 and are expressed as percentage errors with respect to the finest mesh (‘Refined III’) results. As far as the predicted mass-flow rate (black lines in figure 3.10) is concerned, the resultant mesh dependence is weak for both models. In fact, an error reduction from 2% to 1% is obtained by replacing the ‘Coarse’ mesh with the ‘Refined II’ (Table 3.2). As far as the influence of the adopted turbulence model is concerned, a slightly slower ‘rate of convergence’ arises for the Standard cubic model. The error produced by the Realizable model in the tumble evaluation ranges around a 2% for the ‘Refined I’ mesh and reduces down to a 1% for the ‘Refined II’ mesh. One should recall that such a refinement involves the adoption of a fairly small cell size (0.313 mm) in the valve throat region (Cylinder 3 in figure 3.9). This size corresponds to a half the size of the ‘Refined I’ mesh in the same region. The extension of such a degree of refinement to the Cylinder 2 region produces a change in the tumble error by a 1%, mainly to be ascribed to the reduced numerical viscosity in the cylinder. Still, this is accompanied by a significant increase in the cell count (see Table 3.2). According to the right chart in figure 3.10 the dependence of the NT predicted by the Standard cubic k-ε model on the mesh degree of refinement is larger than that produced by the Realizable model. In addition, the non-monotonic trend represents an additional issue of the Standard cubic k-ε model with respect to the Realizable one. The change in cell size around the valve curtain area (Cylinder 3) leads to a decrease in the error from about 7% to about 4%. The refinement in the region between the valve and the measurement plane (Cylinder 2) holds a greater influence on the predicted tumble intensity for the Cubic than for the Realizable model.

Table 3.2 Mesh refinements studied for grid independence test

Mesh	Base Size [mm]	Size in Cyl.1 [mm]	Size in Cyl.2 [mm]	Size in Cyl.3 [mm]	Approx. cell count
Very course	10	-	-	0.625	400,000
Course	10	1.25	-	-	800,000
Refined I	10	1.25	0.625	-	2,400,000
Refined II	10	1.25	0.625	0.313	4,200,000
Refined III	10	1.25	0.313	0.313	14,900,000

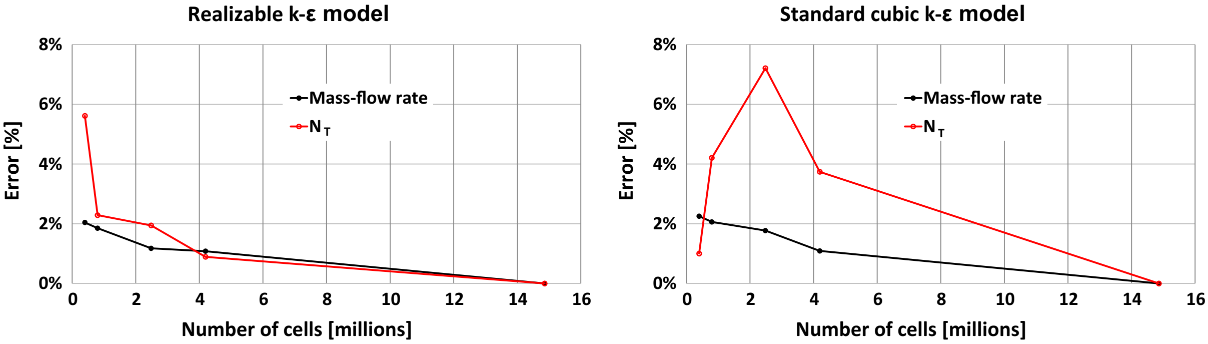

Fig. 3.10 Grid independence study for the ‘Virtual Flow Box’ model with lift = 7 mm: percentage difference with respect to the ‘Refined III’ mesh for the Realizable (left) and the Standard cubic (right) turbulence models

The Standard cubic model turns out to be more demanding in terms of mesh density than the Realizable one. The results of the Realizable model are in fact mesh independent when the ‘Refined II’ mesh is adopted. As a matter of fact, both the mass-flow rate and the NT error float below 1%. On the contrary, the Standard cubic model achieves a good mesh-independence for the mass-flow rate with the given mesh refinement whereas it would require a mesh finer than the ‘Refined III’ to be tested to assess for a complete mesh independence. Such a refinement would imply an excessively high computational effort. Thus, in order to perform a direct comparison between the two models, the analyses have been carried out with the ‘Refined II’ mesh, this latter allowing for a reasonable reliability of the results with both turbulence models. As far as the wall treatment is concerned, all the meshes featured 5 extrusion layers and the thickness of the layer closest to the walls was such that the non-dimensional wall distance y+ turned out to be between 1 and 2. This was consistent with the adoption of a two-layer approach with ‘blended’ wall functions.

3.2.1.3 Results Validation

The results obtained with the ‘virtual flow box’ are presented hereafter and allow for getting an insight into the model capabilities in capturing the tumbling flow features . The ‘virtual flow box’ model validation results are presented in Figs. 3.11-3.13. More specifically, figure 3.11 reports the comparison between the experimental and the simulated integral parameters, namely, the discharge coefficient and the tumble number. Figures 3.12 and 3.13 are instead focused on the comparison of the detailed tumble (axial) velocity profiles for two representative lift values, i.e. 4 mm and 8 mm.

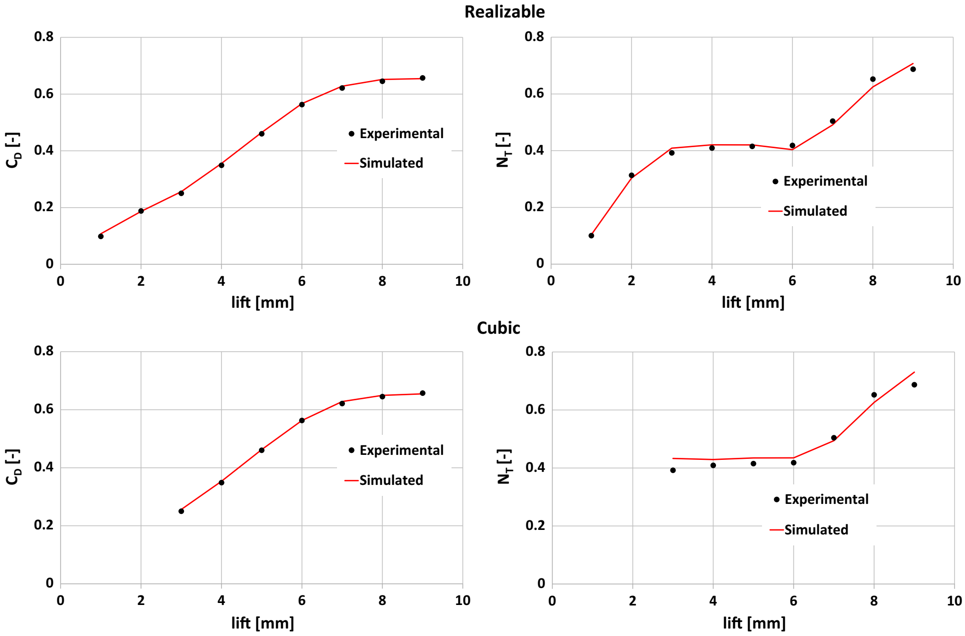

Fig. 3.11 ’Virtual Flow Box’ model validation for Realizable (upper row) and the Standard cubic (lower row) k-ε models: Discharge coefficients (C_D) and Tumble number (N_T) for ’Refined II’ computational mesh

The results in figure3.11 highlight the satisfactory accuracy of the two models in the prediction of the discharge coefficients. However, the NT coefficients produced by the Standard cubic model feature a weaker agreement with the experimental results for the 3 mm and 9 mm lifts. Moreover, despite the use of a lower time step (0.25 instead of 1 ms), which in turn resulted into higher computational costs, the simulation with the Cubic model could not reach convergence for lifts below 3 mm. In addition, the integral parameters for any of the considered lift have not reached stabilized values at the end of the simulated-transient (1s) and the residuals associated to each of the equations have remained well above the convergence threshold. This behaviour proves an increase in the model stiffness and constitutes a drawback of the Cubic model with respect to the Realizable one.

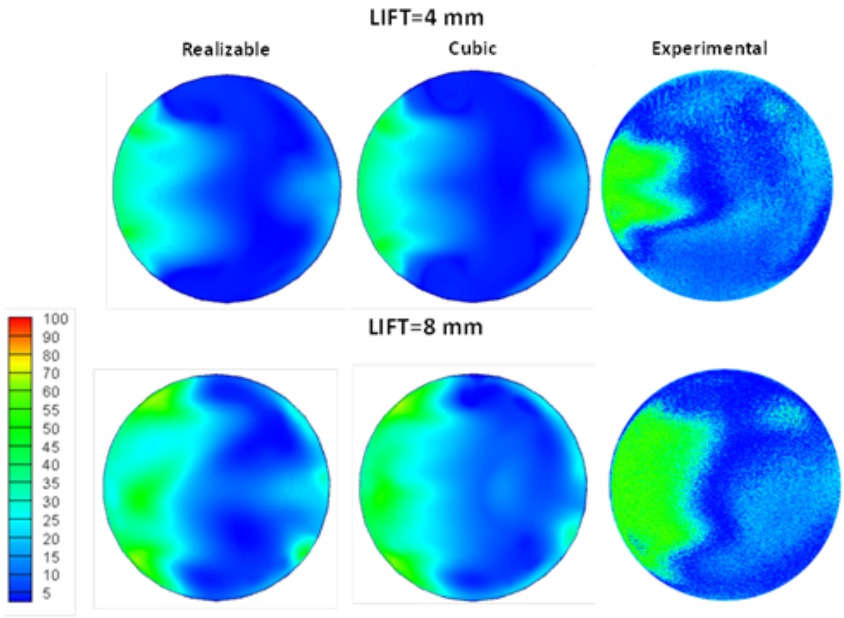

Fig. 3.12 ‘Virtual Flow Box’ model validation for the Realizable (left column) and the Standard cubic (middle column) k-ε models: Contours of axial velocity measured in z-plane – Computational mesh = ‘Refined II’: Experimental results from HWA technique (Right column). Validation is shown here for 4mm (Top row) and 8mm (Bottom row) valve lift

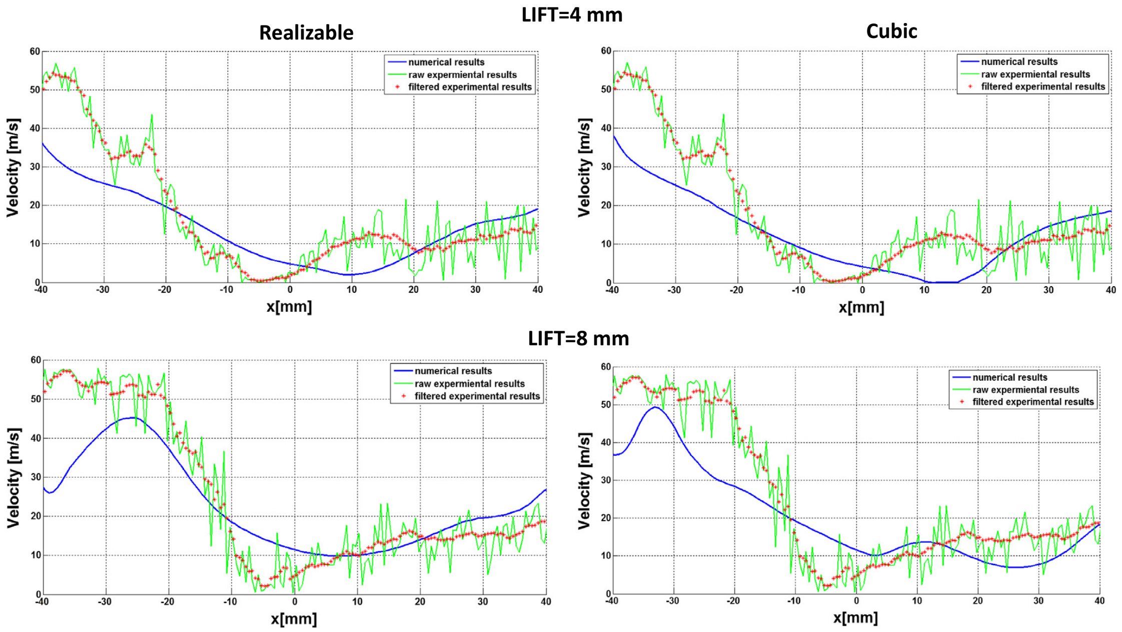

Fig. 3.13 ‘Virtual Flow Box’ model validation for the Realizable (left column) and the Standard cubic (right column) k-e models: Patterns of axial velocity measured in y = 0 plane – Computational mesh = ‘Refined II’. Raw Experimental values (Green line); Filtered experimental velocities (red dots).Validation is shown here for 4mm (Top row) and 8mm (Bottom row) valve lift

Figures 3.12 and 3.13 should be interpreted and considered within the actual frame and goal of the present activity. As a matter of fact, the focus has been mainly set on the matching, with a satisfying accuracy, of global quantities such as the CD and NT quantities whereas minor attention has been devoted to the prediction of the actual flow pattern at any stage throughout the engine cycle. The comparison between the patterns in the experimental and in the predicted isolines of the axial velocity (figure 3.12) reveals that a consistently accurate solution has been achieved for both models.
Still, it is worth observing that the numerical simulations produce spread out high-velocity regions, such a feature being enlarged by the Standard cubic model outputs. Figure 3.13 shows the comparison between the measured and the predicted profiles of the axial velocity in the measured plane for y=0. The solid green line represents the 'raw' experimental velocities, the red circles refer to the filtered experimental velocities (produced by means of a moving average filtering technique) whereas the solid blue line addresses to the simulated velocities. Despite the apparent and local mismatches between numerical and experimental values, both models prove to be capable of capturing the essential features of the flow, i.e., higher velocities close to the external bounds corresponding to the direct and to the reverse tumble velocities.
However, a sound exception is represented by the calculated velocities between x=-30 and -40 mm (exhaust side) where the flow is affected by the boundary layer close to the left side of the cylinder wall. Given that the errors are virtually alike for both turbulence models, the reason for such mismatches is mostly likely to be ascribed to the near-wall treatment. This is in agreement with some of the findings in the literature [46, 47]. It is worth pointing out that, in the present work, specific attention has been paid to the feasibility of the model implementation in a transient simulation of a complete engine cycle. Consequently, despite their accuracy, the low-Re approaches for the wall boundary conditions have not been considered. Still, the accuracy arising from the results presented in Figs. 3.11-3.13 assesses the capability of the model to capture the integral features of the tumbling flow (figure 3.11). The model can thus be used as a predictive tool to gain further insight into the tumble flow characteristics as well as to assess the impact of the cylinder-head design variables on the tumble intensity. Finally, another significant remark has to be made about the Cubic model. In fact, from a theoretical point of view, this latter is supposed to allow the eddy-viscosity models to account for the flow anisotropy and curvature to a greater extent with respect to linear models. However, from a practical point of view, the Standard cubic model has not proved to appreciably improve the accuracy of the results with respect to the Realizable model. Similar conclusions were found in [46] with reference to swirl and squish flow conditions. Moreover, the increased computational cost and instability constitute a strong drawback.

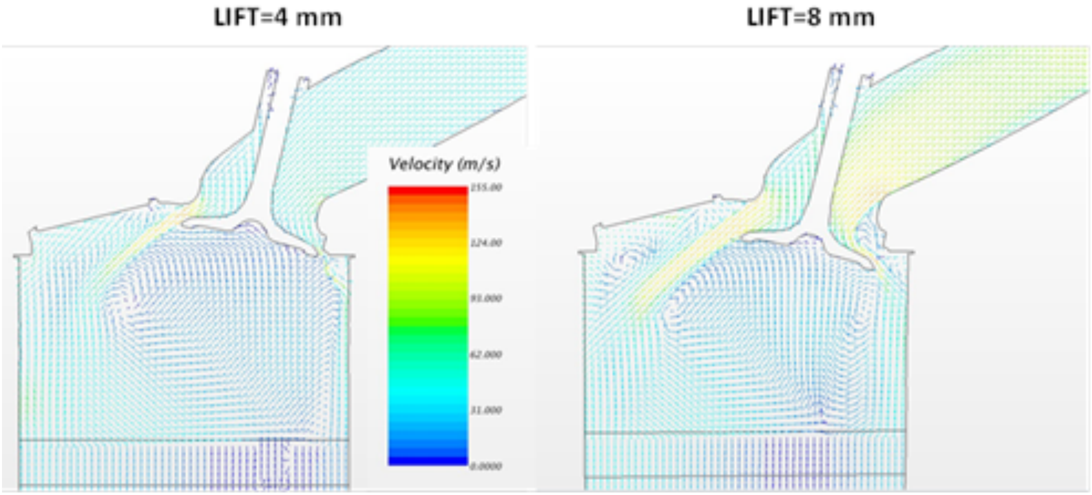

Fig. 3.14 Steady-state flow past the intake valve at fixed lift: 4 mm (left), 8 mm (right)

Figure 3.14 depicts the evolution of the flow issuing from the intake valve under steady-state conditions. The results are reported for two different lift values, i.e., 4 mm (Figure 3.14 a) and 8 mm (Figure 3.14 b). Consistently with the HWA experimental results (see Figs. 3.5-3.6), the flow features a considerable tumble number in the considered lift range mainly thanks to the flow distribution unevenness with respect to the valve axis.

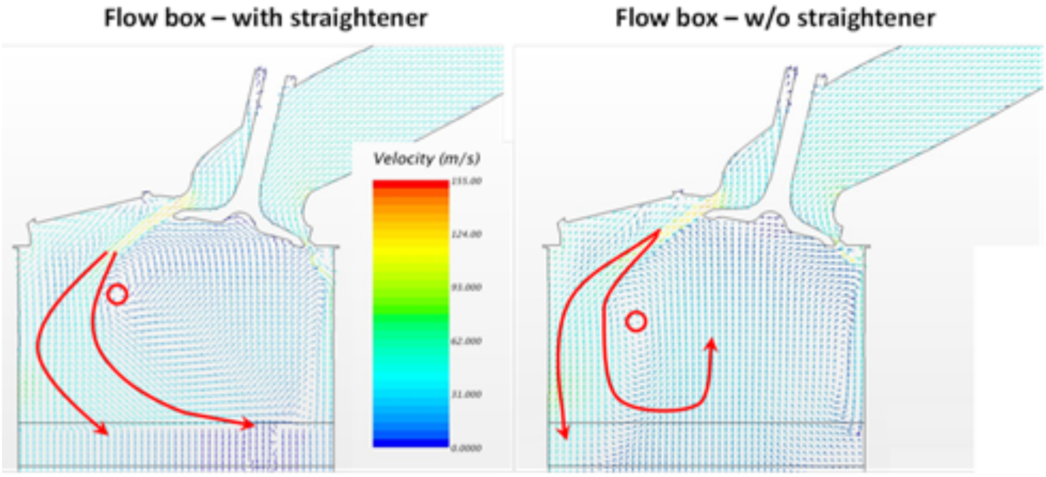

Fig. 3.15 Comparison of the flow fields in the virtual flow box with and without flow straightener : valve lift (4 mm)

Figure 3.15 shows the intake flow patterns obtained in two cases for the same valve lift (4 mm). The first case (Figure 15a) refers to the steady state flow in the HWA test rig and hence basically represents the same flow field as for figure 3.14 a. The second flow map (Figure 3.15b) has been obtained under steady state conditions, removing the flow straightener from the numerical model. More specifically, the porosity of the cells corresponding to the straightener in the computational domain has been removed and the region has simply been modelled as a fluid region. The comparison between Figure 3.14b and 3.15b thus offers a substantial estimation of the flow perturbation introduced by the straightener. The comparison of the first and of the second picture in figure 3.15 accounts for the changes in the flow pattern produced by the straightener. As a matter of fact, the resistance induced by its small pipes not only constitutes an additional flow resistance but also decouples the cylinder environment from its surroundings to some extent. When the straightener is not included in the model (figure 3.15b), the cylinder is directly connected to the downstream ‘pressure’ boundary, which is allowed to reflect waves and to feed the low pressure zones with fluid. This has a remarkable impact on the streamlines aspect. As a matter of fact, the velocities close to the axis turn out to be upwardly directed, thus causing the direct tumble to be shifted both downwards and towards the exhaust side (refer to the position of the red circle and of the red arrows). On the other hand, the straightener inhibits the pressure boundary effect and the flow hence is downwardly directed almost everywhere. It is worth highlighting that such a finding is in agreement with the experimental measurements. The results produced by the different measurements techniques and the corresponding numerical simulations provide a qualitative insight into the in-cylinder flow field despite the mismatches that arise from a quantitative point of view. A thorough and detailed analysis of the in-cylinder flow field is mandatory to achieve a better understanding of the phenomena that define the engine behaviour throughout the whole engine cycle and specifically during the combustion process.

3.2.2 Numerical Assessment of the intake masking effect

Once the baseline model has been built and validated against the experimental data the tool was considered robust enough to extend the experimental testing campaign to a different cylinder head. The second head variant (figure 3.1) has been derived from baseline removing the intake masking, the expected result from this modification is an increase in volumetric efficiency due to the reduction of local losses at the valve curtain with a possible negative effect in turbulence due to a reduced tumbling behavior of the intake flow. The two contrasting phenomena described above should be carefully evaluated and balanced for a proper design of a high performance engine, this is even enforced for a gaseous fuel that, with respect to a traditional gasoline engine, tends to have a lower ignitability and most of all cause a lower volumetric efficiency for lack of evaporation.

To that end the virtual model developed here effectively replaces the experimental activity.

Using the same approach described in the previous section the results with the Masked and the Non-Masked head have been compared. The synthetic results are presented in figure 3.16, the solid lines represent the Tumble Number value as function of the lift while the dashed line are the corresponding values of discharge coefficient.

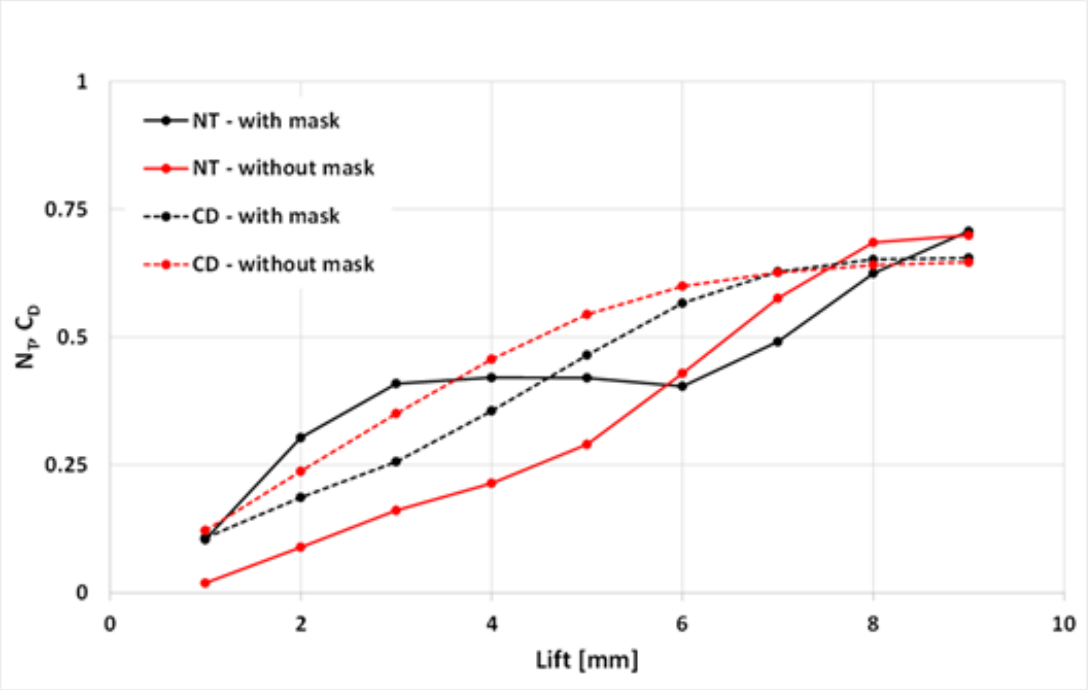

Fig. 3.16 Tumble Number, N_T (Solid line) and Discharge Coefficient, C_D (Dashed line) versus valve lift. Masked : Black colour, No-Mask: Red colour

The Masked head shows a better performance in tumbling formation at lower valve lift from 1 to 5 mm, the trend is then inverted at higher lift even if the differences between the two solutions reduce and finally converge to the same value at maximum lift (9 mm).

It is interesting to note the different behavior for the two geometries: the masked case shows a maximum and then a trend inversion while the No-Masked variant increases its Tumble Number over all the lift range. This is explained considering that for lift higher than 4mm the valve overcomes the mask obstruction reducing the masking effect on the flow as it is confirmed in figure 3.16 where the velocity vector plots are considered at 4 and 8 millimeters of valve lift

For the 4 mm valve lift (left picture in figure 3.14), the flow past the valve on the intake side (right side) is inhibited by the presence of purposely designed masking wall on the cylinder head downstream from the valve curtain surface. As a result of it, the ‘direct’ tumble (anticlockwise tumble) extends over the whole domain delimited by the cylinder and the straightener. At a higher valve lift (8mm - figure 3.14b) the valve has been displaced beyond the extension of the masking wall, thus dramatically reducing its effect. In fact, a clockwise vortex (‘anti tumble’ or ‘reverse tumble’) forms close to the valve plate on the intake side. However, the intensity of the direct tumble too increases thanks to the increased flow velocity in the intake runner and to the higher flow momentum acting against the curvature of the streamlines towards the intake side of the valve. The intensity of the direct tumble thus increases more than that of the reverse tumble as a result of the greater flow asymmetry. For what concerns the discharge coefficient, as it was expected, higher losses are introduced with the masked head, nevertheless the differences between the two variants is not dramatic. Anyway, it can easily be recovered by using a slightly higher boost pressure in case of necessity. Moreover, the positive impact on combustion given by the increased turbulence level could more than offset the volumetric lost as it is described in the next section.

3.3 Engine Numerical Model

The use of a steady state flow rig is only partially representative of the actual in-cylinder flow since the flow pattern inside the chamber is actually affected by the induction stroke history from IVO to the considered crank angle position. Furthermore, given the considerably high compression ratio of the considered engine, the piston is very close to the cylinder head in the first period of the intake phase thus causing the entering tumble flow to impinge on it modifying the direct tumble formation.

In agreement with the literature conclusions [42, 48] the results produced by different static measurement techniques and the correspondent numerical simulations provide a qualitative insight into the in cylinder flow, while fully quantitative results cannot be drawn from steady-state data.

A complete engine model investigation is then mandatory to achieve a better understanding of the phenomena that define the engine behaviour throughout the whole cycle and specifically during the combustion process.

3.3.1 Model Presentation

The CFD model for the transient simulation of the in-cylinder tumbling flow and combustion is represented in figure 3.17. More specifically, figure 3.17a reports an overall look at the adopted computational mesh whereas figure 3.17b shows the in-cylinder mesh layout at the engine BDC. The model has been built using the es-ice tool available in the Star-CD v4.20 package. In analogy with the settings exploited for the virtual flow box model, the second-order MARS differencing scheme has been selected for the discretization of the momentum, energy, turbulent kinetic energy and dissipation rate conservation laws. A 0.5 blending factor has been adopted. The first-order upwind difference was used for the pressure equation. The Realizable, the Standard cubic and the RNG k-ε models have been tested in the present work. One extrusion layer has been adopted close to the walls and the wall function in the formulation of Angelberger et al. [50] has been adopted for the near-wall boundary conditions. Such a choice has been mainly determined by two factors. First, the implementation of the same wall treatment as in the ‘virtual flow model’ has not been possible due to the fact that the use of the Star-CD two-layer formulation is only pertinent for highly refined boundary layer discretization (i.e., at least 15 layers). Second, unlike standard wall functions, the Angelberger one was specifically formulated for IC engines and it is claimed to account for the influence of a strong temperature gradient in the near wall region. Thus, it turns out to be recommended for IC engine simulations involving combustion. The thickness of the extrusion layer has been calibrated so as to achieve y+ values ranging between 30 and 100.

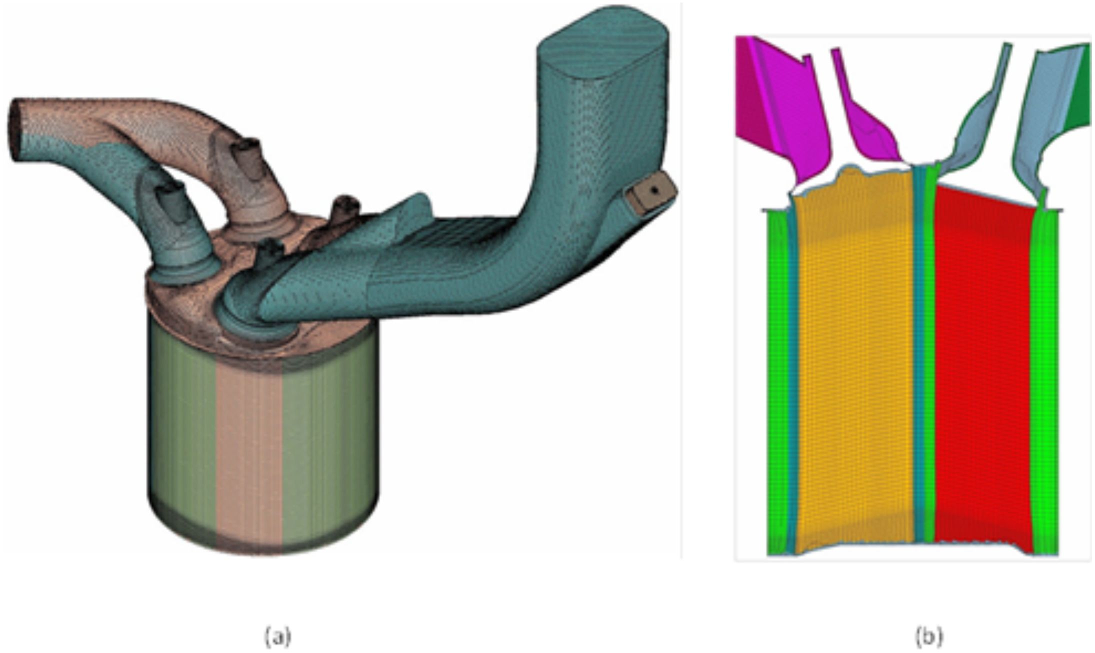

Fig. 3.17 Engine mesh (a), In-cylinder mesh layout at BDC (b) Plane clip at valves (YZ plane)

3.3.2 Grid independence analysis

In analogy to what performed for the virtual test rig a grid independence test has been performed for the transient engine simulation. A preliminary grid assessment has performed in [51] comparing the performances of three different grids under motored conditions.

The main characteristics of the three grids used in the independence analysis are summarized in table 3.3, since the semi-automatic mesh procedure adopted in Es-Ice version 4.20 allows an indirect control for the mesh size [52], a reverse meshing approach has been adopted to set the nominal cell height respectively to 1.2, 1 and 0.8 mm for the Coarse, Intermediate and Fine mesh.

An overview of the outcomes is reported in figure 3.18; the Tumble Number evaluation is presented for all the three meshes and it is possible to appreciate the difference in the results from the Coarse to the Intermediate mesh, while a reasonable good grid independence can be claimed between the Intermediate and Fine mesh. The small difference in the first part of intake phase can be considered as negligible since it is totally recovered during the following

Table 3.3 Grid independence test: Summary of mesh characteristic and relative computational time

Mesh refinement	No. of cells	Computational time
Fine(baseline)	$1.68 * 10^6$	$\approx$ 55hrs
Intermediate	$8.08 * 10^5$	$\approx$ 22hrs
Coarse	$3.47 * 10^5$	$\approx$ 16hrs

phase that is of major interest for combustion simulation; a further check on this purpose has been performed considering only the two more refined grids and running a complete test with combustion figure 3.19, this check confirms the good correspondence between the two setups, moreover the significant reduction in computational time enforces the choice of the intermediate grid solution.

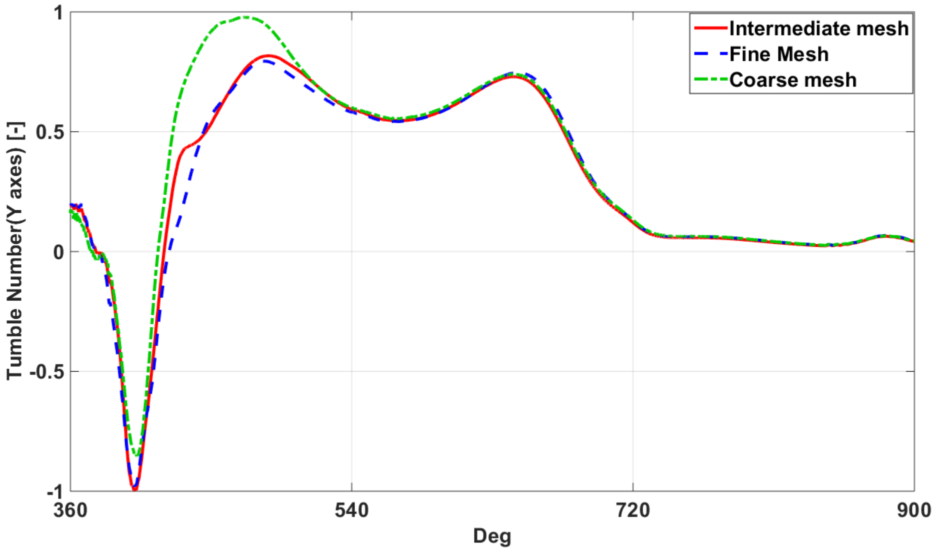

Fig. 3.18 Grid Independence test: Tumble number along Y-axis as function of crank angle degree. Coarse mesh (green dashed line), Intermediate mesh (red solid line), Fine mesh (blue dashed line)

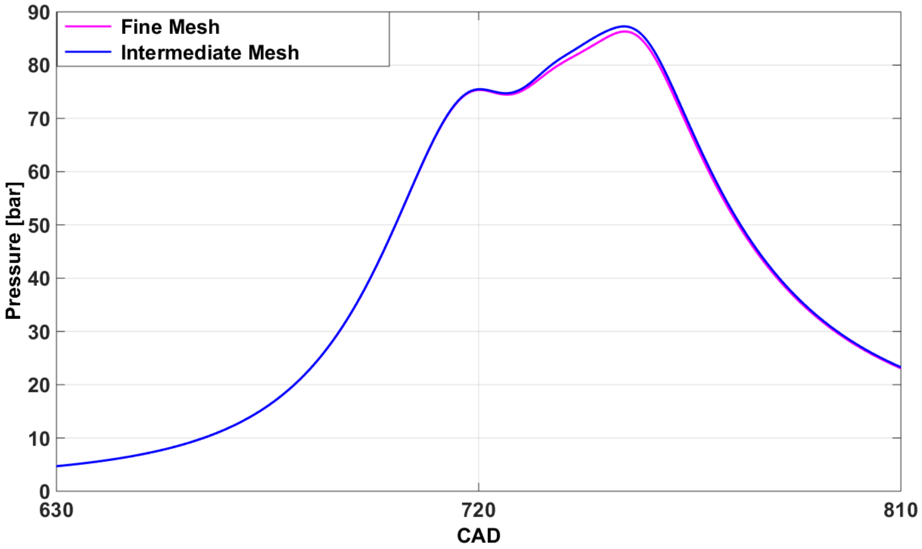

Fig. 3.19 Grid independence test: In-cylinder Pressure vs Crank angle degrees. Fine mesh (Red), Intermediate mesh (Blue)

3.3.3 Combustion Model: Sensitivity study and calibration procedure

The ECFM-3Z model [53] has been used in the present work to simulate the combustion process. Such a model is based on a flamelet assumption where the Flame propagation is described by a transported quantity called Σ that represent the Flame surface per unit of volume. The transport and production of the sigma variable are physically driven by two main factors: the turbulence level and the laminar flame velocity.

In the present work the ECFM-3z model has been applied considering an homogeneous and stoichiometric engine fueled with methane and the Gulder [54] experimental correlation been used for the evaluation of the laminar flame speed. Given the lack of information in literature about the usage of ECFM-3z model in such typology of engine, a sensitivity analysis on the parameters and a fine model calibration has been needed to validate the model. The Gulder correlation provides the laminar flow speed starting from a reference velocity and taking into consideration the actual thermodynamic condition in the chamber

$$S_l = S_{l_{ref}} \left(\frac{T_u}{T_{u_{ref}}} \right)^{\gamma} \left(\frac{P}{P_{ref}} \right)^{\beta} (1 - 2.1Y_{dil}) \tag{3.7}$$

where

$$S_{l_{ref}} = \omega \phi^{\eta} \exp\left[-\xi (\phi - 1.075)^2 \right] \tag{3.8}$$

where ω, ξ and η are user-supplied constants appropriate for the fuel and oxidizer used in the simulation,T_u is the unburned temperature, Tu_{ref} is the reference unburned temperature, P

T_{u-ref}	P_{u-ref}	ω	η	ξ	γ	β
298 K	1013525 pa	0.4220	0.150	5.18	2	-0.50

Table 3.4 Methane specific values of Gulder constants

is the pressure, P_{ref} is the reference pressure, $Ydil$ is the mass fraction of the diluted species, temperature (γ) and pressure exponents (β) are defined below whereas the Gulder constants are mentioned in Table 3.4.

$$\gamma = \gamma_{ref} - 0.8(\phi - 1) \tag{3.9}$$

$$\beta = \beta_{ref} + 0.22(\phi - 1) \tag{3.10}$$

For what concerns the ECFM transport equation, it can be synthetically written as [53]

$$\frac{\partial \Sigma}{\partial t} + \frac{\partial u_i \Sigma}{\partial x_i} = \frac{\partial}{\partial x_i}\left(\frac{\mu}{S_C}\frac{\partial(\Sigma/\overline{\rho})}{\partial x_i}\right) + (P_1 + P_2 + P_3)\sum - D + P_k \tag{3.11}$$

Where μ is the laminar viscosity, S_c is the Schmidt number,
$P_1(= \alpha K_t)$ represents the flame surface density production by turbulent stretch,
$P_2(= \frac{2}{3}\frac{\partial \widetilde{u'_i}}{\partial x_i})$ is the flame surface production by mean flow dilation ,
$P_3(= \frac{2}{3}\overline{S_L}\frac{1-\widetilde{C}}{\widetilde{C}}\Sigma)$ models the effects of the flame thermal expansion and curvature ,
$D(= \beta\overline{S_L}\frac{\Sigma^2}{1-\overline{C}})$ represents the flame destruction due to consumption,
P_k is the source term (such as a spark plug), S_L is the laminar flame speed, $\widetilde{C}$ is the mass progress variable and $\overline{C}$is the volume progress variable.
A major role in the model calibration is played by the term αK_t. Such a term represents the flame production by turbulent interaction where α is a model constant and k_t is the ITNFS function [55]. While the α coefficient is a tuning parameter used in the model calibration.
In addition to the ECFM transport equation and its parameters a strong role in the combustion simulation for internal combustion engines is also played by the ignition model which affects the heat release rate in the flame development phase. In the presented model, the so called “standard model” [52] has been used as ignition model, for which a tuning can be needed especially at low load condition when the combustion energy released at the spark has a higher relative importance with respect to the overall heat release.
All the cases have been calibrated comparing the pressure curve obtained from simulation with the correspondent experimental value obtained from ensemble averaging at test bench, figure 3.20. In all the cases the maximum error on the peak pressure has been kept below 3.5% on a percentage base and in any case never larger than 2 bar. A further check for the model calibration has been fixed on the heat release curve in particular on the mfb50 value that never differs from the experimental one for more than 0.5% (3 deg maximum). A part from the synthesis values

reported above as a threshold, the “shape” of the above mentioned curves has always been taken into account in order to avoid a “stiff” calibration procedures that may lead to non-physical results.

The strong effect of the calibration parameters in the combustion simulation in the pressure and apparent heat release plots is presented in figures 3.21 and 3.22, which show a reference case where the alpha parameter has been swept from the original recommended value 1.6 up to the value 1.2.

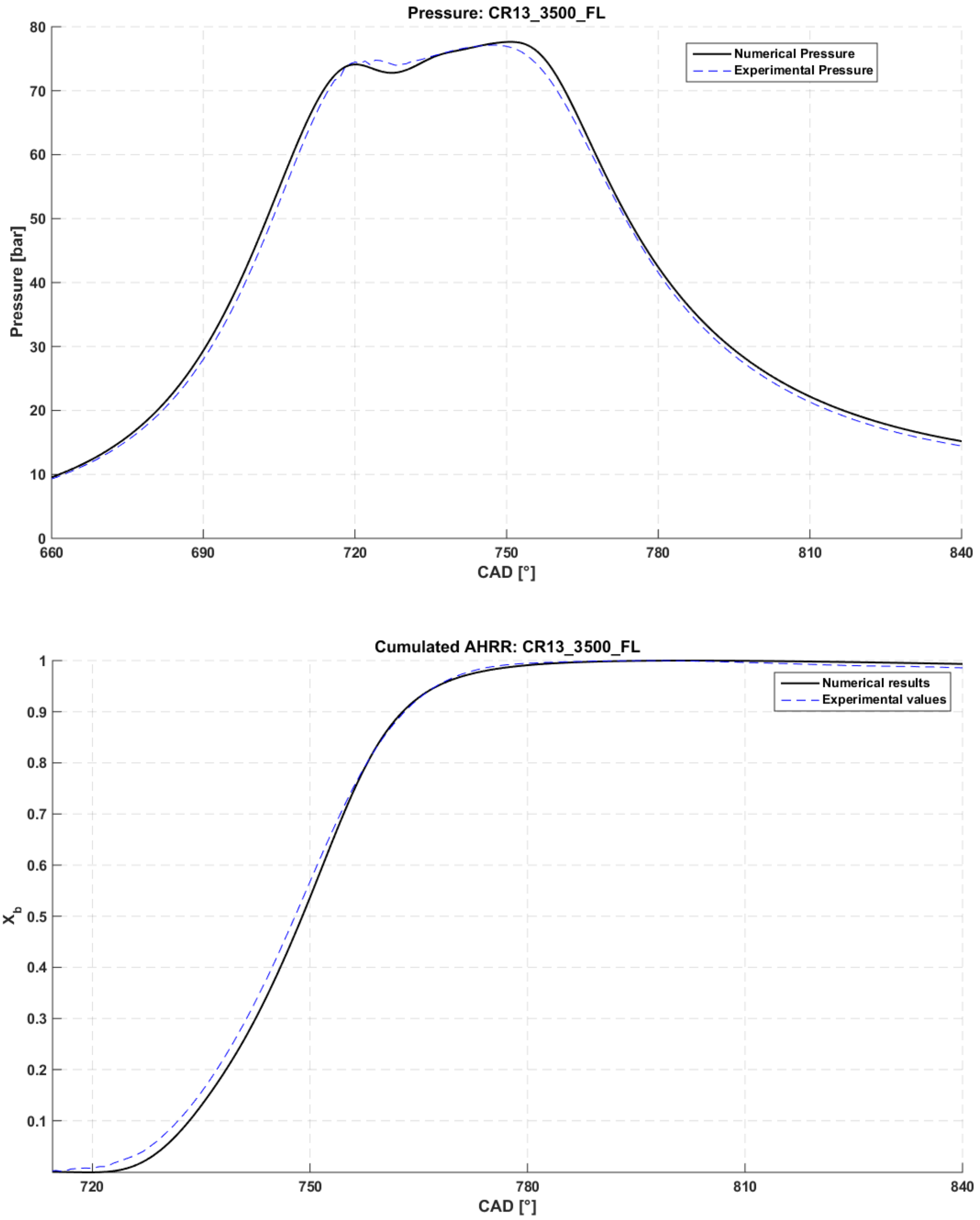

Fig. 3.20 Calibration case example. In-cylinder pressure (TOP), Apparent heat release rate X_b (Bottom). Experimental value (Blue dash line), Simulation result (Solid black line).

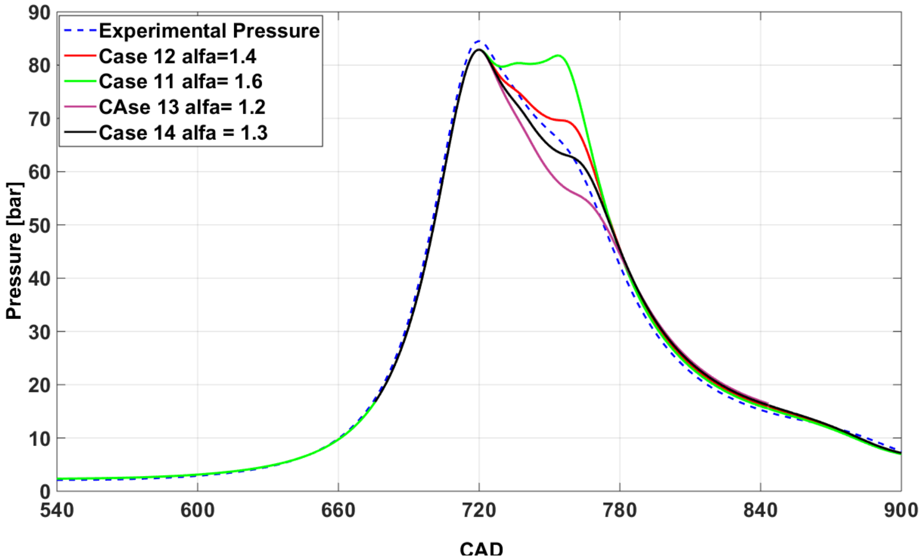

Fig. 3.21 Pressure sensitivity for ECFM calibration parameter: α sweep. Experimental data (Red dashed line)

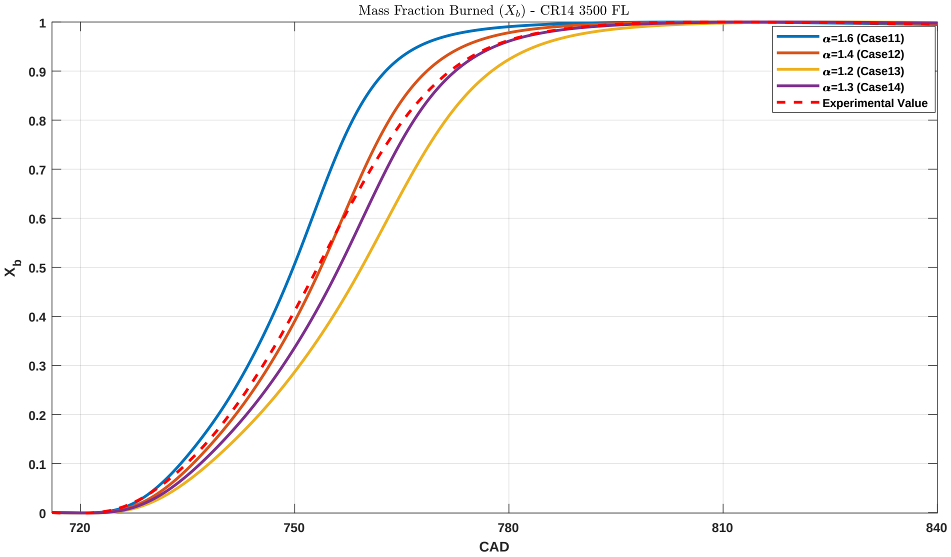

Fig. 3.22 AHRR (Apparent Heat Release Rate) sensitivity for ECFM calibration parameter: α sweep. Experimental data (Red dashed line)

The partial load cases present some additional difficulties for the model calibration. It is due to the fact that, at partial loads, model shows greater sensitivity to the small change in boundary conditions namely wall temperature, intake runner temperature etc. Also, model sensitivity strongly depends on the ignition sub-model that has a strong impact on the energy release and in turn on the pressure prediction. A test on the model sensitivity has been carried out at partial load (4 bar BMEP). The effect on the boundary perturbation has been evaluated changing the

Table 3.5 CR 13 2000x4- Simulations chronology with main set up parameters: Experimental reference values (Last Row)

No.	Alpha	RK limit [mm]	Lift Closure angle [deg]	T Cyl [K]	T Int [K]	T Exh [K]	Max P [bar]	Intake Air [kg]
1	1.3	NO	426	500	adiabatic	adiabatic	41.78	2.2054 E-4
2	1.3	NO	426	500	407	507	40.24	2.0791 E-4
3	1.3	NO	426	450	407	507	39.71	2.1096 E-4
4	1.3	NO	422	450	407	507	39.89	2.0097 E-4
5	1.3	NO	422	420	407	507	39.9	2.0269 E-4
6	1.3	1	422	420	407	507	35.57	2.0269 E-4
7	1.25	0.5	422	420	407	507	32.87	2.0269 E-4
8	1.25	1	422	420	407	507	34.45	2.0269 E-4
Experimental							34.45	2.0642 E -04

valve profile and the wall temperature of the intake duct and cylinder. The valve lift profile has been changed virtually moving 4 degrees in advance the electric command that drives the valve closure while the temperature at the wall has been varied over three different values as reported in table 3.5 . The influence of the ignition submodel is then evaluated changing the leading parameter value (i.e. “Rk limit”), Table 3.5.

In the following graphs figures (3.23 -3.24) it is reported a graphical summary of all the listed cases; the valve lift and wall temperatures obviously affects the intake mass while they have a minor consequence on the pressure peak. It is interesting to notice the influence of the cylinder temperature variation performed in cases “No. 2” and “No. 3”. The reduction of 10% of the cylinder temperature leads to an induced mass increase of about 1.5% but despite of it the maximum pressure decreased by roughly the same amount i.e. 1.5%. So in this case the effect of a mass increase is offset by the effect of a slower flame development due to the lower cylinder temperature. The major role for the model calibration is played by the ignition model, a strong decrease in the pressure peak was obtained limiting the kernel radius to 1mm. After that a further decrease to 0.5 mm was tested and finally the combination of a slight decrease for the alpha coefficient to 1.25 and the kernel limitation to 1mm was considered the best compromise for the model calibration.

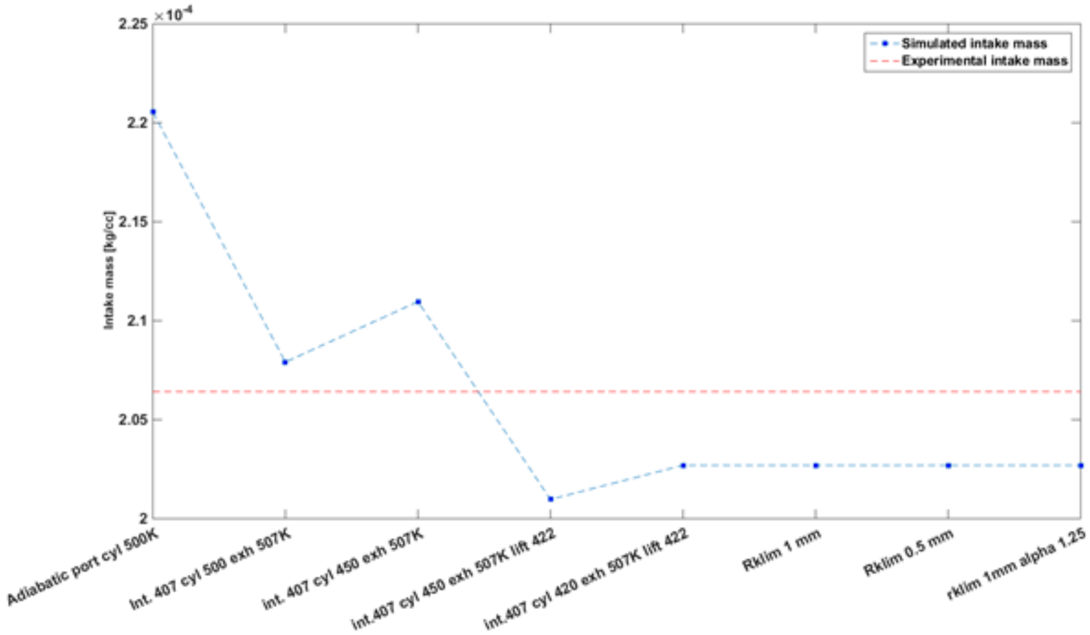

Fig. 3.23 Intake air as function of different boundary set up (Blue line) - Experimental Intake mass (Red line)

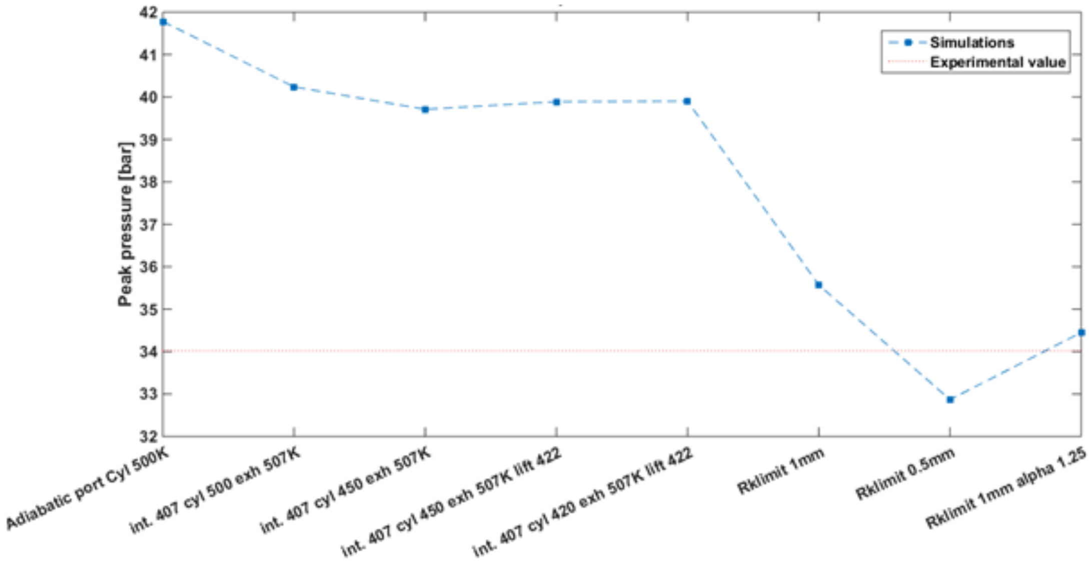

Fig. 3.24 Maximum peak pressure for different set up (blue line) - Experimental value (red line)

As a result of the calibration procedure a good agreement between the experimental and numerical data has been found.

3.4 Study on the compression ratio optimization

The better knock resistance of Natural Gas gives the possibility to increase the compression ratio with respect to gasoline engine. The increase of compression ratio is beneficial for the limit efficiency of the cycle but could bring to too high mechanical stresses than can in turn damage the engine and/or decrease the overall mechanical efficiency.
The engine evaluated in this work is derived from a normal production engine fuelled with gasoline, the compression ratio in the baseline engine is fixed to 10 to avoid knock problems in order to guarantee a reliable use. Keeping constant the structural limits of the engine,different compression ratio have been evaluated for the specific work with natural gas only. The change in compression ratio has been achieved by modifying the piston shape maintaining the same engine displacement (figure 3.25).

Fig. 3.25 Piston head design changes to achieve the higher compression ratio. From left to right decreasing compression ratio

The maximum peak pressure admissible for the engine is fixed to 100bar in order to preserve the structural integrity. In accordance to such constraint the spark advance has been changed for the different compression ratios so as limit the maximum peak.
The four variations have been tested on the test bench by Centro Ricerche Fiat as reported in the graphs (figure 3.26).

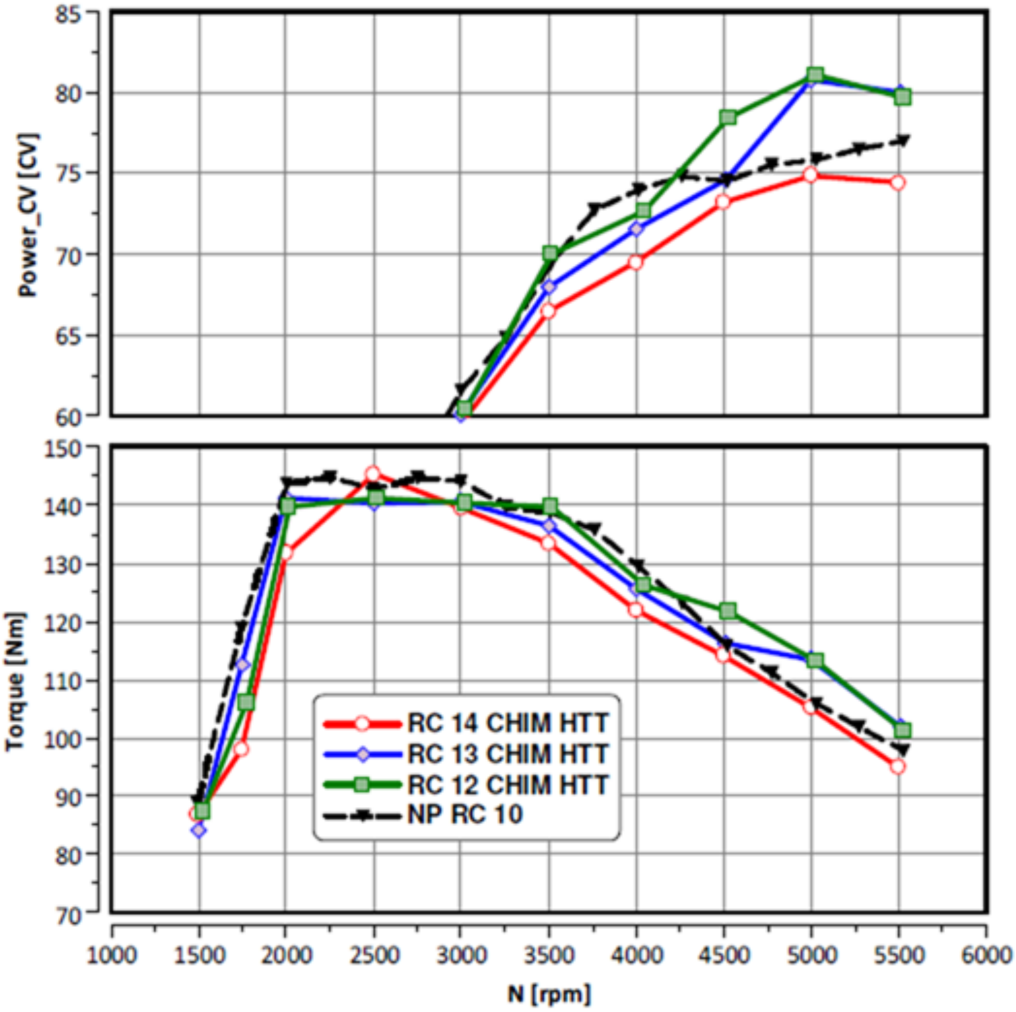

Fig. 3.26 Power and Torque as function of engine speed for different compression ratio configurations

The higher compression ratio engine gives an higher torque at 2500 rpm but it is less performing in the overall range; the power and torque thresholds were fixed at 80 Cv and 140 Nm at 2000 rpm, both of the goals are reached for the engines with CR 12 and CR 13, while are not fulfilled with the higher compression ratio, i.e. CR14.
From test bench, the IMEP CoV (Coefficient of Variation) and the variation in the peak pressure is also extracted over a representative number of cycles. In Figure 3.27 pressure traces are reported for a full load case with the three different compression ratios. The red thick line represents the ensemble average on the cycle and the light grey curves are the different pressures recorded at each cycle.

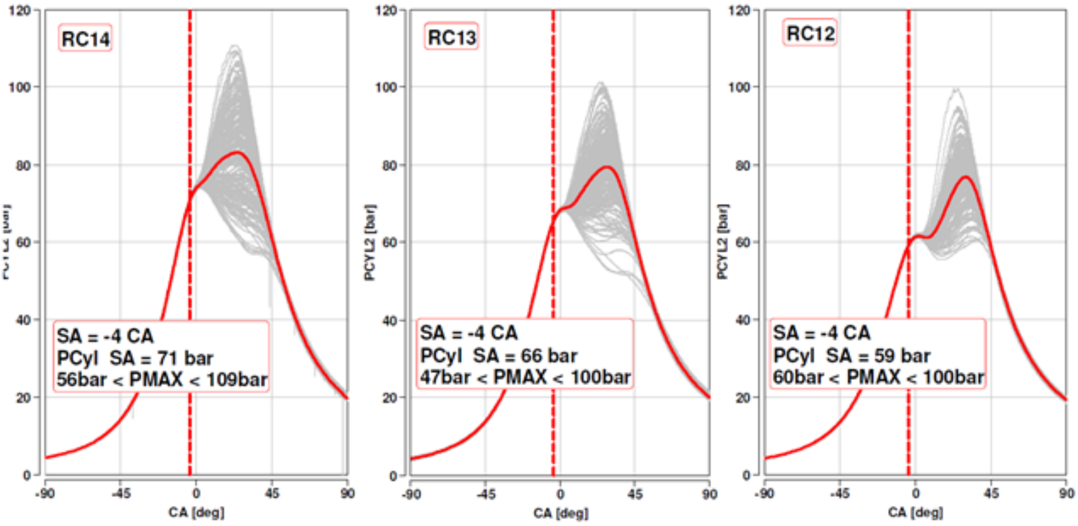

Fig. 3.27 Experimental pressure traces with different engine compression ratios. Redline shows the ensemble average of all the cycles (Greylines)

The engine with compression ratio 14 shows a higher variability and moreover the maximum pressure peak overshoots above the fixed limit of 100 bar, this behavior is clearly visible in the COV plot reported in figure 3.28.

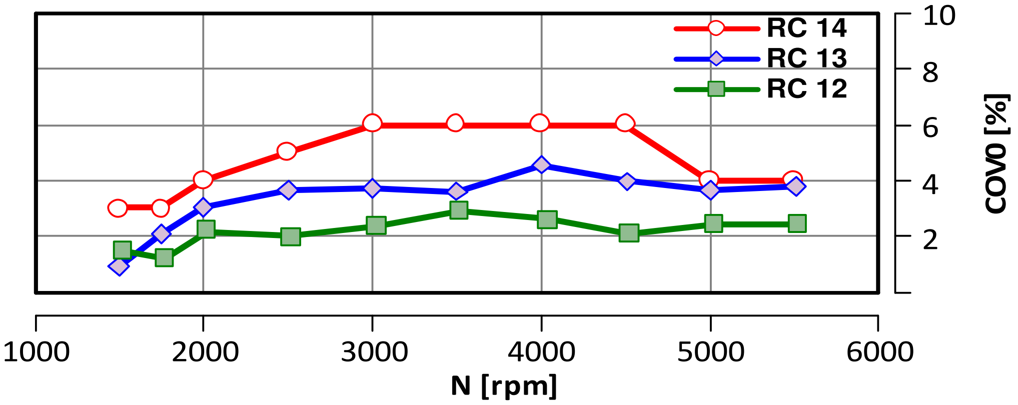

Fig. 3.28 Coefficient of variation (CoV) as function of engine speed for different compression ratios

A deeper understanding of the leading phenomena can be obtained through the CFD simulation. The three engine versions have been modelled in Es-Ice, the simulations have been performed at 3500 RPM where the three engines presents the largest difference in performances and a higher CoV is found for the CR14 case.

Figure 3.29 presents the tumble formation and evolution for the three configuration, in a section plane including the valve axis or corresponding to the cylinder symmetry plane.

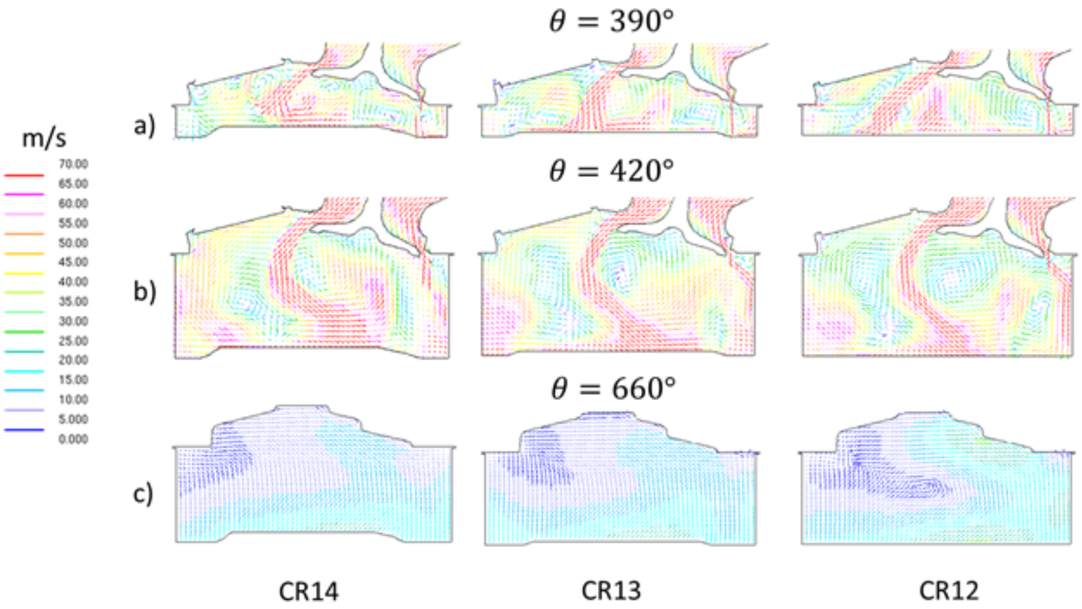

Fig. 3.29 In-cylinder Velocity field during intake phase for different compression ratios (decreasing from right to left).Rows a) and b): section cut at the intake valve axis; Row c): section cut in the cylinder symmetry plane

At $\theta = 390deg$ higher tendency of the flow to "bend" under the valve is noted for increased compression ratio. This phenomenon reduces the radius of the positive tumbling vortex (counter-clockwise motion) and on the other hand the flow reflection on the piston top deviates the flow on the left liner wall producing a bigger clockwise tumble that is accounted as negative in the reference frame. This phenomenon is enhanced when the piston approaches the top dead center due to the well known tumble spin up effect.

The tumble number value computed in all the cycle for the three cases is reported in figure 3.31. The plot shows clearly the higher tumble number for the CR12 engine and the faster decay that brings to a higher turbulence formation. The higher turbulence production is mainly responsible for the better combustion stability as confirmed by simulation, figure 3.32 displays the apparent heat release curve extracted from the simulated pressure trace following the method proposed by Brunt et al. [50]. The heat release rate shows that the combustion tends to become faster with decreasing compression ratio. This phenomenon is due to higher available turbulent kinetic energy (tke) at the start of spark especially evident in case of CR12, see Figure 3.30. It can be observed that tke is decreasing as the compression ratio is increasing.

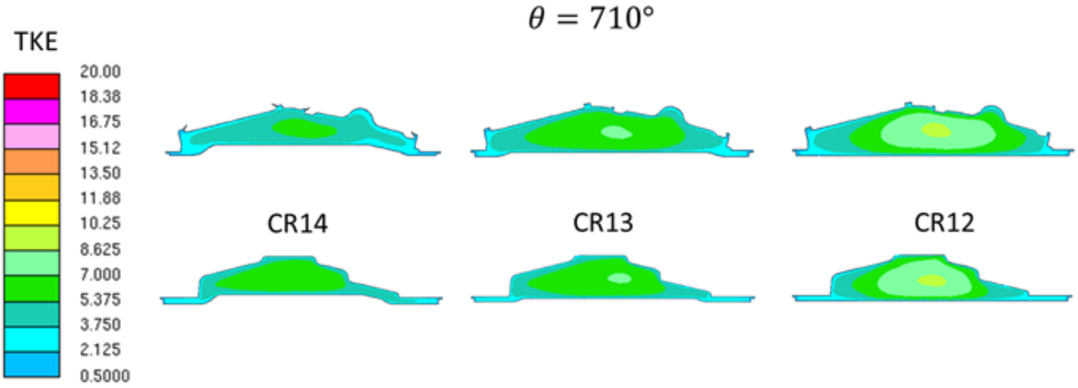

Fig. 3.30 Turbulent kinetic energy (TKE) just before the spark for different compression ratios.Upper row: section cut at intake valve axis , Lower row: section cut in the cylinder symmetry plane

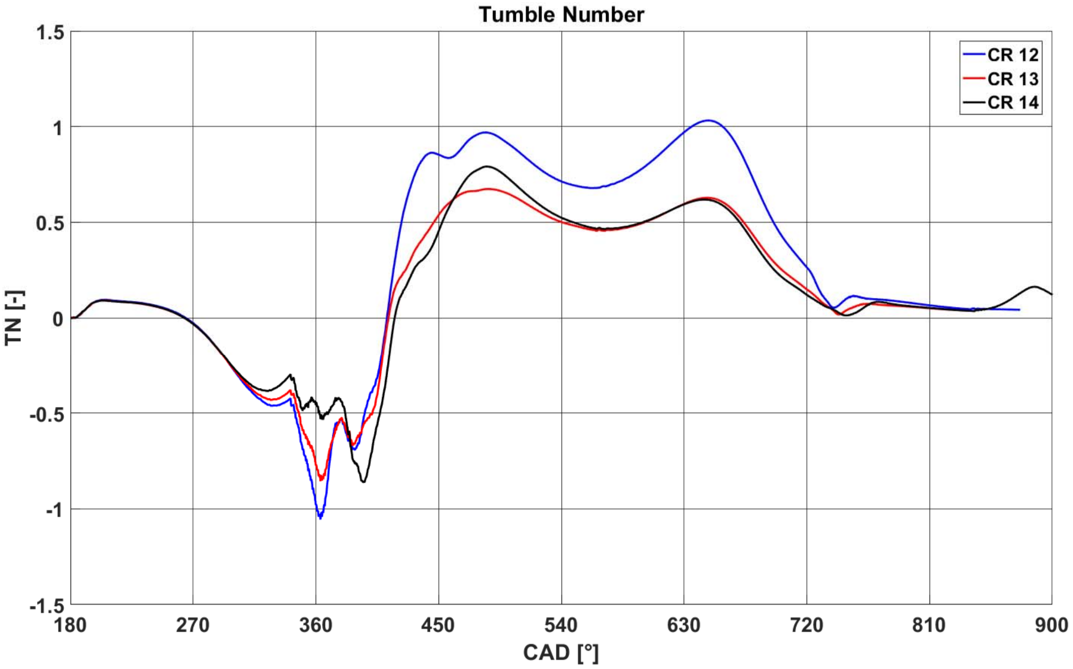

Fig. 3.31 Tumble number (TN) evolution at different compression ratios

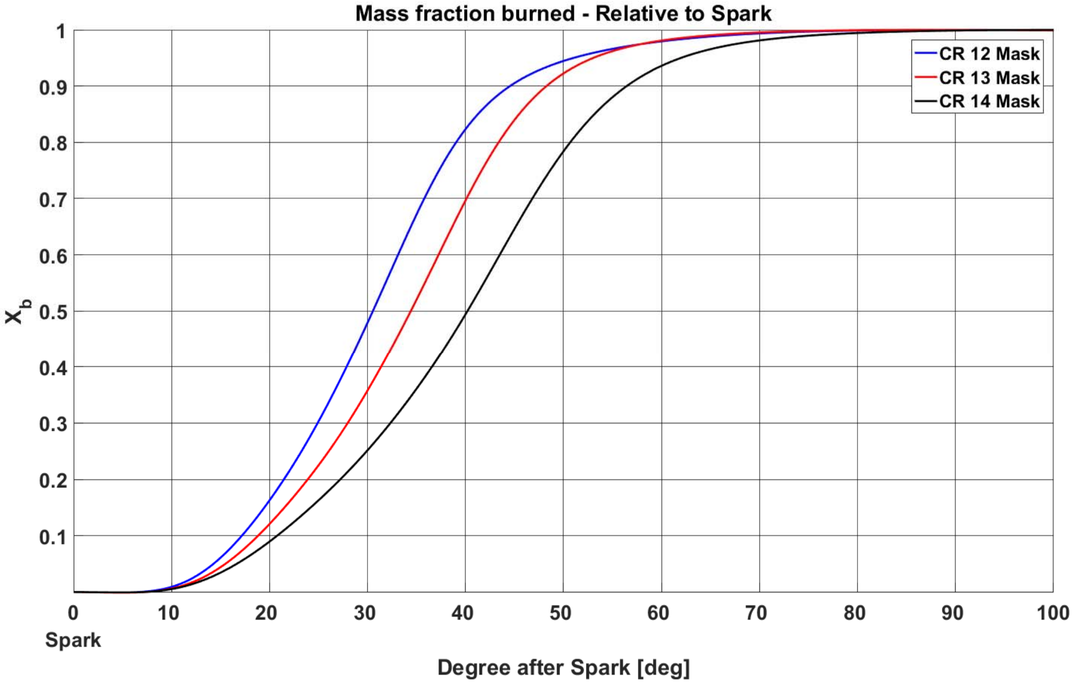

Fig. 3.32 AHRR (X_b) at full load for different compression ratios

3.4.1 Intake masking effect on complete engine model

The effect of intake masking has been further evaluated making use of a complete transient engine model. It was aimed to confirm and better quantify the positive outcomes obtained from the experimental and virtual flow bench. The use of a complete engine model gives the possibility to evaluate the real geometry of the engine during a transient condition, so that the influence of the piston geometry and its movement can be better evaluated. Moreover the combustion simulation gives the possibility to estimate the mutual influence between fluid-dynamic and chemical phenomena such as giving a better understanding about the possible improvement achievable with use of a modified cylinder head. The simulation campaign performed in this task is summarized in Table 5.12 different cases have been compared considering the engine versions with compression ratios 12 and 13 and excluding the CR14 variant on the basis of the previous experimental and numerical study. For each compression ratio the Masked and the traditional “No-Masked” cylinder head versions have been tested under three different load conditions (3500 FL, 2000X4 and 2000X 2). These loads were chosen considering the most representative and interesting points for the examined engines on the basis of the destination use and from the observed results at the test bench. The presence of mask confirms to be beneficial for the tumble formation giving rise to an higher turbulence intensity inside the chamber.

The tumble number modulation and the turbulent velocity fluctuation evaluated just before the spark discharge are presented in the histogram of (figure 3.33-3.34); it can be noticed that the

Table 3.6 Simulation campaign summary

Head Variant	Mask	No-Mask
Compression Ratio	CR12 CR13	CR12 CR13
Working Points	3500rpm at full load 2000rpm at 4bar bmep 2000rpm at 2bar bmep	

highest tumble enhancement is obtained for the medium load case (i.e. 2000 RPM 4 bar BMEP) where the tumble number for mask case is roughly doubled compared with the engine without intake masking. The improvement in tumble formation seems to be reduced in the full load and in the low load cases. This phenomenon is analysed in detail in the next lines and is mainly due to the different lift profile. Even following the general trend some specific differences can be found changing compression ratio.

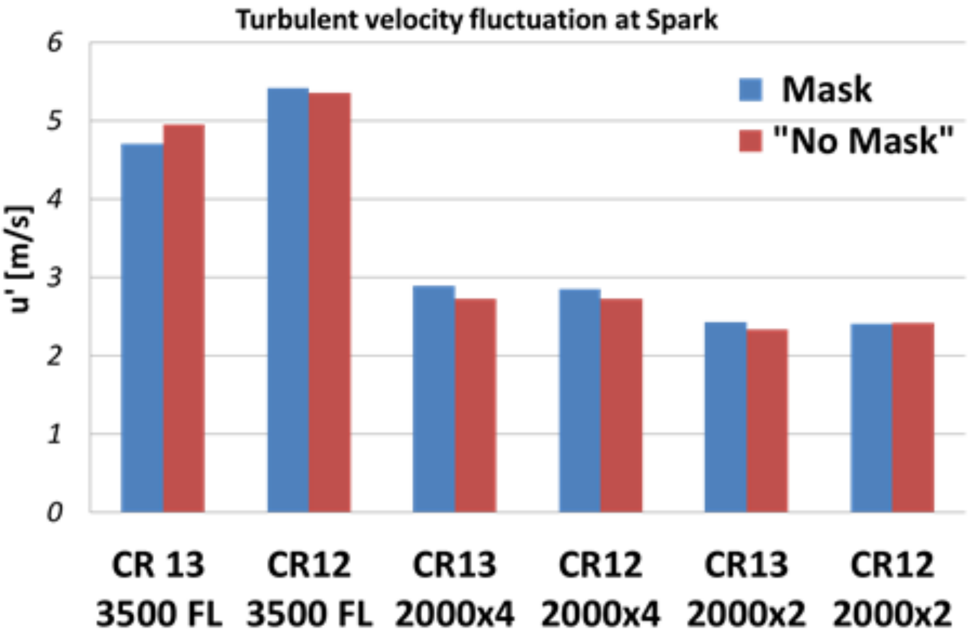

Fig. 3.33 Turbulent velocity fluctuations at spark advance for various loads : Difference in $u\prime$ for Masked and No Masked intake configurations

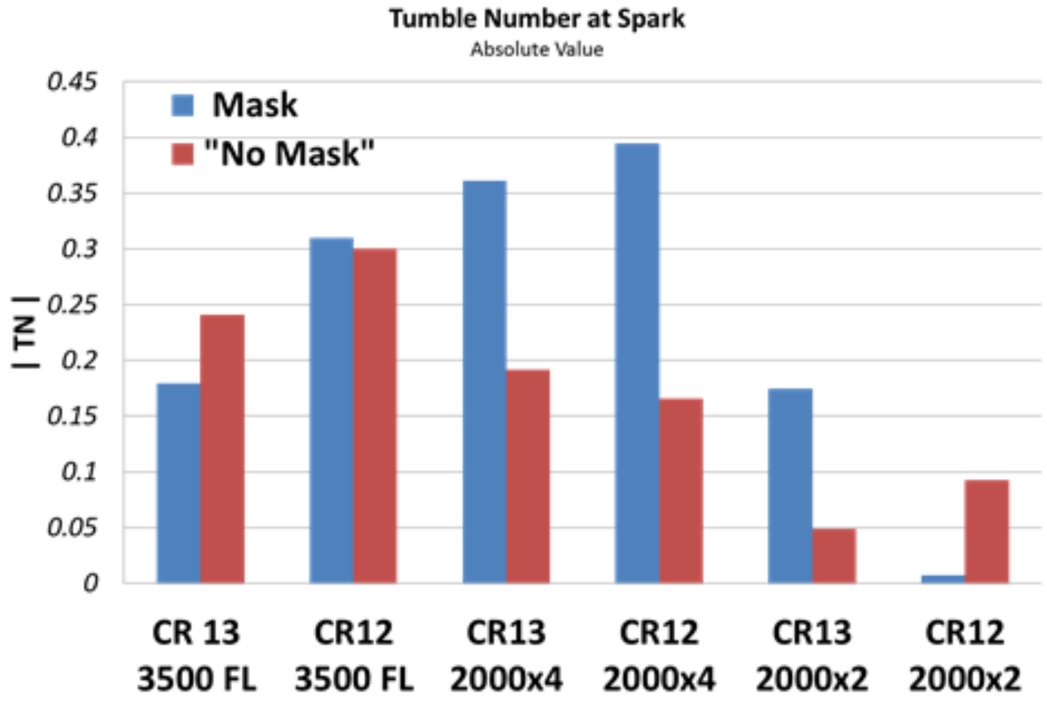

Fig. 3.34 Tumble number (Absolute value) at spark advance for various loads : Masked and No Masked intake configurations

The tumble formation mechanism for case 2000x4 CR12 is n in figure 3.37. The mask presence forces the flow on one side of the chamber leading to the formation of an asymmetry in the flow and so to a tumble formation. In the no-mask case, the flow is free to cross the valve on both the sides creating two counter-rotating vortexes that destroy each other. On the middle plane section (Figure 3.37.c) it is visible the difference in the velocity field between the two different engine geometries. In the baseline engine the high velocity vectors coming from the intake, follows the valve shape and distribute quite homogeneously in the plane. In the masked engine the flow is constrained by the mask and the flow distribution is much more uneven creating an organized motion.

The tumble evolution evaluated at each crank angle is compared in Figure 3.35 for both the engine variants. The blue solid line represents the tumble measured in the masked case and the red dashed line is the correspondent value for the baseline engine geometry. It can be noticed that the two curves diverge significantly during the second part of the intake phase, when the lift has reached its maximum and the effect of perturbation due to the previous exhaust phase is smoothed down. Nevertheless, the organized motion created during the intake phase persist during the following phases, when the piston approaches the bottom dead center and the tumble number naturally decrease due to the higher vortex ratio and to the friction dissipations that reduces the flow velocity. The final increase due to the spin-up effect given by the tumbling radius reduction is also higher in the modified engine leading to a higher turbulence level of 5% at spark time, figure 3.36.

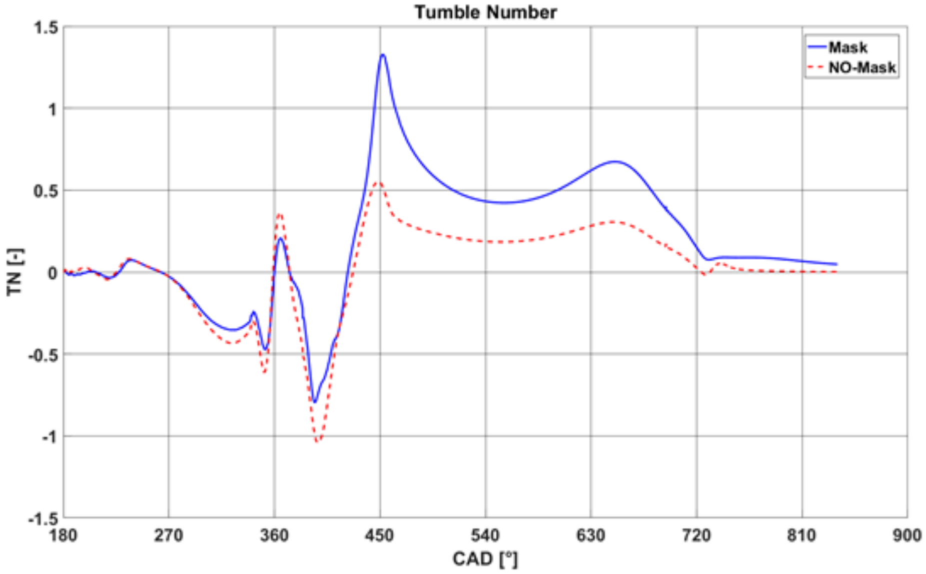

Fig. 3.35 Tumble number (TN) evolution during engine cycle: 2000 rpm 4 bar BMEP compression ratio 12

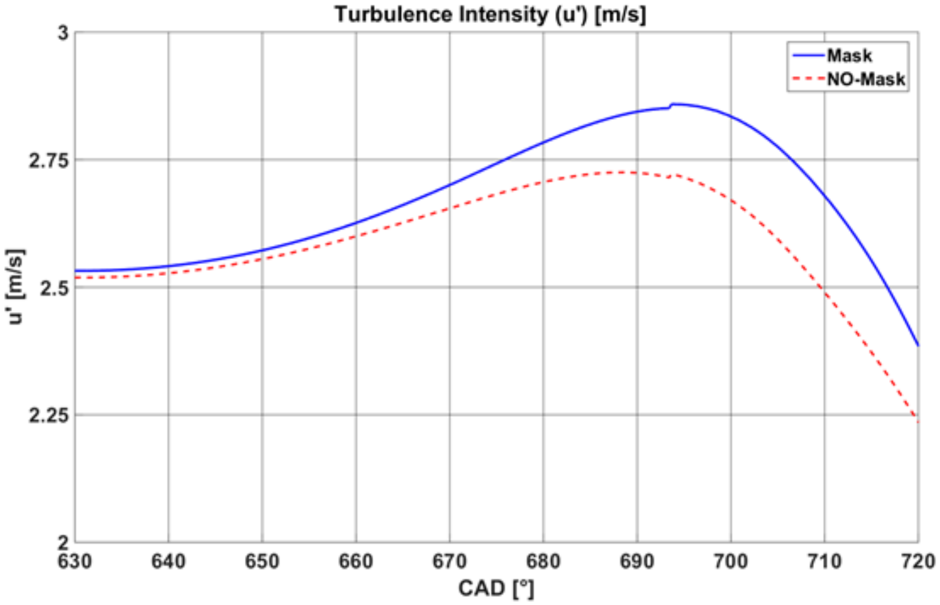

Fig. 3.36 Turbulence intensity ($u\prime$): 2000 rpm 4 bar BMEP compression ratio 12

The higher load case (3500 rpm at Full Load) is less affected by the intake masking and on the contrary the engine with compression ratio 13 seems to be even in contrast with the general trend. Figure 3.38 shows the velocity vectors for the case CR13 running at 3500 rpm Full Load.

Two cut planes respectively including the valve axis and corresponding to the cylinder symmetry plane are reported. The analysis of the flow shows a lower difference between the two engine versions with respect to what seen for the mid-load case. In partial opposition to what described in the previous case, it can be noted a better structured motion for the No-Mask engine: a small counter-clockwise eddy appears on the top of the piston on the cylinder symmetry plane, figure 3.38 b .

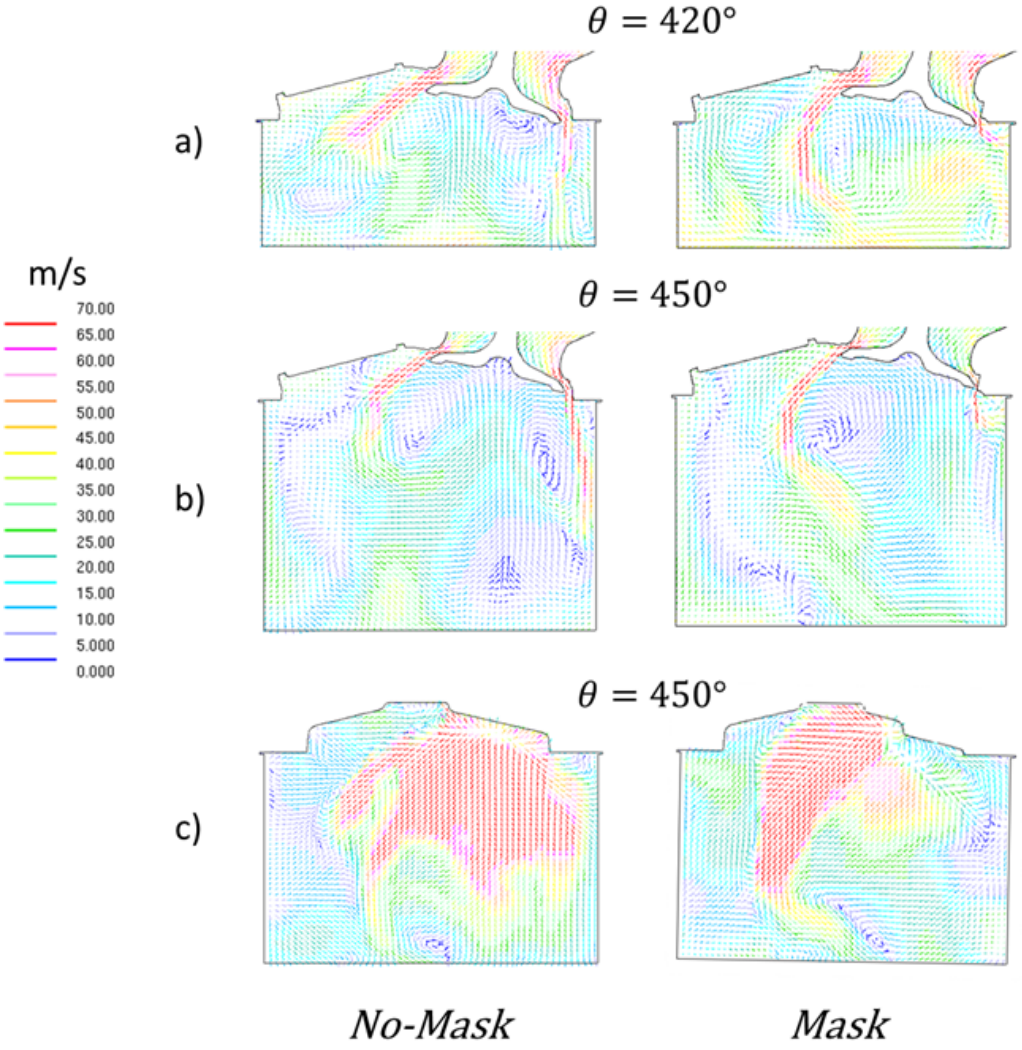

Fig. 3.37 In-Cylinder Velocity field during intake phase: 2000 rpm 4 bar BMEP compression ratio 12.Rows a) and b): section cut at the intake valve axis; Row c): section cut in the cylinder symmetry plane

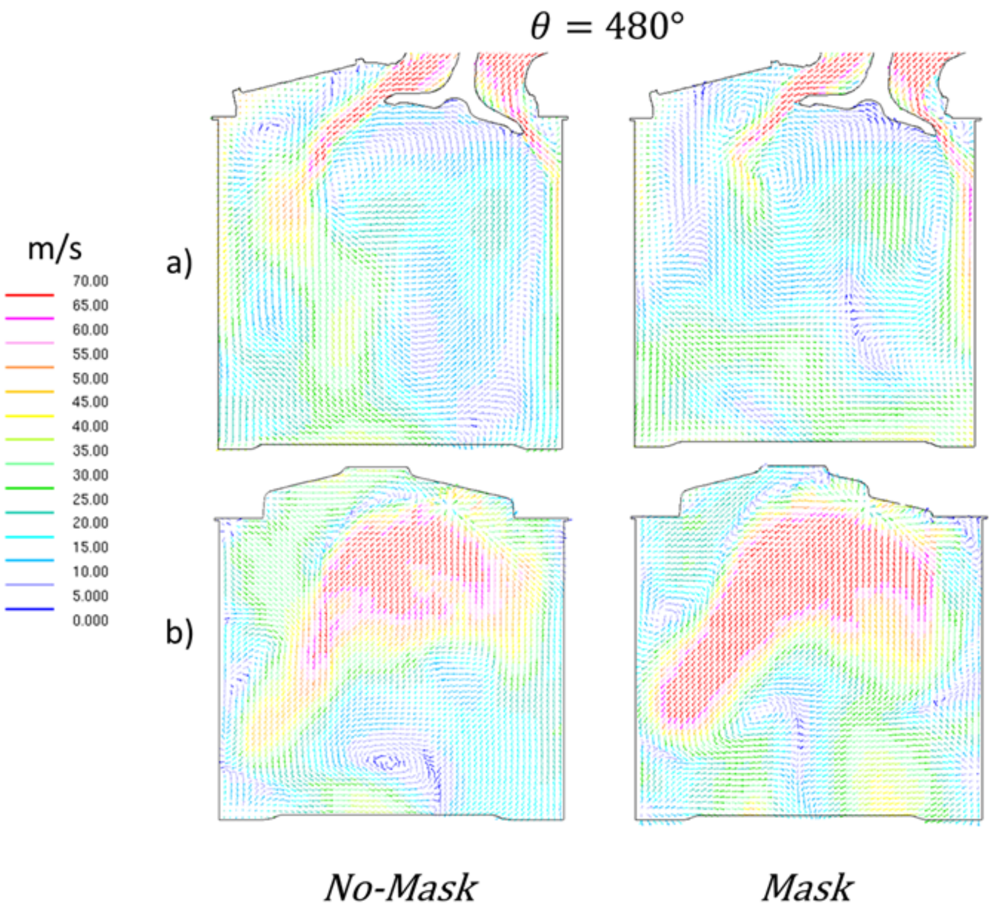

Fig. 3.38 In-Cylinder Velocity field at 480deg (Intake Phase): 3500 rpm Full load compression ratio 13:Rows a) and b): section cut at the intake valve axis; Row c): section cut in the cylinder symmetry plane

The considerations done observing the vectors are in accordance with the Tumble Number and the turbulence fluctuation velocity computed for each Crank angle. The turbulent velocity $u\prime$ for masked engine presents a higher value during the intake period while the tendency is reversed when the piston approaches the TDCf. This is confirmed by the cross cut reported in figure 3.41 that shows a significantly higher Turbulent Kinetic Energy at 450 degrees in the case of masked engine configuration.

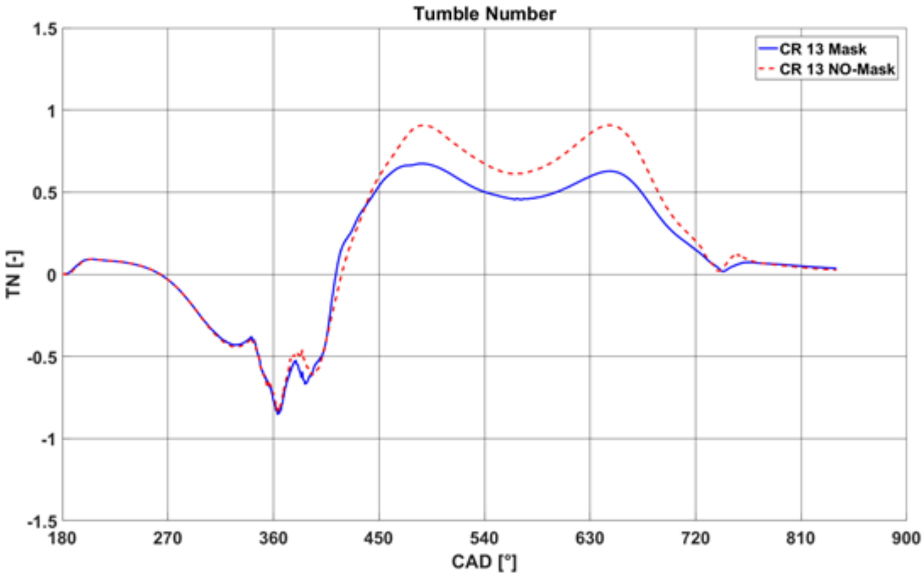

Fig. 3.39 Tumble number evolution for Mask and No-mask: 3500 rpm Full load compression ratio 13

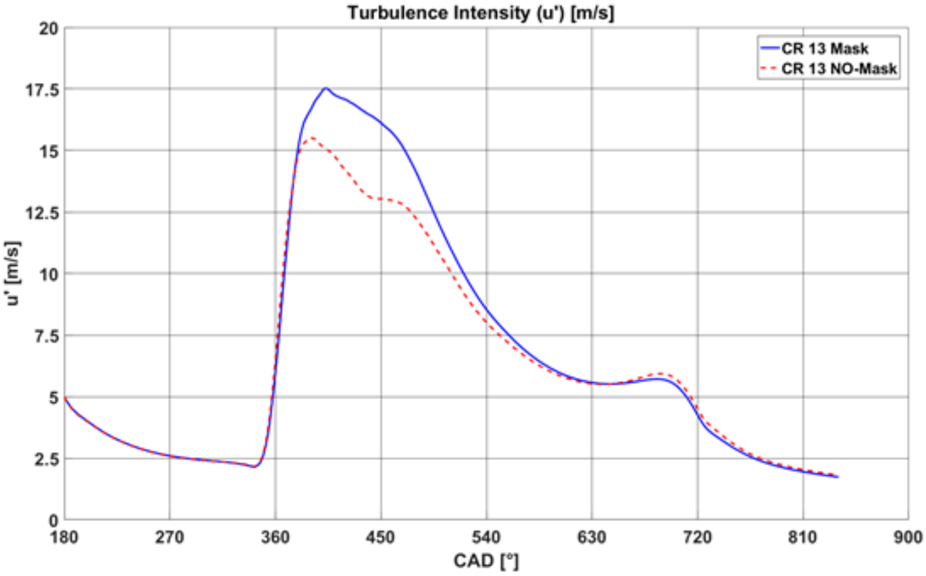

Fig. 3.40 Turbulence intensity for Mask and No-mask: 3500 rpm Full load compression ratio 13

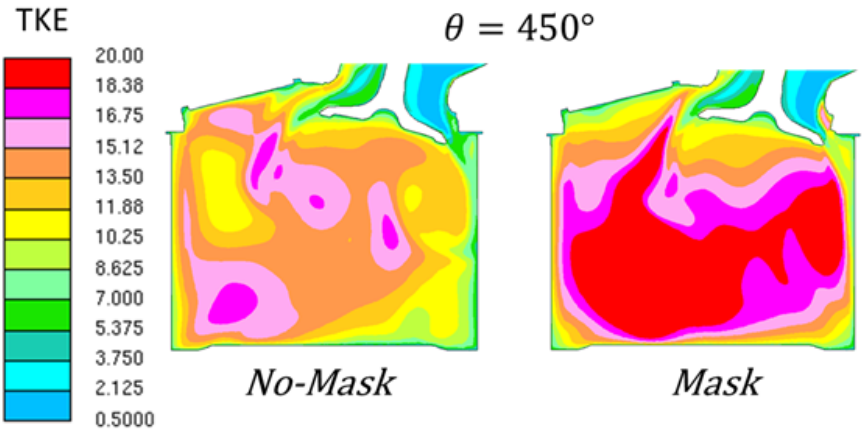

Fig. 3.41 Turbulent kinetic energy during Intake phase for Mask and No-Mask: 3500 rpm Full load compression ratio 13

The apparent contradiction highlighted in the full load cases can be explained considering the effect of valve lift on the flow. Since the engine is equipped with a VVA system, the valve actuation is different as load changes, in particular the early valve closure strategy adopted at partial load enhanced the effect of the mask because the valve in its maximum position is almost in line with the mask resulting in a strong flow obstruction and so a high asymmetry in the charge motion, on the opposite at full load the valves follow the maximum profile leaving enough space to the fluid to flow in all the port sectors and the balanced fluid exit creates counter rotating vortexes that annihilate each other without positive contribution for tumble.

For the case with CR12 running at 2 bar BMEP the lower value in the tumble number module at spark advance reported in the bar plots (figure 3.34) can be explained analysing its evolution over all the cycle (figure 3.42); the baseline engine has the tendency to create a negative tumble motion during the intake phase (clockwise rotating in the considered reference system), this motion although very weak is preserved up to the end of the cycle. The modified cylinder head instead drives the flow in a specific direction creating a positive tumble, as it is clearly visible in the spike around 420 deg; as a result the two opposite vortices interact and the tumble motion is totally destroyed.

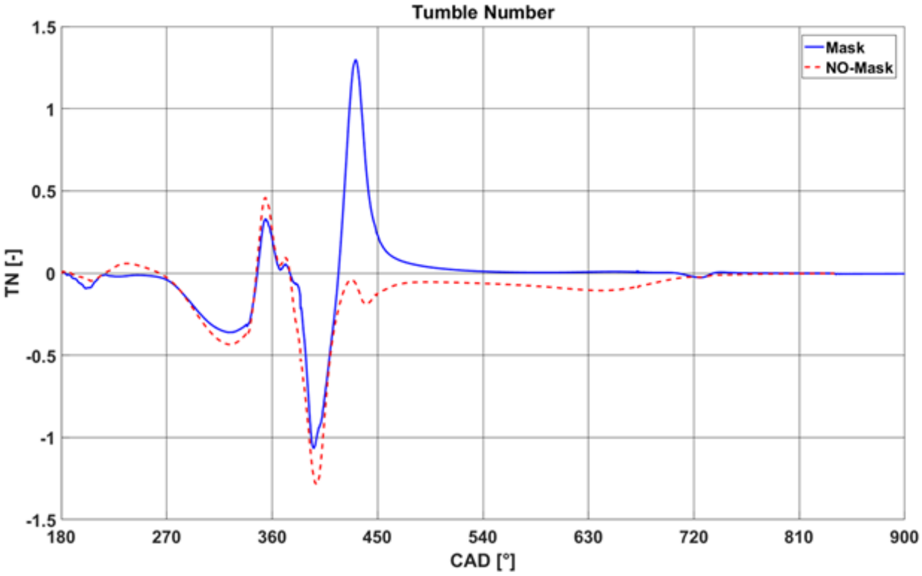

Fig. 3.42 Tumble number evolution for Mask and No-mask: 2000 rpm 2 bar BMEP compression ratio 12

3.5 Combustion simulation: Effect of turbulence on flame development

The influence of the masking on the combustion is evaluated by means of combustion simulation, the same calibration parameters used for the mask case are applied for the respective case without mask. The influence on combustion can be evaluated considering the pressure curve and the cumulative apparent heat release rate for both the engine variants, as reported in the example figure 3.43 where the above mentioned plots are reported for the full load case in the engine featuring compression ratio 12.

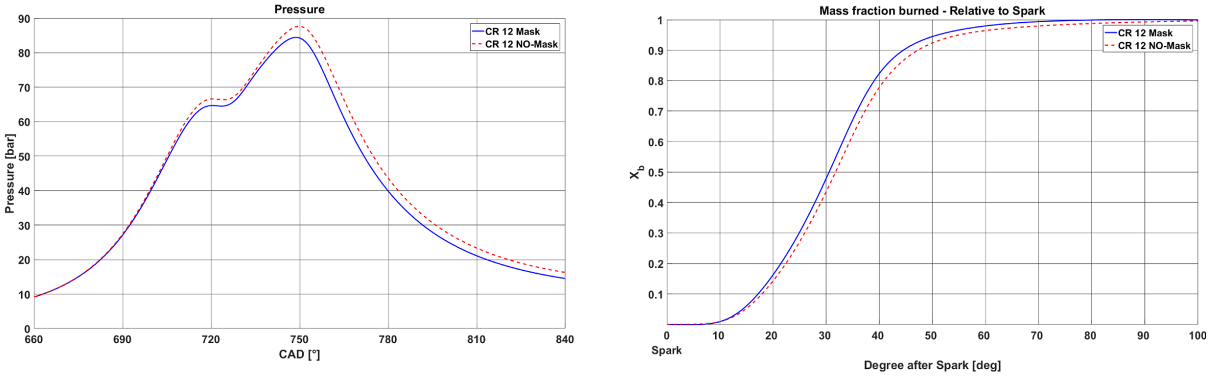

Fig. 3.43 3500rpm at Full Load: Incylinder pressure (Left) and Apparent heat release rate, X_b, (Right): Mask and No-Mask

In order to extract a meaningful synthetic index able to compare the different cases the crank angle interval needed to release the 80% of the energy is evaluated Such an interval is measured considering the rapid burning region, i.e the period that goes from 10% to 90% of the total heat released, this choice is a quite common practice in engine combustion diagnostic and it is aimed to reduce the uncertainty in the assessment of the combustion start and end.

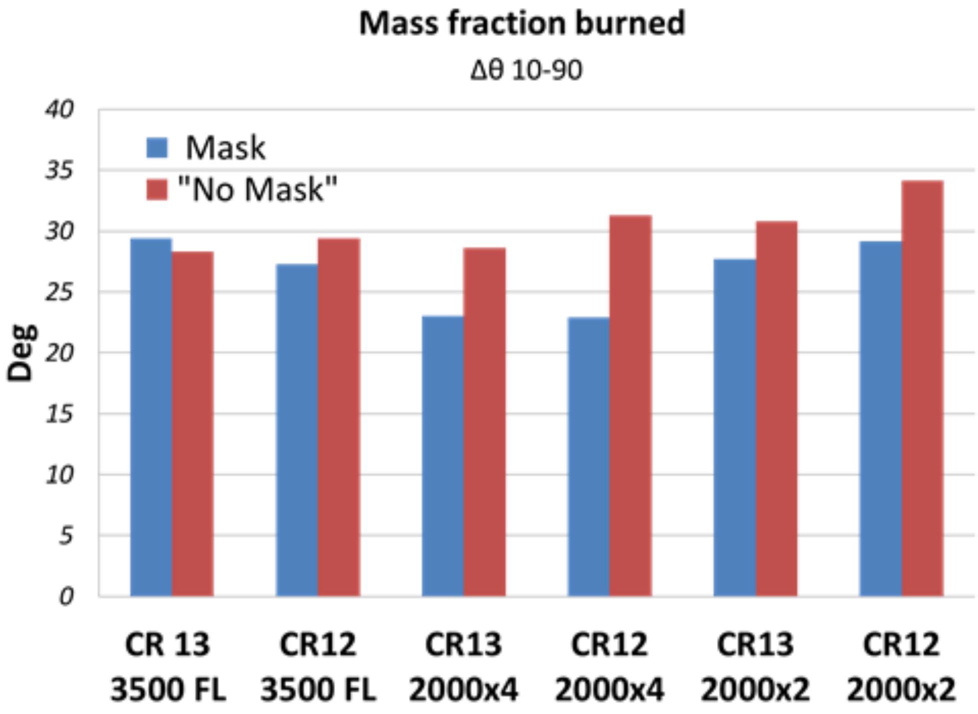

Fig. 3.44 Mass fraction burned ($\Delta\theta$ 10-90). Time taken (in crank angle degrees) to burn from 10% to 90% of mass of fuel

The values reported in the bar plot of figure 3.44 confirms that at low/medium engine loads the combustion speed is significantly enhanced by the higher turbulence level promoted by the use of the mask at the intake, while at high load the difference is not so big or even opposite (CR13 3500 FL), it is also worth to notice that the increase in combustion speed is not always related to an increase of peak pressure, as it can be seen in figure 3.43 referred to the case CR12 3500 FL; here in fact the penalizing effect of the mask on the volumetric efficiency causes a reduction in the intake mass (about 5%) and this leads to a reduction in the peak pressure that is visible both on the compression and on the combustion pressure peaks.

Chapter 4

Injector modelling

4.1 Injection

4.1.1 Introduction

This section describes the study of a Direct Injection (DI) system specifically designed for Natural Gas engines, this work is part of the “GasOn” European research project (http://www.gason.eu). The GasOn Project is aimed towards the development of advanced CNG mono-fuel engines that are able to respect the “2020+” CO2 emission targets. The target of the project is to achieve a 20% reduction in CO2 emission with respect to the current best in class CNG vehicle. This ambitious target is pursued by 3 parallel technology paths using advanced technologies able to exploit CNG characteristics in the most efficient way. The implementation and optimization of a Direct injection system specifically developed for Natural Gas engine is one of the tasks included in the WP2 branch of the ‘GasOn’ project. The task includes the use of innovative gas injector developed and provided by Delphi and the development and optimization of an ad hoc engine undertaken by Fiat Research Centre (CRF). The optical and numerical test of such engine has been performed between AVL and the Politecnico di Torino engine research group with which the author collaborates. The accurate modelling of the injector able to correctly capture the injection of natural gas (NG) into the combustion chamber is one of the fundamental objectives of this research. The injection of the fuel in the combustion chamber is a case of a supersonic underexpanded compressible flow characterised by Prandtl-Meyer expansion fan that occurs at the nozzle exit (i.e. the injector seat region) with subsequent recompression with shock formation and reflection. Thus, to accurately account for these phenomena along with a reasonable computation effort, it is important to optimize the grid topology in the supersonic region. Most of the industrial and academic research on supersonic jet exiting from poppet valve type nozzle has been performed considering a fixed lift injector and through changing the boundary pressure [57,58,59,60]. It was found in consequence that the flow initialization done by gradual increase in inlet boundary pressure and the location of the boundary are crucial to the numerical model predictability. In addition, during the transient phases, the flow speed predicted with such method results to be lower than the experimental one, due to the absence of needle movement, with negative effect on the jet penetration length [61,62]. As a result, a static flow passage is unable to account for the transient behaviour and introduces artificial treatment that implies limited accuracy especially just after the start of injection (SOI) when the needle valve opens a small aperture and the supersonic flow field starts to build up. From a numerical point of view, the simulation of the gas flow from a nozzle to the combustion chamber implies that several additional issues must be faced, mainly connected to the time-dependent problem geometry, which requires the adoption of a moving mesh strategy in which the cell number, size and connectivity may vary at the same time. Therefore, to simulate such flow accurately and improve the predictability of the injector model, a dedicated computational grid of the injector was developed individually. It was concluded in [63] that about 16 cells across the needle lift give a reasonable compromise between the accuracy of the result and the required computational time. Thus, based on the mentioned research the final injector mesh features a moving grid that allows the actual movement profile of the needle to be accommodated, with the capability of simulating a realistic behaviour of the injector during any transient phase. This separate injector mesh has then been embedded into the engine mesh (discussed later), through some numerical treatment applied on the coupling interface of these two meshes. Thus, the numerical strategy adopted has the capability to account for high accuracy required in the supersonic region as well as for the reduction in the computational time.

4.1.2 Computational Grid Development

The computational grid for the injector consists of one continuous block of cells divided into two parts. The first part encompasses the fluid volume from the injector tip up to a certain upstream portion of the injector internal passage around the needle (see figure 4.1). The length of this upstream portion is long enough so that the fluid there can be meaningfully regarded as having uniform properties or, in other words, as one-dimensional flow over that cross section, but possibly short enough so that the original geometry of the injector internal passage is respected and computational cost contained. The uniform cross section facilitates the specification of boundary conditions for the injector inlet connected with the further upstream passages and fuel supply line. The function of this first part is to precisely model the injector geometry and especially the needle movement. The second functional part belongs to the fluid volume inside the engine cylinder just downstream of the injector tip and is independent of the injector geometry (see figure4.2). The reason for the injector mesh being extended downstream into the cylinder volume is to avoid abrupt change between the mesh at the interface and allow a smooth transition resulting in modelling of the flow dynamics with reasonable accuracy. It is important to reiterate that the injector in the region at the interface is characterized by high Mach number and strong shock formation, as a result the numerical technique used to connect the injector grid to the engine grid may not be able to handle such challenging flow accurately. Therefore, it is preferable to postpone as much as possible the flow passing across the interface. Another concern is that the flow field immediately downstream of the injector exit is predominated by the axially-symmetric jet that is faintly influenced by the much slower in-cylinder air flow. So, the second functional part can prevent the jet from becoming asymmetric solely due to discretization error owing to the non-axially symmetric engine grid.

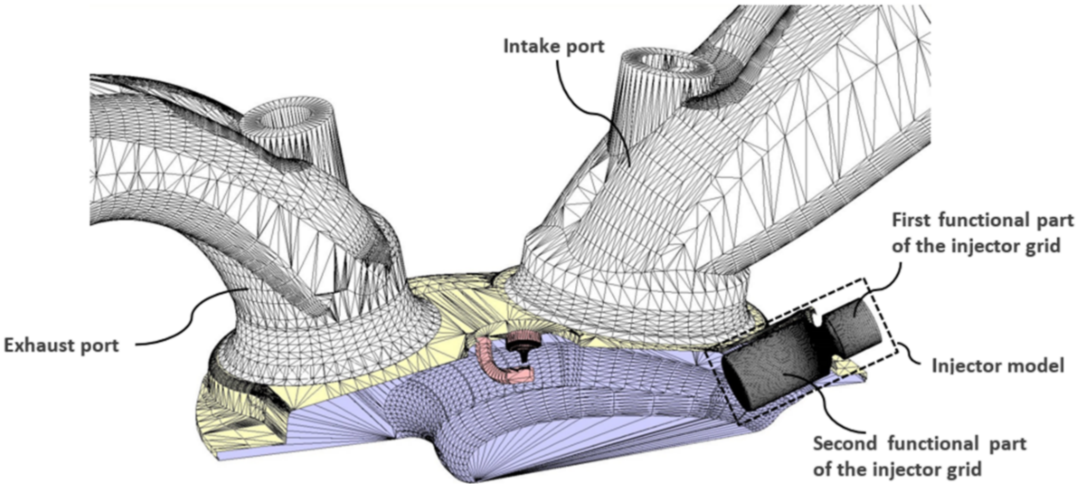

Fig. 4.1 Geometry of the Engine showing the positioning of the injector

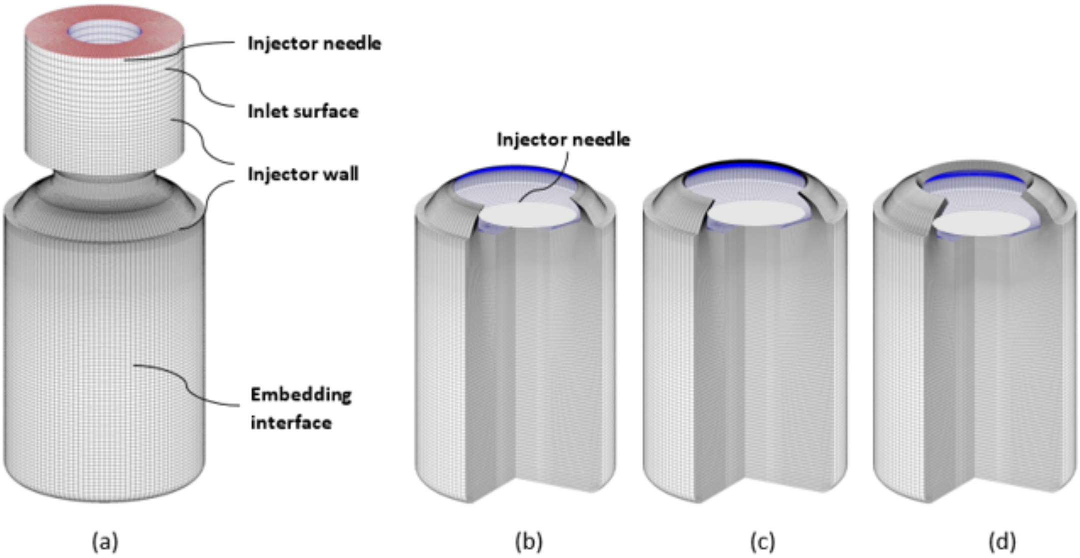

Fig. 4.2 Computational grid of the injector (a) Complete grid (b) Needle at closed position (c) Needle at 25% of the maximum lift (d) Needle at maximum lift

According to the different functions mentioned above, the injector mesh that represents the fluid volume has surfaces with different boundary conditions. The inlet surface corresponds to the inlet cross section i.e. the beginning of the first functional part, which is perpendicular to the flow and can be considered one-dimensional. Therefore, this surface is treated as a uniform pressure boundary. The injector wall represents the inner wall of the injector nozzle housing, in contact with the fluid, which is modelled as an actual wall boundary. And the embedding interface circumscribes the second functional part that is to be connected to the engine mesh numerically. The numerical treatment ensures a continuum without barrier and thus guarantees communication of flow solution as if the injector and engine grids were an existent wall. The last surface is the outer surface of injector needle, which benefits from the new feature in this injector model. The needle surface is a wall boundary that is movable according to a given lift profile, thus resulting in a moving grid of the injector. Given a realistic needle lift curve is provided, this moving grid allows the real transient behaviour of the injector to be considered, therefore capable of accurately simulating the flow fields during the entire injection duration within an engine cycle. In addition, this model can also be used to study the response of injection spray to various needle actuation profiles. To realize the movable needle, it was the essential that an injector model be built independently from the rest of the engine domain. This is because commercial 3D CFD codes suitable for engine cycle simulations allow for the motion of valves and piston but usually not of the injector needle. This new feature of this model has the advantage that the movable needle can reproduce the real variation of the nozzle flow passage which in turn provides insight into the transient flow fields. Given the compressibility of the gaseous fluid, this feature has the potential to better capture the gaseous flow than using fixed nozzle does, especially during the spray build-up phase shortly after the SOI.

4.1.3 Engine models

The engine prototypes under study, supplied by CRF, are two turbocharged NG DISI engine with a side-mounted housing for the NG injector (table 1). The two engines differs mainly for the injection angle positioning, the second engine prototype (Engine 2) presents a much steeper angle between the nozzle axis and the plane normal to the cylinder, thus the predicted cone jet is supposed to not interact with the injector niche cavity (Figure 4.3 d)). Furthermore the head and port design is significantly different (figure 4.3 b - f) for the two engines, the adoption of inclined ports and the head masking adopted in the second prototype gives rise to an higher tumbling tendency with important consequences on the mixing mechanism and turbulence performance.

Table 4.1 Engine Configuration

	Engine 1	**Engine 2**
Bore	72 mm	70 mm
Stroke	84 mm	86.509 mm
Compression ratio	13	13
Number of Cylinders	4	3
Displacement	1367 cm^3	998.777 cm^3
Valves per cylinder	4	4
Turbocharger	WG-controlled FGT	WG-controlled FGT
Intercooler type	Water-to-air	Water-to-air
Injection	DI	DI
Injection Angle	70 degree	35 degree

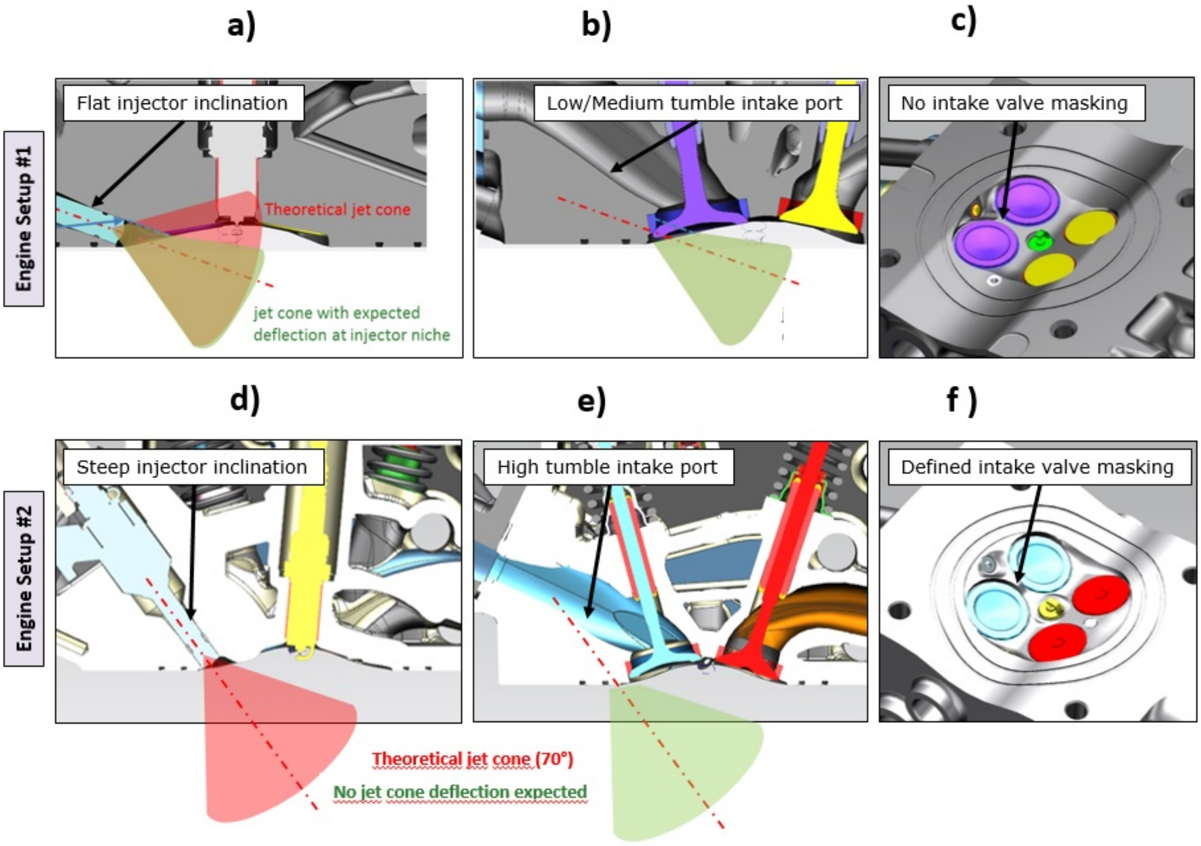

Fig. 4.3 Top Row: Engine Type 1; Bottom Row: Engine Type 2

The computational domain of the engines encompassed one engine cylinder together with intake and exhaust ports and runner. Given the fact that the fluid volume of all those parts is symmetric about the vertical plane passing through the injector and spark plug, only half of the engine geometry is considered to build the computational grids to reduce simulation time and cost. The engine model has an inlet pressure boundary at the far end of the intake runner and an outlet pressure boundary at the far end of the exhaust runner. These pressure boundaries replace the real intake and exhaust system including manifolds and connecting ducts to other cylinders but still provide the real flow conditions as in the real multi-cylinder engine. All the other surfaces are wall boundaries and, in particular, the intake and exhaust valves as well as the piston are movable walls. Therefore, the engine model is suitable for transient simulations of full engine cycles. In addition, the second functional part of the injector model belongs to the engine volume. So, the engine model in turn has a part carved out in correspondence to the injector model, and the reserved cavity on the engine grid is confined by a surface that is the same as the embedding interface on the injector grid. When the injector model is incorporated into the engine model, the full model can be used for the study of injection with the advantage of having a movable injector needle.

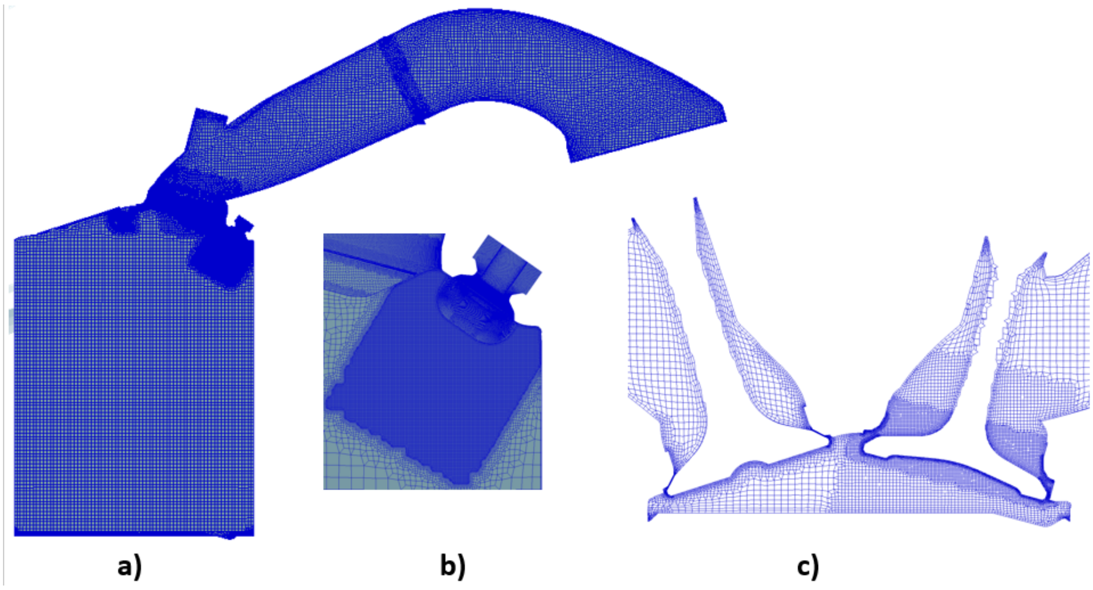

Fig. 4.4 Computational domain of the engine with subsequent refinements (a) Engine (b) Injector (c)Plane through the valves

The injector model and the engine model were combined to generate the final complete engine model that was featured by movable valves, piston, and injector needle.The numerical grid adopted for such study has been accurately refined taking in consideration the flow phenomena and trying to keep the numerical effort to the minimum. Some overview of the engine numerical grid is shown in figure 4.4, it is worth to notice the mesh refinements adopted at the connection boundary between nozzle and the cylinder volume.

4.1.4 Preliminary grid assessment on Moving mesh injector

Figure 4.5 (a) through (c) shows the simulation results of CH4 concentration obtained from the five cases at three time instants when the injector needle is 25%, 50%, and fully opened, respectively. Figure 4.5(d) shows the Mach number profile of the injection spray when the needle is at the maximum lift. Since the flow fields were axial-symmetric, results on only one half of the symmetry plane in are shown. It can be observed in Figure 4.5 that the results of Case III and IV are very different from those of Case I, II, and V, as a result of different convection calculation i.e. in Case III the convergence requirement on momentum was removed and in Case IV the two-stage pressure correction was introduced, such numerical treatment resulted in even worse flow solutions than those given by the 1.5th-order scheme at least at later stage of the injection as evidenced by Fig. 4.5 (b) and (c). At early stage of the injector when the spray started to mix with air, the spray penetration predicted by the 1.5th-order scheme was higher than that by 2nd-order scheme. This behaviour was likely attributable to the higher numerical diffusion error intrinsic in lower-order schemes that, in the case of air-fuel mixing, appeared as an enhancement of the mixing process. Such discrepancy between 2nd-order and 1.5th-order schemes became less evident as the injector opened and bulk of fuel was injected. In terms of the more demanding prediction of shock structure shown in Figure 4.5 (d), the difference was mainly between 2nd-order and 1.5th-order schemes. The shock structure predicted by the 1.5th-order scheme was less clear, which was again due to the higher numerical diffusion tending to smooth the abrupt change of flow properties associated with shock waves. Based on these observations, one can conclude that, as an ideal strategy for simulating the gaseous injection, the 2nd-order numerical schemes should be used both for continuity and momentum equations with proper convergence criteria, especially at early stage of injection, as long as the convergence of residuals is attainable. In time periods when intermittent convergence issues occur, the 1.5th-order scheme can be considered to mitigate them. Figure 4.5 (a) through (c) also reveals the feature of the injector design. It can be seen that, as the injector opened, the injection spray formed a narrow cone in the normal direction of the needle axis. This feature is called the collapsing jet that is intended for the application of side-mounted DI injector.

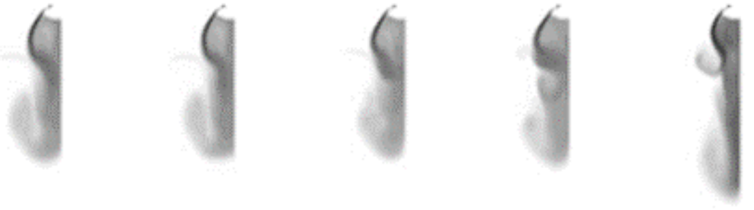

(a) Injector 25% opened

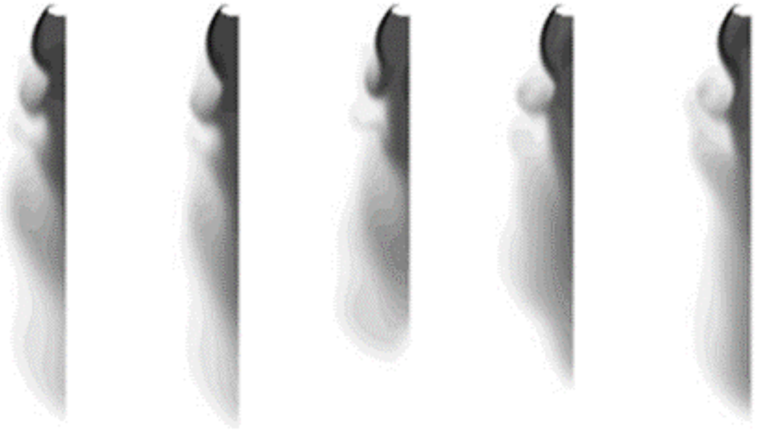

(b) Injector 50% opened

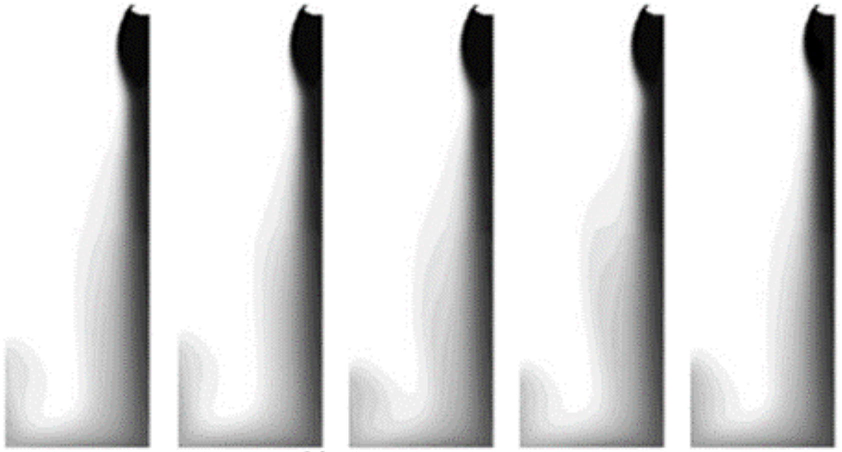

(c) Injector fully opened

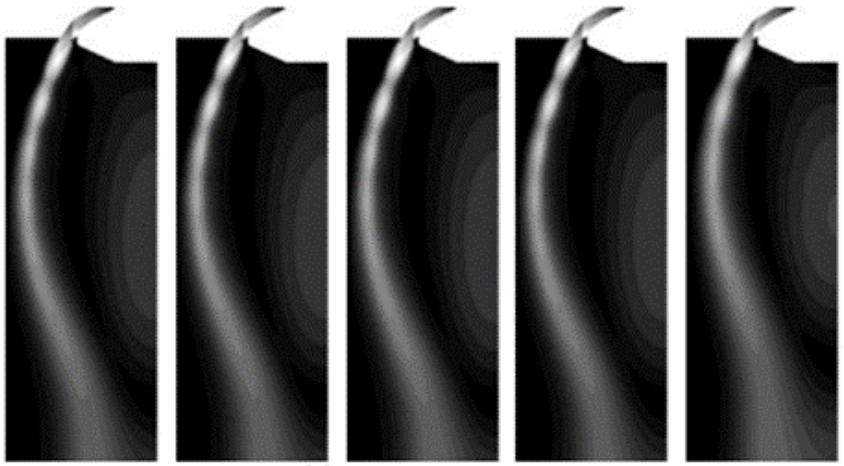

(d) Injector fully opened

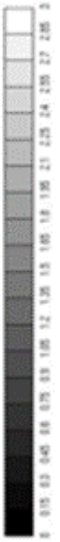

Fig. 4.5 Simulation results of injection processes (a) (b) (c) CH4 concentration contours (d) Mach number contours

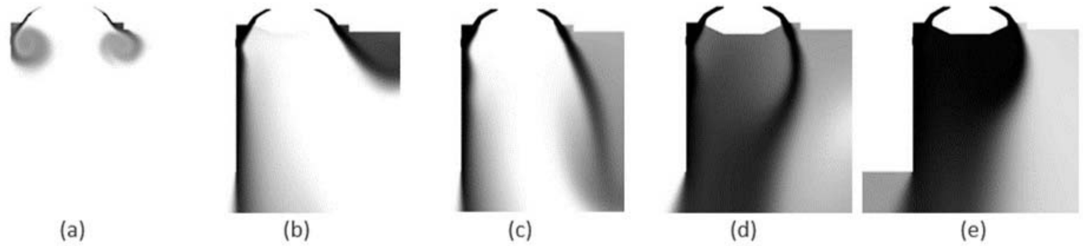

Fig. 4.6 Simulation results of injection processes with wall impingement (a) Injector just opened b) Injector 50% opened (c) Injector 75% opened (d) Injector fully opened (e) Injector fully opened and spray at steady state

The advantage of such collapsing jet is that the injected fuel can travel long enough towards the spark plug and centre of the engine cylinder without excessively mixing with air around the injector tip locally. The simulation results of injection process in presence of wall impingement are shown in Figure 4.6. Since the computational domain in this case was no longer axial-symmetric, the results on the whole symmetry plane are given. The left side of each figure corresponds to the part where pressure chamber was removed while on the right side the computational grid was the same as in the previous case. At early stage of injection (see Fig.4.6 a through c), the presence of a nearby wall restricted the spray and forced it to follow the vertical wall boundary without the formation of large-scale vortex, whereas on the right-hand side the spray was free to expand into the much larger pressure chamber and formed an inward vortex. However, as shown in Figure 4.6 d and e, when the injector was fully open and the steady spray established, the wall appeared to attract the jet on the opposite side towards it and eventually the collapsing jet was even deflected to the side of wall straying away from the central axis. The explanation is that when both the left and right jet could evolve freely without restriction of nearby wall, they tend to form two symmetric inward vortices that balanced each other. When the presence of wall destroyed the vortex of the flow on its side, the inward vortex of the jet on the other side lost the counter-balancing force and hence continued the inward revolution beyond the central axis to the side of the wall.

Based on these results, it is speculated that the injection spray in the engine may very likely be attaching the pent roof all the way to the exhaust side, rather than collapsing into a cone along the inclined central axis of the needle.

4.1.5 Simulation Campaign

Two different engine prototypes have been tested evaluating for each of them several injection strategies at different load and speed conditions. For the mixing and turbulence evolution one of the most important difference between the two engines is related to the injector positioning that have a different inclination in the two different cases. The simulation campaign has been performed on the first engine considering two full load cases,1500 rpm and 5500 rpm and a partial load case at 2000 rpm with 4 BMEP load. On the second prototype, similar preliminary cases have been tested considering a high load condition at low engine speed (i.e. 1750 rpm Full Load) and a partial load case at 2000 rpm (i.e. 2000 rpm 4 bar BMEP). The points were chosen based on the engine characteristics, considering the most interesting point for the optimization and the availability of the optical test for a qualitative model validation.

4.1.6 Results and Discussion

4.1.6.1 Engine 1: Case – 1500 RPM at Full Load

Firstly, the 1500 rpm full load point was considered. In this case a very late injection strategy has been tested in order to maximize the low-end target torque by means of an optimization of the volumetric efficiency avoiding the displacement of fresh air during the intake phase (figure 4.7). The Injection event starts around the bottom dead centre and ends 110o before the top dead centre firing. The short time left between the end of injection and the firing point make the situation very problematic for the achievement of a good mixture quality and homogenization. In Figure 4.8 are shown the air to fuel isolines that are useful to understand the fuel path evolution inside the chamber. The flow tends to mix with the air following the clockwise tumble motion that is created during the intake phase (Figure 4.9), the Coandă effect cause the adhesion of the outgoing flow to the cylinder head. As the flow impact on the opposite side of the liner, the rich cloud on one hand is reflected tangentially in a swirl-like motion as shown in (Figures 4.8 d-e-f), and on the other hand it is deflected downward following the tumble flow pattern. It can be seen (Figure 4.10) in the concentration contours the combination of these motions brings a higher fuel concentration on the left piston side in proximity to the injector nozzle. The presence of a late injection is found to be beneficial for the enforcement of the tumble motion (Figure 4.11) and for the increase of turbulent kinetic energy in the chamber (Figure 4.12).

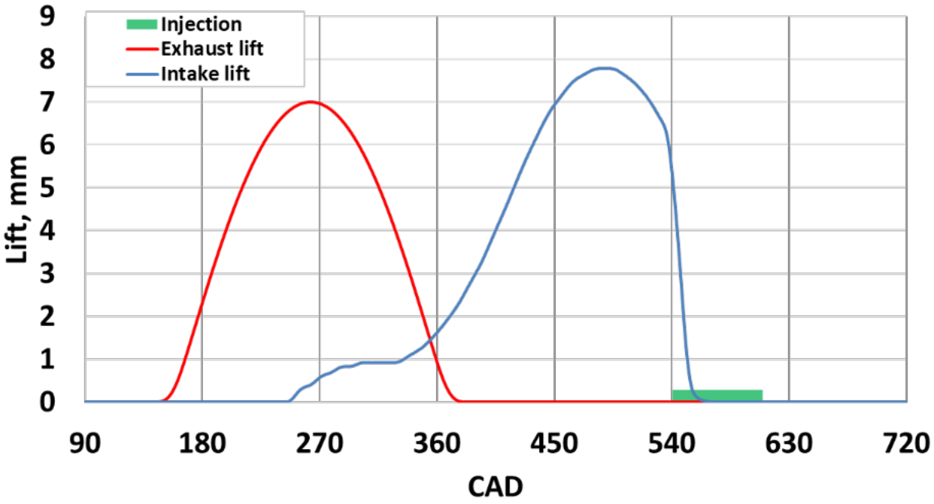

Fig. 4.7 Valve Lift Profile with Injection window (green) (1500 RPM at Full Load)

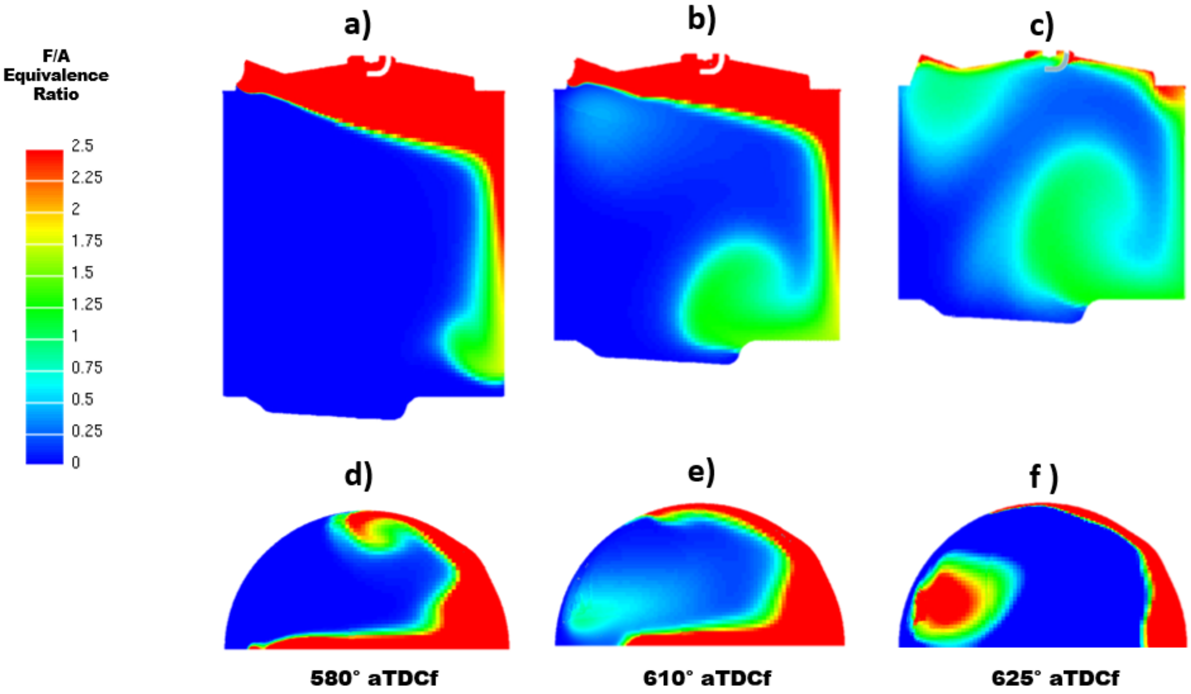

Fig. 4.8 Equivalence Ratio Contours; Top Row – Plane of Symmetry, Bottom Row – Plane passing through the injector in Z plane (1500 RPM at Full Load)

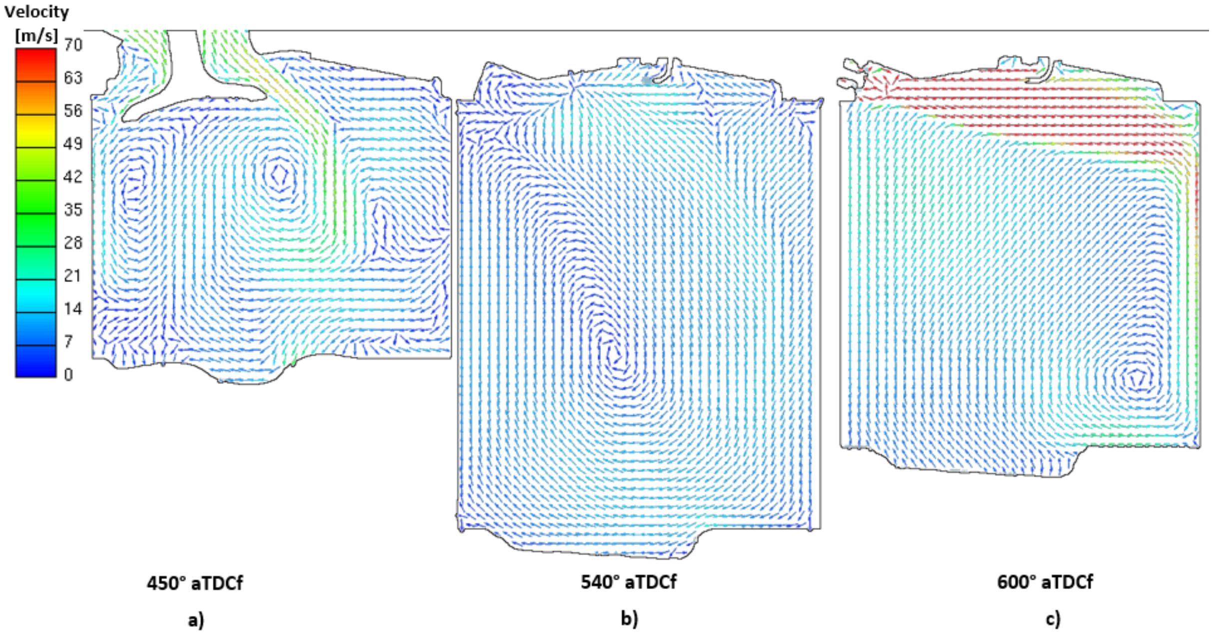

Fig. 4.9 Velocity Contours (1500 RPM at Full Load)

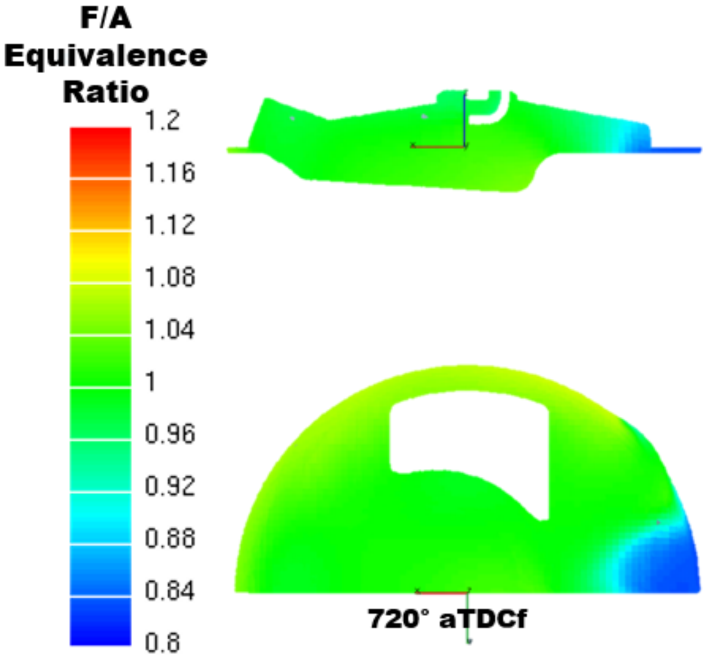

Fig. 4.10 Equivalence Ration Contours at Top Dead Centre – Crank Angle 720 degrees

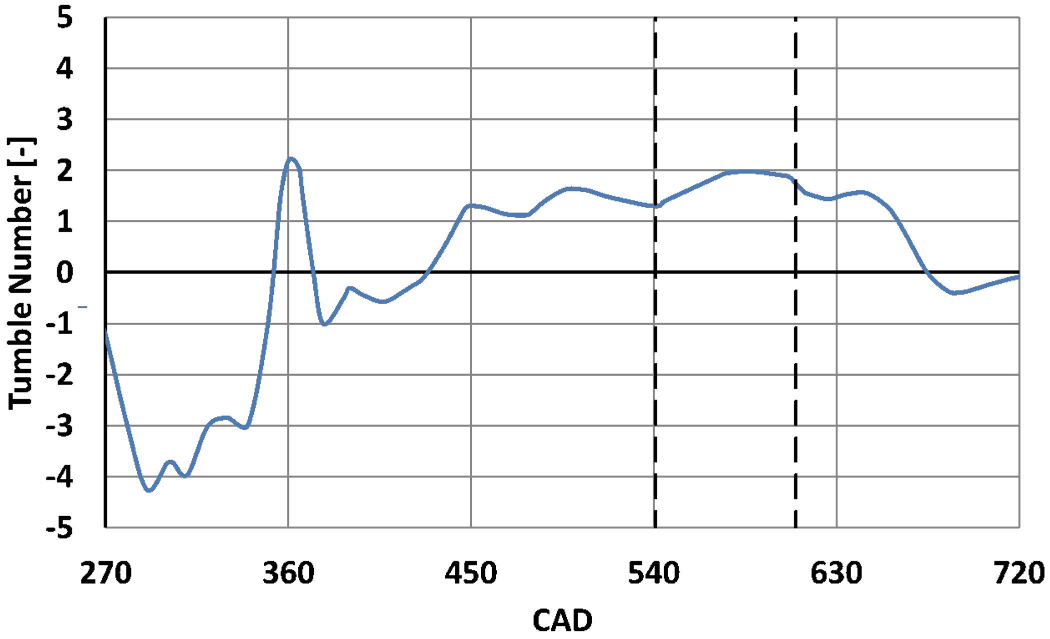

Fig. 4.11 Tumble Number (1500 RPM at Full Load)

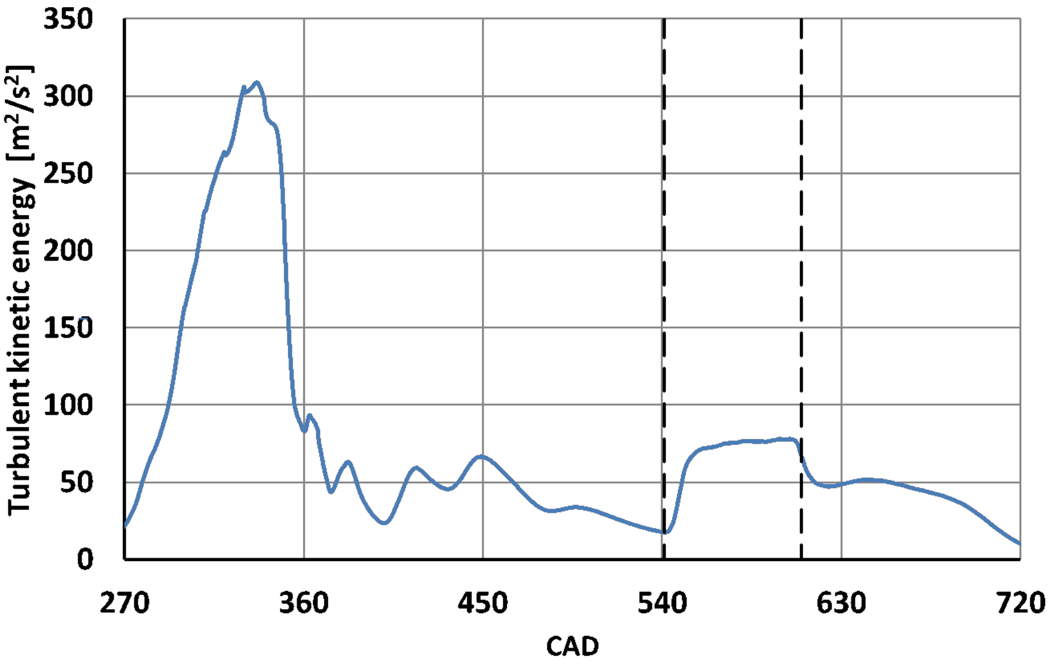

Fig. 4.12 Turbulent Kinetic Energy (1500 RPM at Full Load)

A more precise assessment for the mixture quality has been obtained by means of two different statistical tools: The flammable fuel mass fraction (f_f) and the Coefficient of Variation

(COV). The first index accounts for the ratio between the quantity of fuel included in a flammable mixture to the total mass of fuel present inside the chamber:

$$f_f = \frac{Mass\ of\ fuel\ in\ flammable\ mixture}{Total\ mass\ of\ fuel} \tag{4.1}$$

For these simulations, the evaluation of the mass of fuel included in the flammable mixture is evaluated by summing up the mass of fuel in all the computational cells whose cell-wise relative air-fuel ratio is in the range of 0.8 to 1.2.The coefficient of variation gives an index of homogeneity over all computed domain and is evaluated considering the standard deviation on mass fraction and dividing it by the average fuel mass fraction:

$$CoV = \frac{\sqrt{\frac{1}{N}\sum_i^N \left([CH_4]_i - \frac{1}{N}\sum_i^N [CH_4]_i\right)^2}}{\frac{1}{N}\sum_i^N [CH_4]_i} \tag{4.2}$$

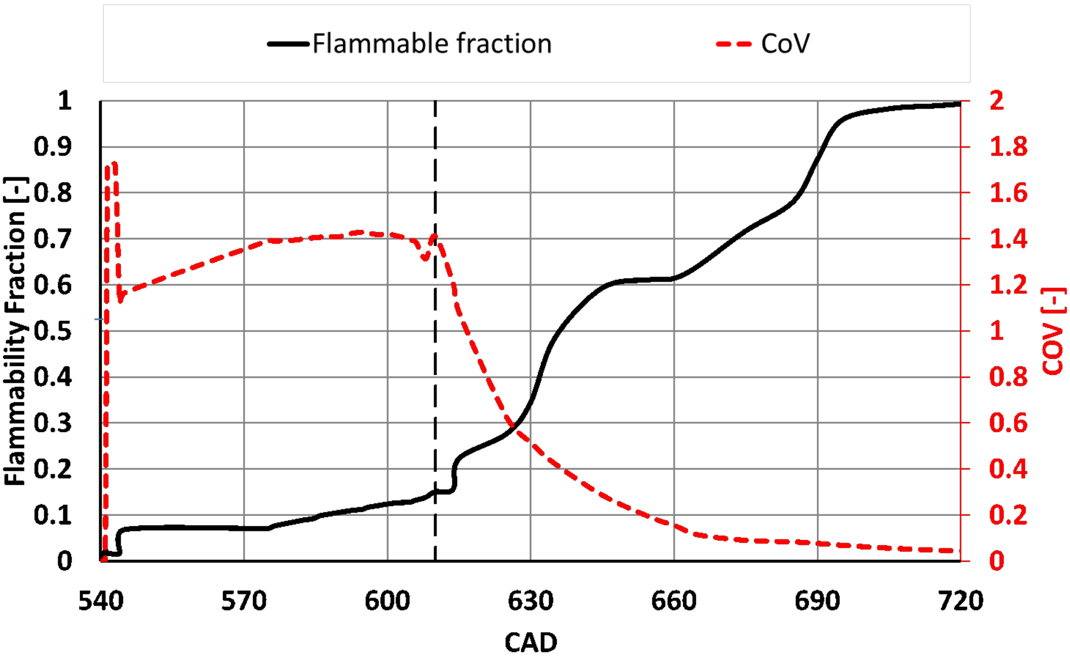

Fig. 4.13 Flammable Fuel Mass Fraction & Coefficient of Variation vs Crank Angle Degrees (1500 RPM at Full Load)

The reported values of f_f and COV (Figure 4.13) shows that despite the reduced time a good mixture has been achieved, in fact can be seen that at top dead centre almost all the fuel is within 20 percent around the stoichiometric value and consequently the degree of homogeneity is acceptably low. The analysis of the behaviour for both the indices could give a better idea about the effectiveness of the mixing and about the distribution of the fuel throughout the chamber volume. On this purpose, it can be noticed that the mixing rate is almost constant during the injection and significantly improves after the end of injection, it is explained considering the motion of the fuel as shown in the iso-contour plots, in fact the fuel flow due to its momentum travels along the chamber in a rich plum without a significant mix. As the injection ends, the trail of the jet is suddenly mixed with the air, as confirmed by the step increase in the flammable fuel mass fraction and the fuel previously injected is transported and mixed with the air.

4.1.6.2 Engine 1: Case – 2000 RPM at 4 bar BMEP

A series of different injection strategies have been tested for the partial load case at 2000 rpm and 4 bar BMEP. At low engine load the engine efficiency is optimized making use of an early intake valve closure (EIVC), this approach inevitably compromises the intake induced charge motion and so deteriorate the turbulence level and the mixing capability. In order to quantify the mixing performances, the flow interaction and the turbulence levels in the chambers, three single injection strategy have been tested moving the injection window from a very late injection which is totally performed after the intake valve closure up to an early injection strategy which is completed at the beginning of the intake phase (Figure 4.14). Additionally, a trade-off between a good mixing and a favourable increase in turbulence has been also investigated considering a double injection strategy. Due to the very different injection timings the flow interacts with the intake air and with the engine geometry in different ways leading to distinct jet evolution and mixing mechanisms.

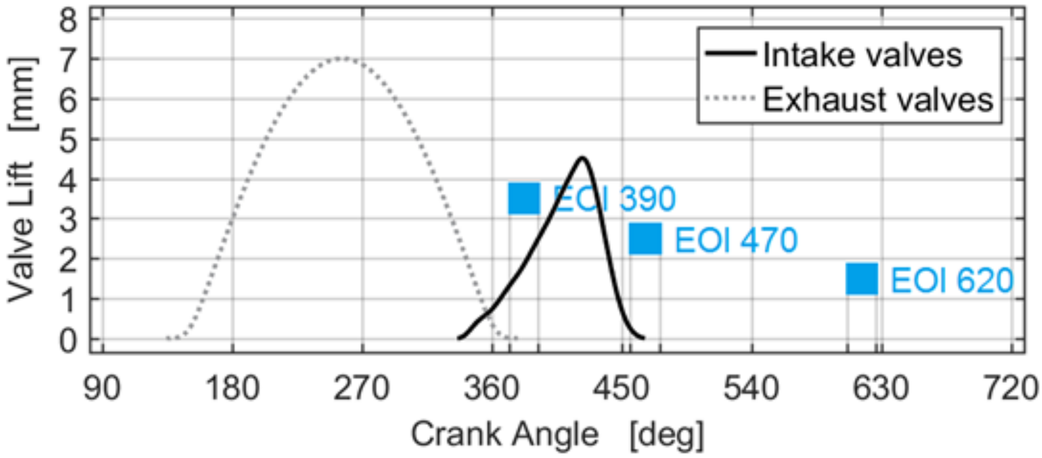

Fig. 4.14 Relative positioning of the injection events with respect to the intake and exhaust valve life (2000 RPM at 4 bar BMEP)

Figure 4.15 reports the A/F contours relative to the three different injection strategies, the image shows the fuel distribution 10 degrees after the start of injection for each case. As expected the biggest difference in the first jet evolution is noted for the earliest injection case, here the injected flow is strongly affected by the piston position and by the air interaction. The piston in fact is responsible for the flow deflection that produce a jet induced counter clockwise tumble opposite to the expected air induced tumble and opposite to the flow path generated for later injections (Figure 4.16) .On the contrary for the intermediate and latest injection strategy the piston is too far to interact with the flow and, in analogy with the Full Load case at 1500 rpm, the Coandă effect is the dominant phenomenon so that the jet follow the roof and the opposite liner side, inducing a positive tumble at the injection start as highlighted in Figure 4.17.

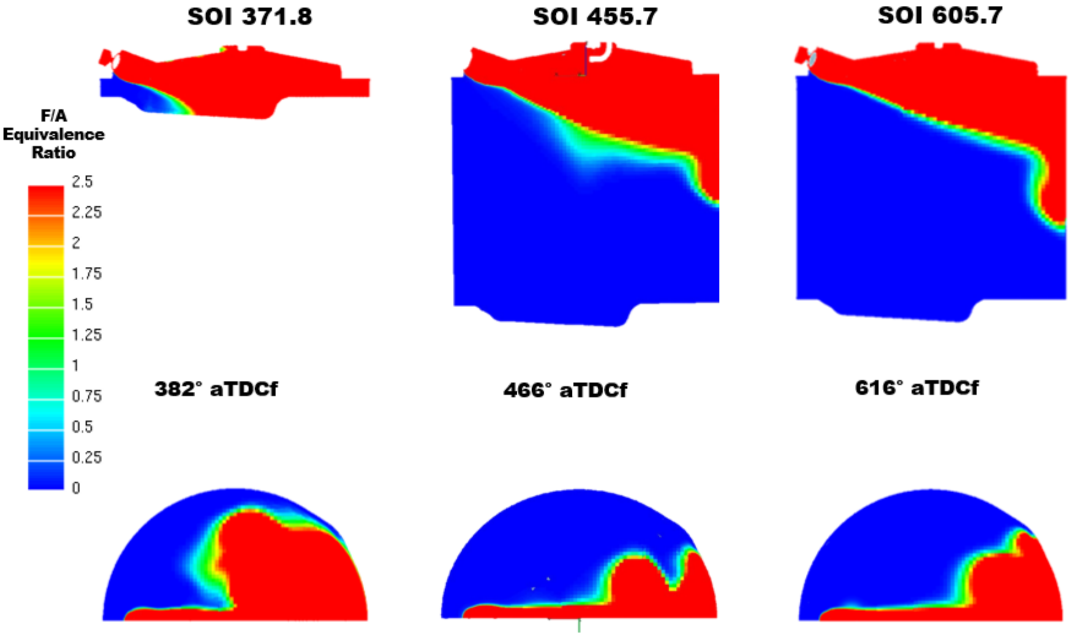

Fig. 4.15 Equivalence Ratio Contours – 10^o after SOI (2000 RPM at Full Load)

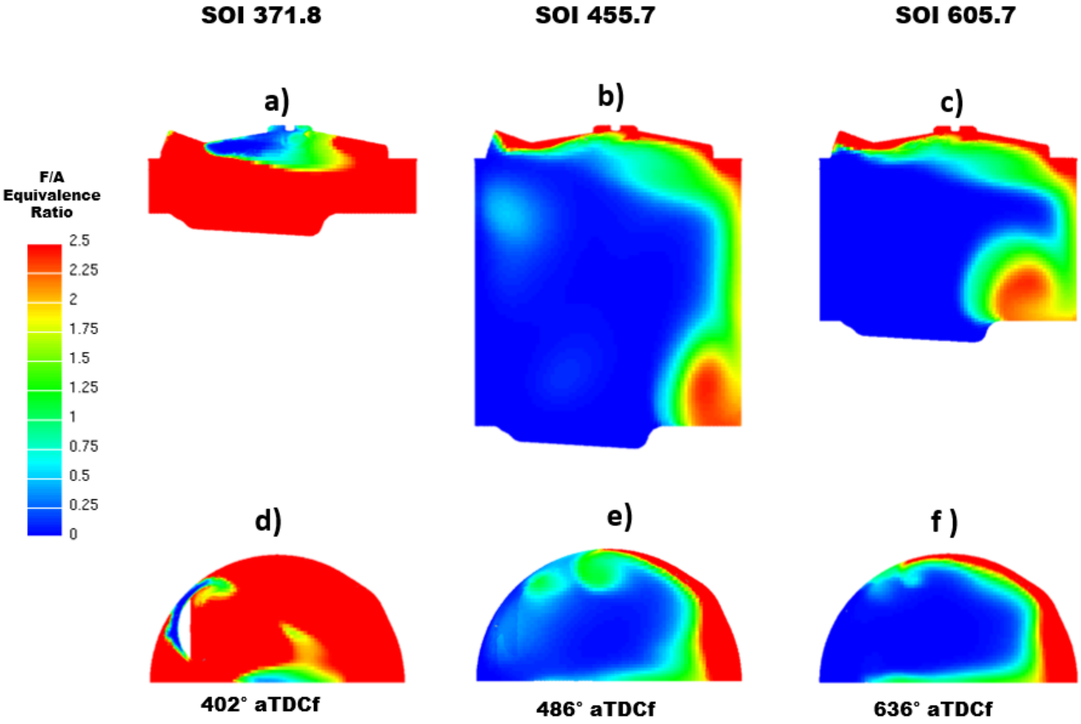

Fig. 4.16 Equivalence Ratio Contours – 30^o after SOI (2000 RPM at 4 bar BMEP)

An interesting overview of the mixing evolution is given in Figure 4.16; At 30 degrees after the start of injection the early injection case appears almost homogeneous, although very rich because of the low air availability during the early intake phase, but a lean zone is visible close to the intake valve due to the fresh air displacement, this shows the peculiarity of such strategy where the incoming air is only responsible for the achievement of a good mixing. In the intermediate and late injection case the flow is still dominated by the liner deflection, that induce a positive tumble on the X-Z plane and a swirl motion in the Y-Z plane (lower row Figure 4.16), the two motions interacts and brings the flow on the intake side as it is visible in Figure 4.16 b.

Even if the mixing mechanisms in the two latest injection cases are similar, the different fluid dynamic condition in the chamber leads to opposite results in terms of mixing, Figure 4.18 shows the equivalence ratio at TDCf with a +/- 20% of the stoichiometric value, the earliest injection case (Figure 4.18 a) is very close to the stoichiometric condition. This was expected due to the relatively long time available for the mixing, on the contrary the other cases show a slight stratification. Surprisingly the fuel distribution is opposite for the two cases. The different stratification between the two cases can be ascribed to the combined swirl/tumble that forms a helical motion from upper exhaust to the lower intake side. Because of the engine symmetry, as soon as the flow reaches the intake side in the symmetry plane and interacts with its opposite side, the flow is pushed toward the exhaust side. This phenomenon can be verified through vector plot (Figure 4.19). The left picture reports the velocity field for the intermediate injection case, relatively high velocity vectors pointing toward the exhaust can be noticed on the intake side. A comparative image is reported also for the latest injection case (Figure 4.19 b), despite the presence of the same helical motion the results are influenced by the piston movement and shape that spin up the tumble vortex which deviates the upward the flow notion on the intake side.

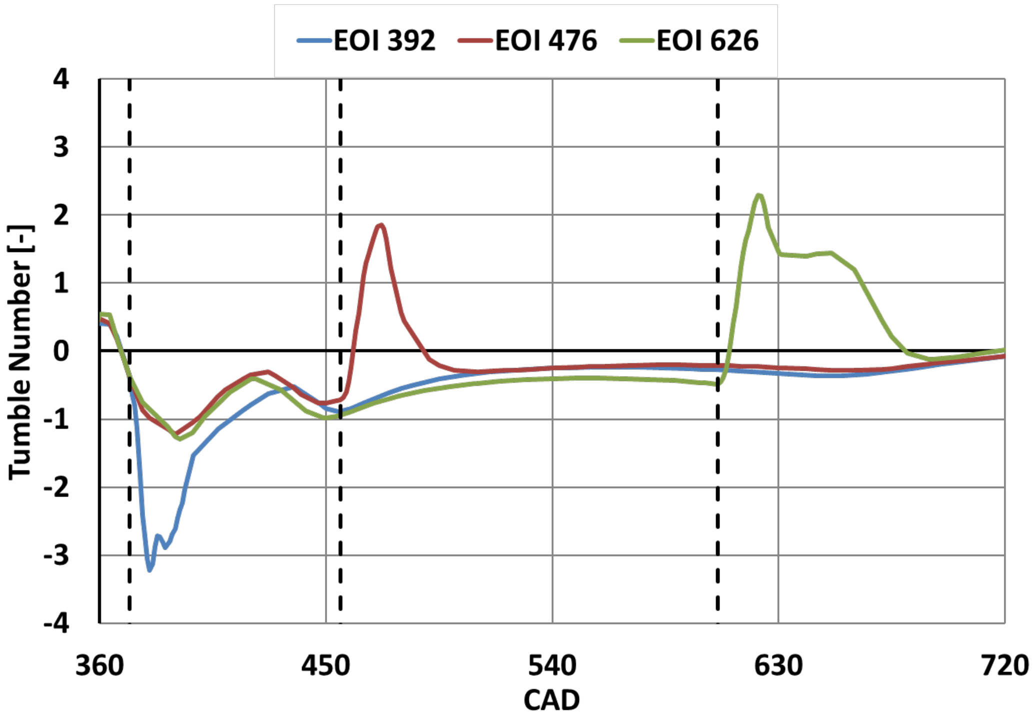

Fig. 4.17 Tumble Number (2000 RPM at 4 bar BMEP))

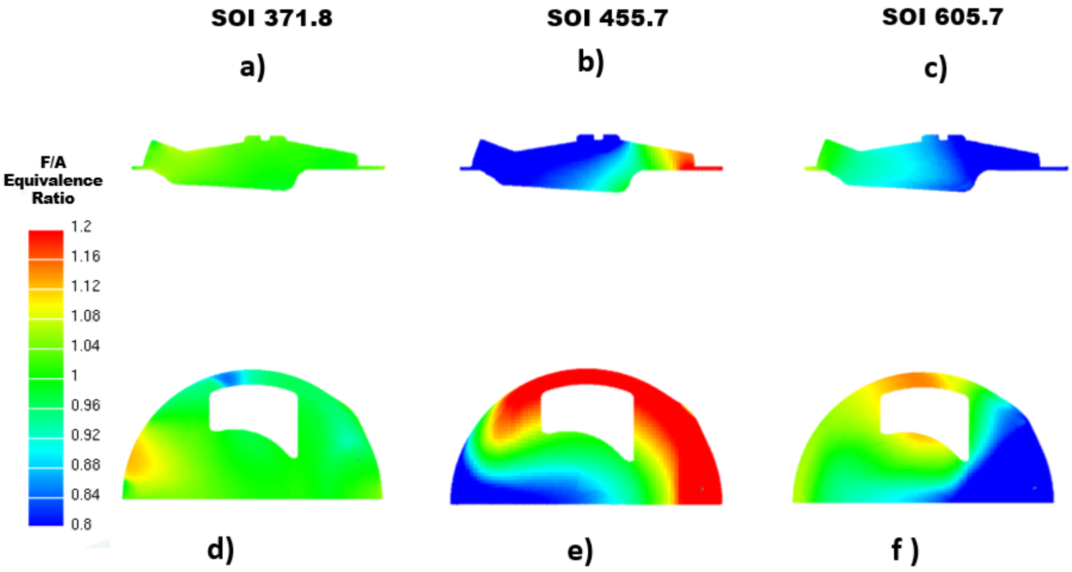

Fig. 4.18 Equivalence Ratio Contours – Top Dead Centre (2000 RPM at 4 bar BMEP))

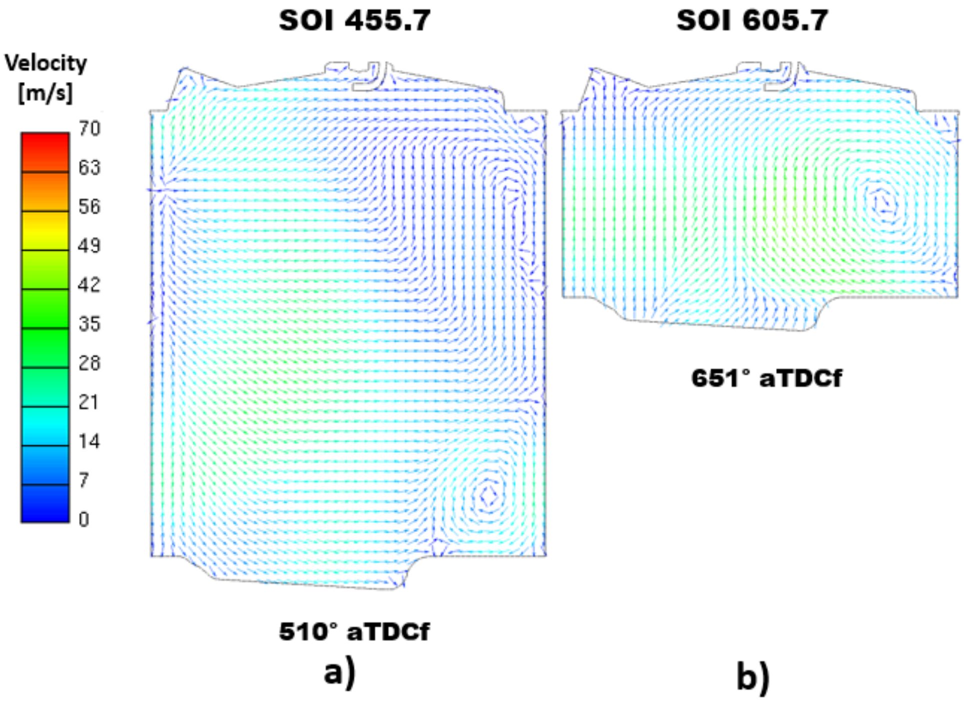

Fig. 4.19 Coefficient of Variation (2000 RPM at 4 bar BMEP)

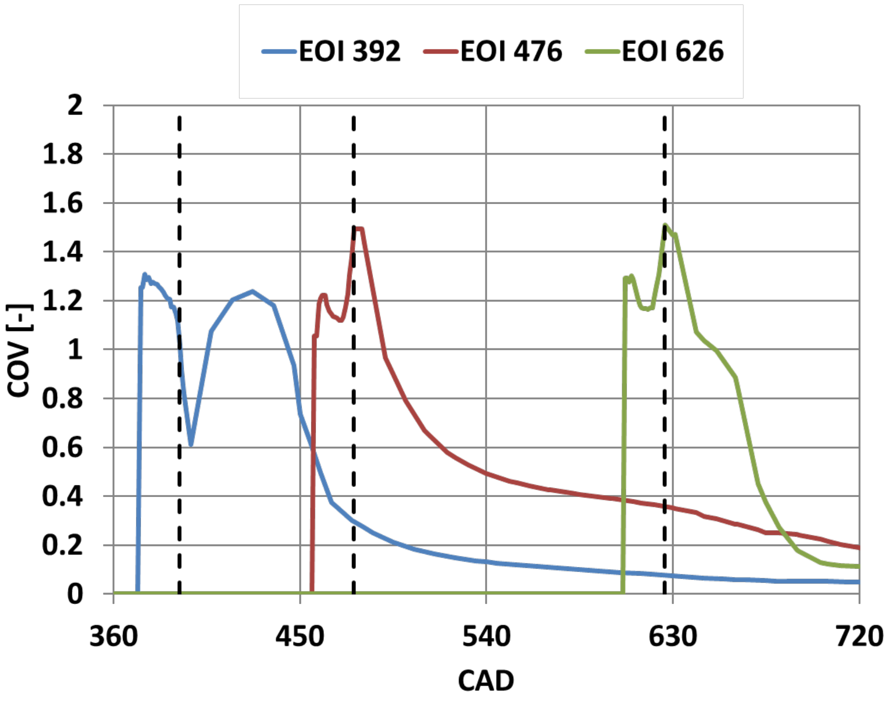

Fig. 4.20 Coefficient of Variation (2000 RPM at 4 bar BMEP

The quantitative analysis obtained through the COV and the Fuel Flammability limit (see Figure 4.20-4.21) substantially confirms the qualitative analysis discussed above. The early injection as expected is confirmed to be the best solution in terms of homogeneity, surprisingly the late injection is found to be more efficient than the intermediate one in terms of mixing. This behaviour is due to the favourable fluid dynamic interaction produced in the late injection case as discussed above. Furthermore, the late injection is beneficial for the induced turbulence level and consequently for combustion stability.

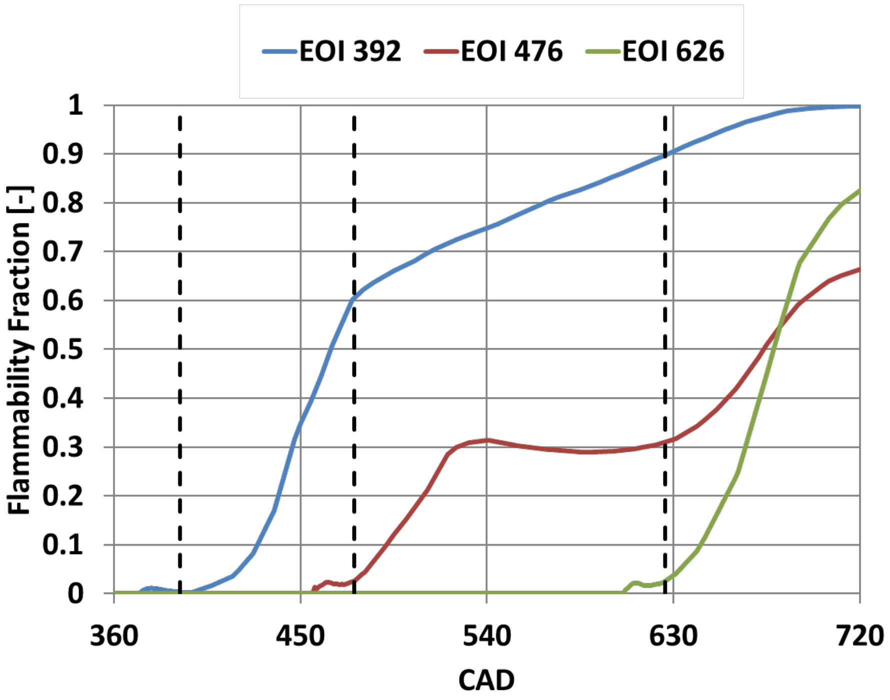

Fig. 4.21 Fuel Flammability Fraction (2000 RPM at 4 bar BMEP)

4.1.6.3 Engine 1: Case – 2000 RPM at 4 bar BMEP with Double Injection

Considering the above analysis, with the aim to optimize both the fuel homogeneity and the turbulence level, a double injection strategy has been tested combining the earliest and the latest strategy. The injection has been divided in two halves, the first event shares the same SOI of the early injection strategy (SOI 371.8), and the second events ends with that of the latest injection analysed (EOI 626) previously.

The results of the simulation can be seen in Figure 4.22. As expected, the Tumble Number and the TKE (Figure 4.22) are enhanced by the second injection event, while the improvement is fuel homogeneity cannot be seen. Thus, the final COV value is found to be slightly higher respect to the late injection strategy (Figure 4.23-4.24). The lower homogeneity level can be explained considering the lower momentum of the charge for the second injection event. The lower jet impulse gives rise to a weaker interaction between the tumble and the swirl bringing to a slower tumble decay as visible in (Figure 4.22). The presence of tumble in the late compression phase create a recirculation zone in the exhaust side that is ineffective for the mixing.

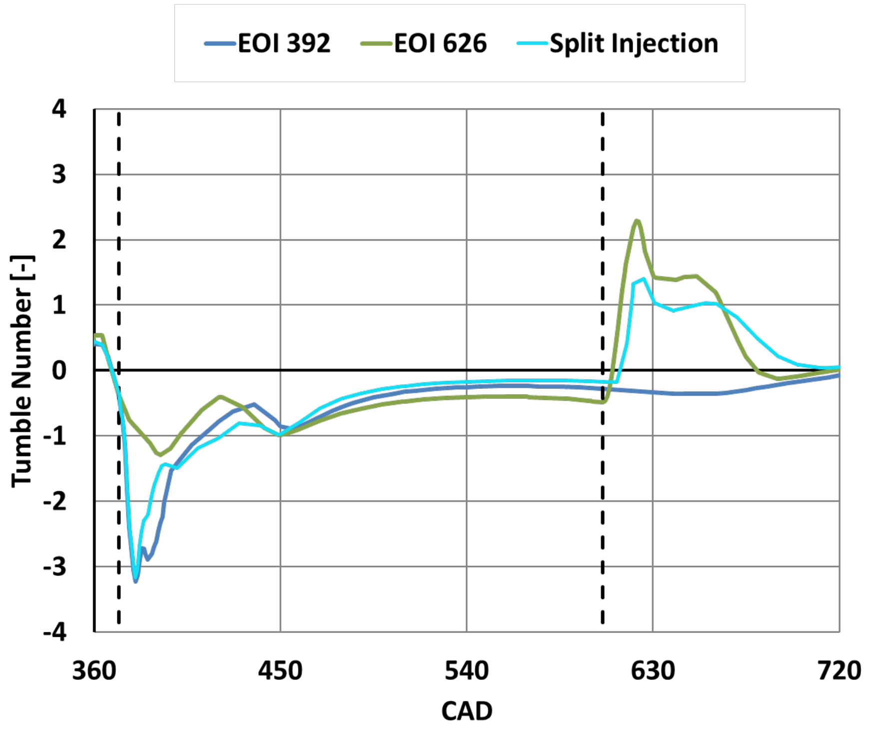

Fig. 4.22 Fuel Flammability Fraction (2000 RPM at 4 bar BMEP with Double Injection)

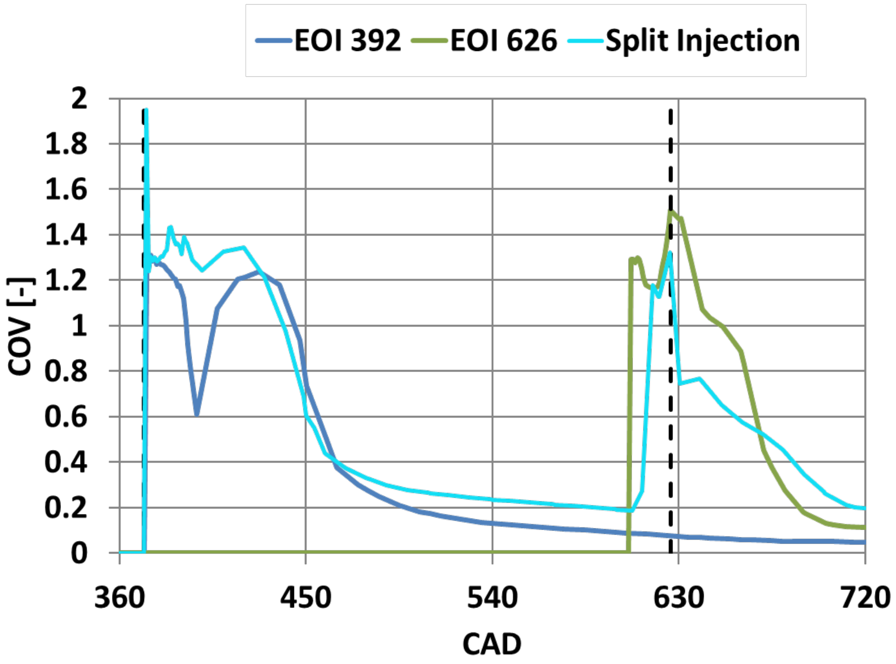

Fig. 4.23 Coefficient of Variation (2000 RPM at 4 bar BMEP with Double Injection)

Figure 4.25 compares the flow field at 680 CAD for two cases (EOI 626 and Double Injection), the higher flow velocity in Figure 4.25-b is clearly visible while the undisturbed tumble is visible for the double injection case in Figure 4.25-a.

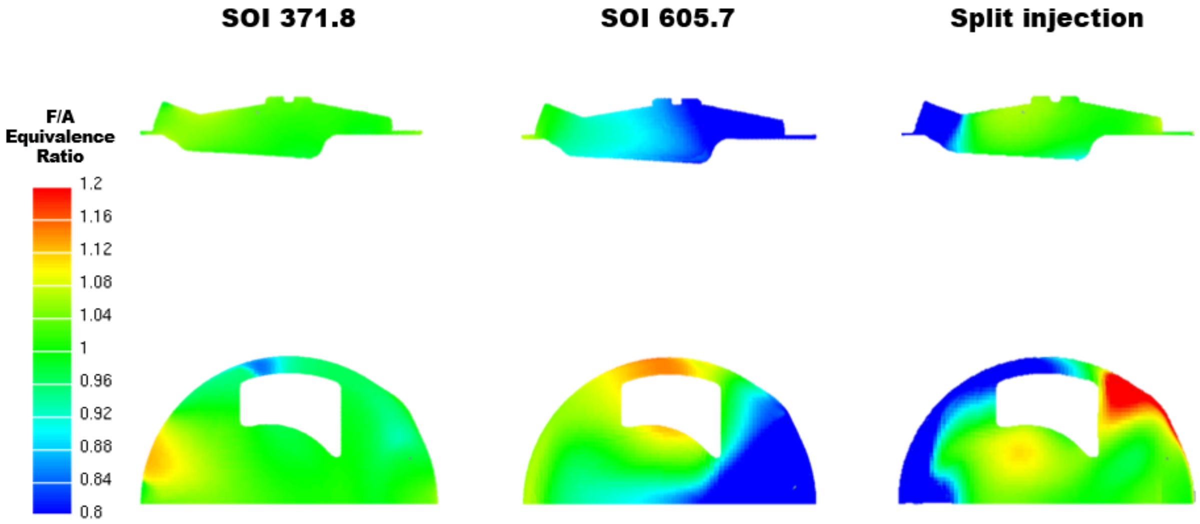

Fig. 4.24 Equivalence Ration Contours – Column 1: Early Injection at 371.8^{o}, Column 2: Late Injection at 605.7^{o}, Column 3: Split Injection

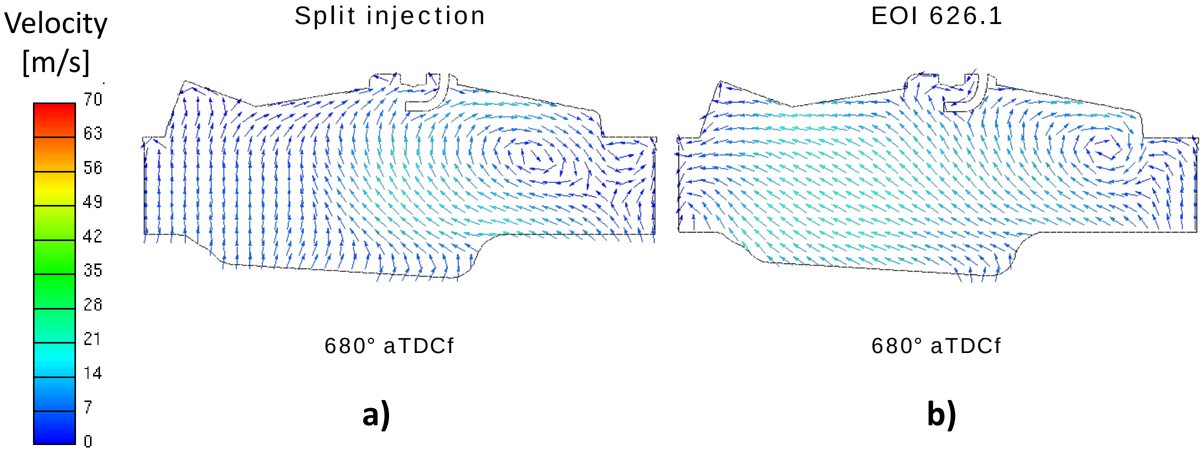

Fig. 4.25 Coefficient of Variation (2000 RPM at 4 bar BMEP with Double Injection)

4.1.6.4 Engine 1: Case – 5500 RPM at Full Load

A further investigation has been conducted on the engine prototype 1, a full load case at high engine speed is tested, three different injection timings are also evaluated considering the relative effect on mixture and turbulence formation. The possible injection windows for the considered case is much narrow respect to the partial load case because of the relatively high quantity of fuel needed and the high engine revolution speed that reduces the crank angle range available for the injection event. The earliest and latest injection are shifted by 53 degrees, despite this relatively small difference in terms of degrees the strong interaction between the jet and the incoming air strongly affect the mixture formation.

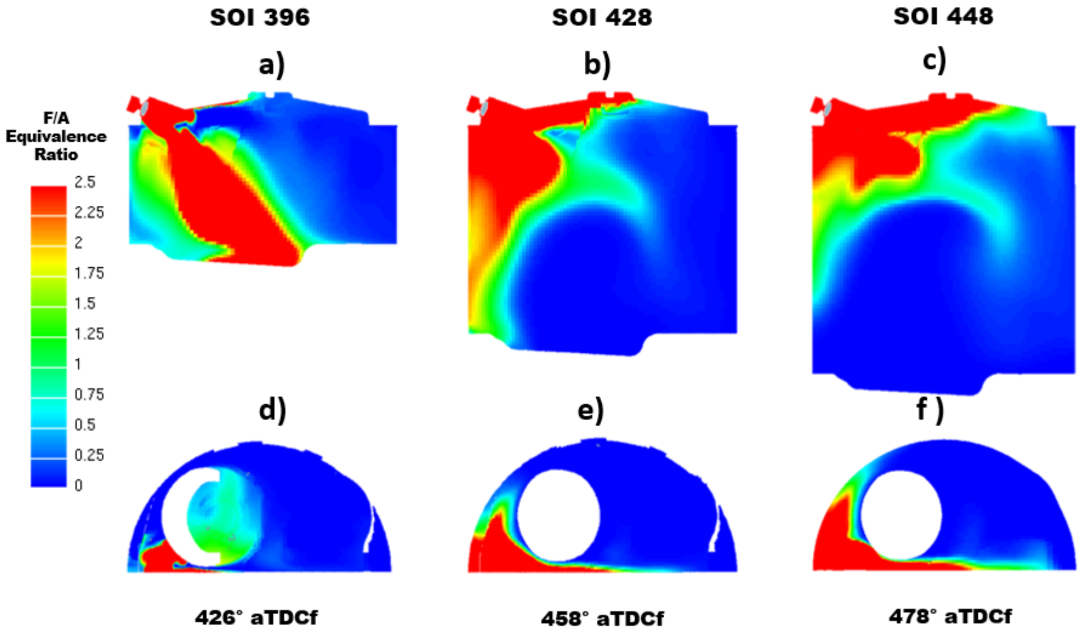

Fig. 4.26 Equivalence Ration Contours at 30^o aSOI; Top Row – Symmetry Plane, Bottom Row – Z-Axis Plane through the Injector (5500 RPM at Full Load)

Figure 4.26 reports the equivalence ratio value for the three cases 30 degrees after the start of injection, in opposition to what already seen at low engine speed and at partial load case the higher valve lift and the incoming flow momentum deflect the flow and prevent the appearance of the Coandă effect. The flow deflection is much higher for the earliest injection case, since it is completely performed during the maximum valve lift period, and the higher air/fuel interaction brings to a higher mixing rate in the first injection period phase as confirmed by the Flammability Fraction plot (Figure 4.27).

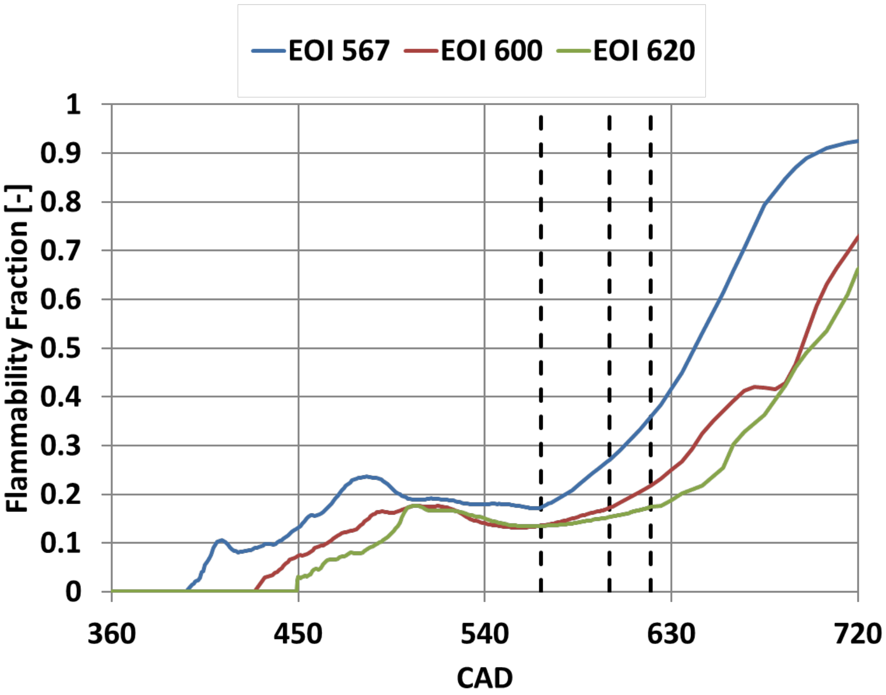

Fig. 4.27 Fuel Flammability Fraction (5500 RPM at Full Load)

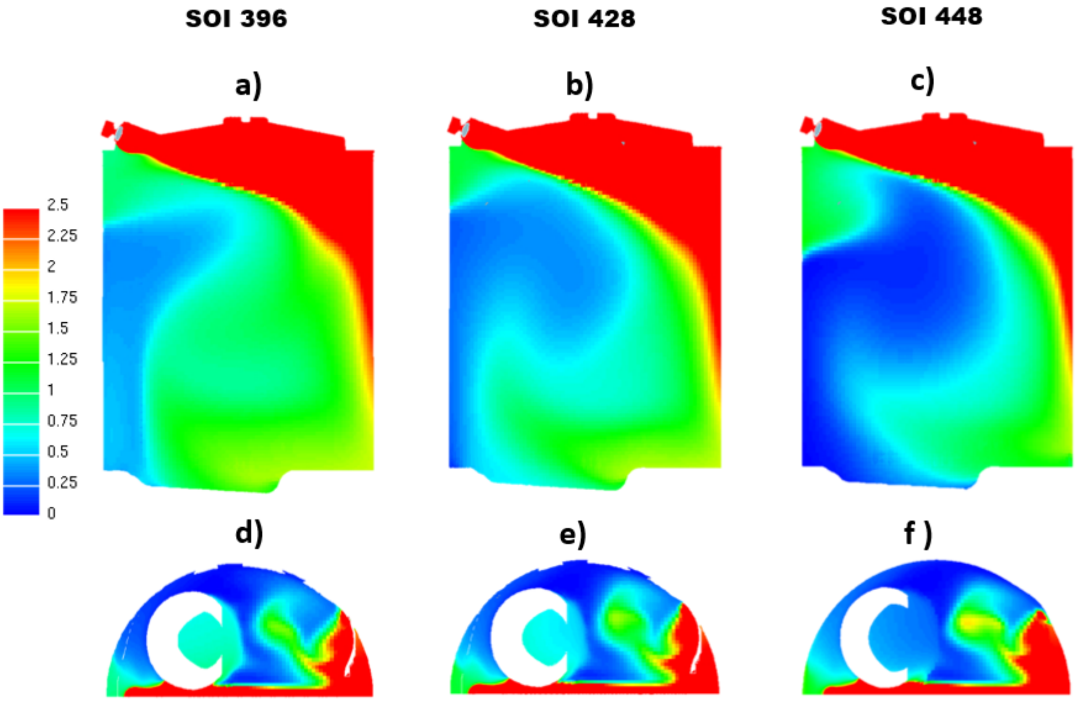

Fig. 4.28 Equivalence Ratio Contours at Bottom Dead Centre (5500 RPM at Full Load)

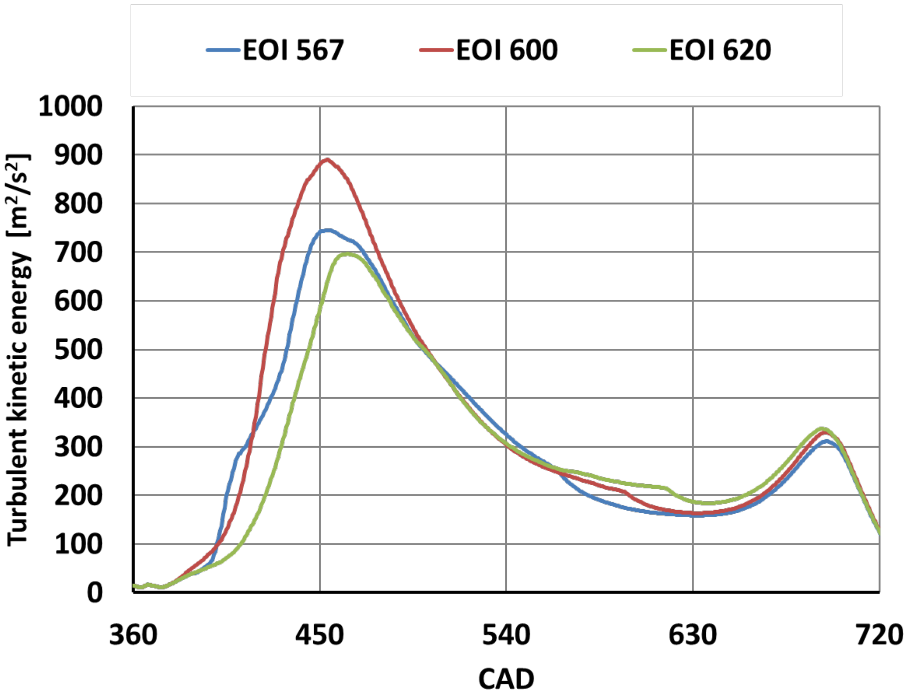

Fig. 4.29 Turbulence Kinetic Energy (5500 RPM at Full Load)

As the valve lift reduces and consequently the air momentum decreases the Coandă effect appears, Figure 4.28, the combination of jet induced and strong air induced tumble present for this engine point conveys the fuel in a circular path all around the liner border and the piston top creating a central lean “eye”, this tendency results to be higher for the late injection case due to the minor deflection applied to the jet in the initial injection stage. Finally, the fuel shows a similar distribution for all the tested cases with a rich pocket on the intake side specifically concentrated in the injector cavity, such fuel unevenness increases as the injection event is delayed. In fact, for the earliest injection case more than the 90% of the fuel is in the range of 0.8-1.2 of RAFR as reported in the flammability chart (see Figure 4.27). In this case, due to the higher intake air momentum and the strong intake induced tumble, the injection influence becomes negligible on the turbulence formation and thus the final turbulence level results to be not substantially affected by the injection timing, figure 4.29.

4.1.6.5 Engine 2: Case – 1750 RPM at 4 bar BMEP

In analogy to what was observed in the Engine prototype 1, a full load case at 1750 rpm and a partial load (i.e. 4 BMEP) case at 2000 rpm have been tested for the second engine. The different engine characteristics significantly modify the mixing processes, here in fact the steeper angle between the injector and the plane normal to the cylinder is not favourable for the Coandă effect and the fuel is directly injected in the chamber without any interaction with the walls. The Full load case simulated at 1750 rpm is roughly comparable with the low load case tested for the Engine 1. Figure 4.30 shows the fuel path at 10 and 30 degrees after the start of injection and is it possible to notice that the flow does not interact with the jet until it reaches the corner opposite to the nozzle. The tumble number and the Turbulent kinetic values reported in figures 4.24-4.25 confirm the higher tendency of the engine to form a higher tumble motion.

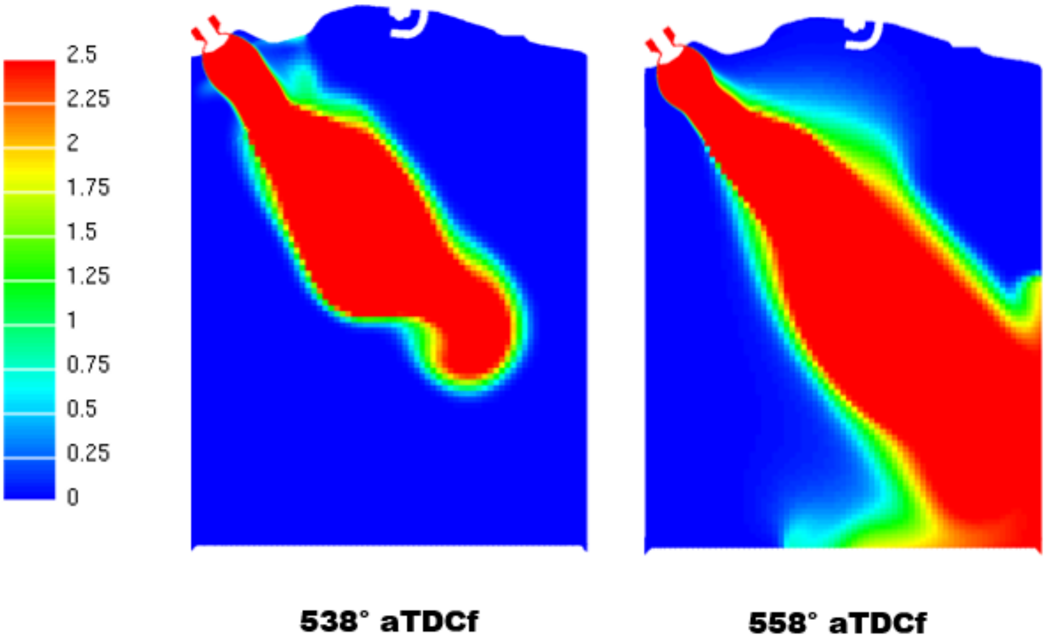

Fig. 4.30 Equivalence Ratio Contours. Column 1 – 10^o after SOI, Column 2 – 30^o after SOI (1750 RPM at 4 bar BMEP)

It also worth noticing that despite the injected fuel is directed against the tumble, it does not destroy the motion. This positive interaction between tumble and injection is due to the very far impingement point that leaves enough room for the sustainment of the tumbling vortex. The overall mixing performance is found to be good and the final COV value results are in accordance to the equivalent case considered for the Engine 1.

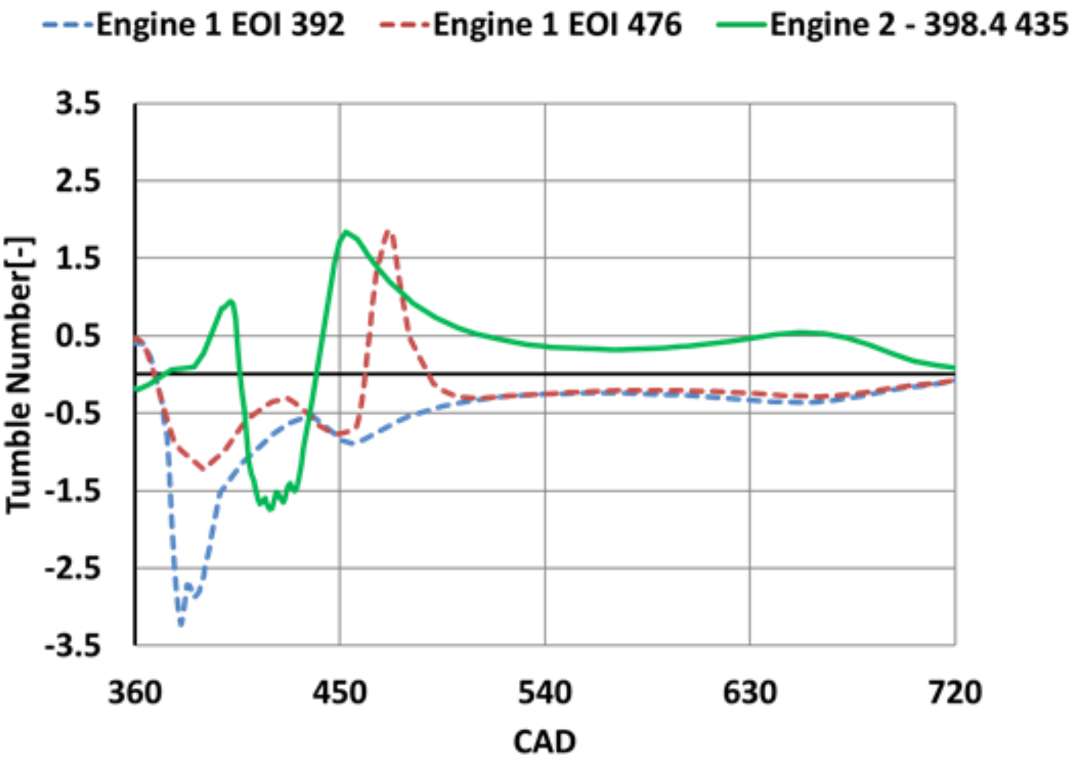

Fig. 4.31 Tumble Number – Engine 1 vs Engine 2

The partial load case at 2000 rpm and 4 bar BMEP shows a similar jet shape but the closer presence of the piston leads to a stronger flow deflection that acts against the main tumble, this is evident observing the plot in figure 4.31; the clockwise tumble created by the incoming flow is reversed during the injection; despite that the strong tumbling tendency of this engine prevails at the end of the injection period producing a tumble level even higher than the similar cases analysed in the other prototype.

4.1.7 Optical validation

The numerical simulation results were validated by experimental investigations performed on an optically accessible single cylinder engine (SCE) with the help of planar LIF technique. LIF is a spectroscopic method based on the excitation of molecules of a predetermined species, called tracer, to a higher energy state through selective absorption of photon (the laser pulse) followed, in a few nanoseconds or microseconds, by the spontaneous de-excitation through the emission of another photon at a longer wavelength, i.e. the fluorescence. Typically,pulsed excimer lasers, in the ultraviolet (UV) region of the spectrum with relatively low energy but high pulse repetition, are adopted for LIF experiments owing to their well-defined wavelengths. With respect to the MCE, the experimental SCE features a modified head, to enable optical access to the combustion chamber. Also, the compression ratio has been reduced with respect to the MCE to account for the engine peak firing pressure, and a specific glass liner was built for lateral optical accessibility. The engine was run without lubrication, so as to improve the quality of measurement data as far as possible. It is worth being underlined that the glass liner imposed some constraints to the experimental procedures. Specifically, the engine could be operated only for a limited number of cycles, especially at high load. For this reason, the engine was firstly motored, and, when all the relevant parameters were set, combustion was enabled for about 200 cycles of which only the latest 50 were measured, so as to ensure that the actually measured cycles correspond to steady state conditions to the greatest possible extent. It is inevitable that the liner temperature was on the one hand different from that in the full engine, and on the other hand more dependent on the investigated operating points. Although the combustion behaviour was not fully comparable to that in the full engine, the effect of injection timing at given speed and load was still meaningful.

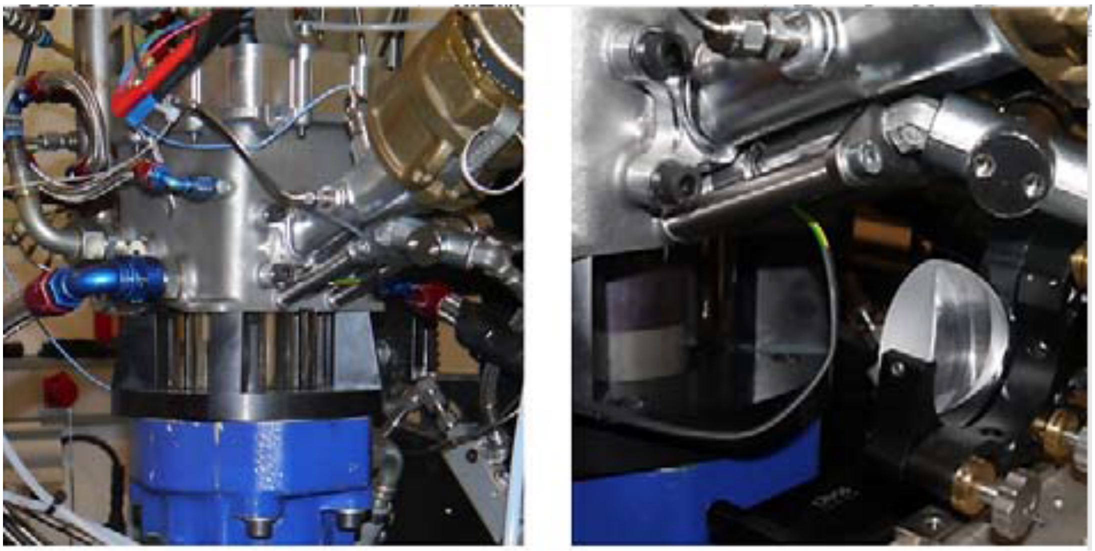

Fig. 4.32 Planar LIF experimental setup. Left Image – optical single-cylinder engine; Right image – last lens used to couple the light sheet from the intake side

The double-sided planar LIF was implemented in the investigation, wherein via a system of lenses and mirrors a krypton fluoride (KrF) excimer laser beam (wavelength 248 nm) was reshaped and evenly split into two planar light sheets that were then coupled into the same symmetry plane of the combustion chamber from two opposite sides through the glass liner. Such arrangement guaranteed symmetrical illumination of the target symmetry plane which is the vertical plane passing through the cylinder central axis and leaving one intake valve and one exhaust valve on each side. Figure 4.32 shows the optical engine configuration including the glass liner and one of the two final lenses of the laser path used to illuminate the target plane.

The optical engine was fuelled by methane uniformly premixed with 4000 ppm of trimethylamine, $N(CH_3)_3$ or TMA, as the tracer for LIF visualization. TMA was found to be a suitable tracer in this application thanks to its branched molecular structure giving rise to a large number of excitable energy states for a broadband excitation by the KrF excimer laser at the wavelength of 248 nm, the wavelength at which methane and nitrogen do not absorb light. The subsequent emission fluorescence at the wavelength of about 300 nm was imaged by an intensified charge-coupled device (ICCD) camera with an image-intensifier quantum efficiency of around 20% at 300 nm and an UV-compatible Micro Nikkor lens.

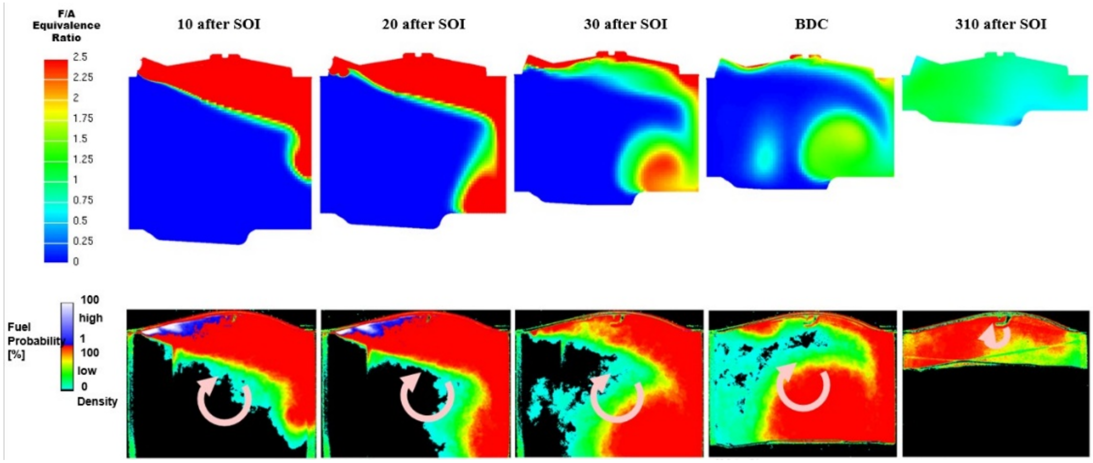

Fig. 4.33 Comparison between experimental and simulated results for EOI 100- statistical evaluation of experimental PLIF images Case - 2000 RPM at 4 bar BMEP

The results of the experiment performed on the optical engine are very encouraging and resemble very closely to the results of the CFD simulations. Figures 4.33,4.34 report the result for the cases of EOI 100 and EOI 334 at various stages of the mixing cycle. The first row represents the CFD results while the second row reports the experimental images. It is also to be noted that the experimental images represent the probability of the fuel and not the concentration. However, the flow patterns obtained through the experiments are completely in line with the experimental simulation and report a close one-to-one correlation. Also, the 'Coandă effect' can be seen in the experimental images. In addition, the clockwise tumble motion predicted by the numerical model is also apparent in the PLIF images. Thus, the robustness of the CFD model is verified.

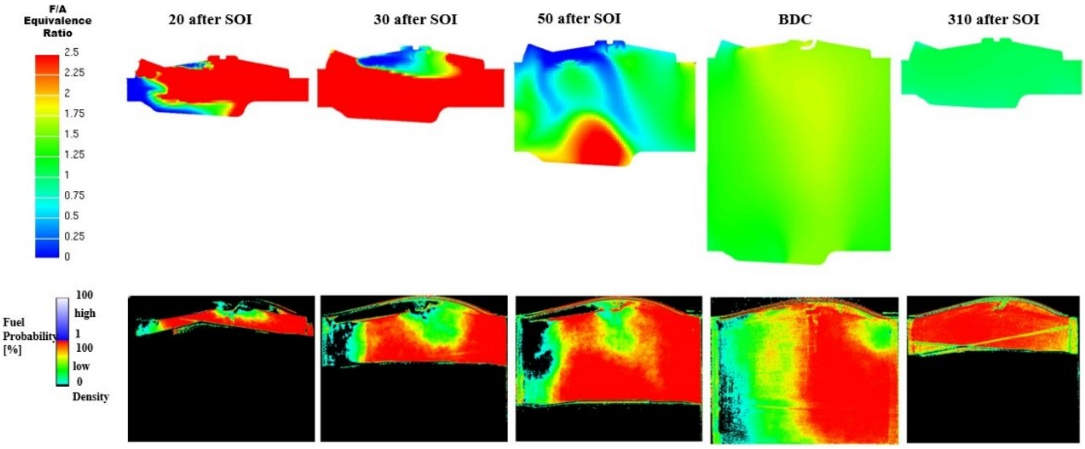

Fig. 4.34 Comparison between experimental and simulated results for EOI 334 – statistical evaluation of experimental PLIF images Case - 2000 RPM at 4 bar BMEP

Chapter 5

Conclusion

The present work aimed at providing a contribution to the development of high efficiency natural gas engines through the optimization of the in-cylinder charge motion as well as the design of a reliable direct injection system. The first section of the work was focused on the optimization of the combustion chamber for a high-performance engine featuring very high compression ratios specifically developed for CNG. The experimental and numerical characterization of steady-state tumble flow generated by two different head designs was performed. Moreover, a numerical model for the transient combustion simulation of the engine cycle was developed and assessed for. Experimental tests were carried out at Fiat Research Center and allowed for measuring the steady-state tumble number with two different methods, namely the Ricardo method and the two-dimensional HWA one. The HWA technique was originally developed by CRF and thus represented an innovative feature of the work. Furthermore, the combined use of experimental and numerical analysis techniques provided useful insight into some important topics such as the intrusiveness of the measurement methods as well as the correlation between the flow rig CFD simulations and the engine ones. The main conclusions can be summarized as follows:

- The one-dimensional HWA technique represents an effective alternative to the traditional Ricardo method for the tumble quantification. In the considered engines, the two techniques provided a good match with the HWA method assessing for an average 10% lower tumble with respect to the value addressed by the Ricardo method.
- Although the HWA method cannot be considered as a fully differential technique, it allows additional information to be provided about the flow distribution throughout the measurement plane, with specific reference to the asymmetry generated by the intake system. As far as costs are concerned, the HWA apparatus and the Ricardo setup are almost equivalent.

- The steady state tumbling flow from the engine cylinder head was also characterized from a numerical point of view. The developed model features a minimum cell size of 0.3 mm in the valve throat and an overall cell count of about 4,200,000. The results presented in the paper demonstrate the model capability to capture the integral features of the tumbling flow. The model can thus be used as a predictive tool to assess for the impact of the cylinder-head design variables on the tumble intensity.
- From a practical point of view, the Standard cubic model did not prove to appreciably improve the accuracy of the results with respect to the Realizable one. Moreover, the increased computational cost and instability of the former model constitutes a considerable drawback.
- The numerical activity on the 'virtual test bench' model also allowed for the estimation of the flow straightener effect on the flow pattern. The straightener not only constitutes an additional resistance but also decouples to some extent the cylinder volume from the downstream environment, thus influencing the streamlines aspect. Still, the perturbation induced by the straightener, which is representative of the HWA technique intrusiveness, showed to hold a minor effect on the flow pattern with respect to the differences produced by inevitable changes from the test rig set-up to the real engine layout.
- The effect of the intake masking has been evaluated with experimental and numerical test procedures. It can be concluded that the enhancement on the tumble formation more than offset the volumetric losses due to the intake restriction.
- Despite the validity of the static test rig analysis complete comprehension of the transient fluid dynamic processes in the cylinder can be only obtained with a complete engine model. The transient numerical model for the complete engine has been developed on the bases of the static test rig model. The model is considered reliable enough for the comparative analysis between different engine geometries and/or actuation strategies
- Different compression ratio solutions have been tested both numerically and experimentally. The study considered the benefit achievable on fuel efficiency and the drawbacks coming from higher cycle instability. The best compromise is found in the engine design with compression ratio 13.
- The effectiveness of the intake masking on the turbulence formation and consequently on the combustion stability has been confirmed by the complete engine model. The intake masking gives the highest contribution for tumble formation at low load/low lift condition counterbalancing the negative influence of an early intake valve closure.

In the second part of the work a numerical study of a direct injection engine fueled with Natural gas was performed. The actual geometry and the realistic movement of an outward opening nozzle was correctly reproduced in the numerical model. The challenging simulation task due to the high velocity and pressure ratio between the incoming fuel and the surrounding flow was correctly faced through an accurate mesh procedure and a dedicate numerical study. Two different engine prototypes were evaluated over several engine speeds and loads. The numerical model was qualitatively validated against optical experimental data provided by AVL. An accurate quantitative interpretation of the correlation between detected luminosity at optical test and equivalence ratio requires dedicated multiple LIF measurement and calibration and is under study. The main conclusions can be summarized as follows:

- The model shows to be reliable and accurate for the simulation of the high pressure injection, with correct prediction of the main engine relevant quantities like mixing quality and turbulence level.
- The simulation results highlighted that the adoption of a side-mounted injector with injector axis almost parallel to the chamber wall is effective in promoting an efficient mixing process. The Coandă effect induced by the vicinity of the cylinder head enhances the tumble motion and is the main mixing mechanism for intermediate and late injection timings. On the contrary the for early injections the main mixing mechanism is given by the jet impingement on the piston.
- As general trend the earliest injection results in a better fuel homogenization due to a longer time available for the mixing, while a retarded injection turns out to be beneficial for the turbulence intensity. However, the mixing trend is not always monotonic and some exceptions are found for specific engine points. Thus the CFD analysis of the jet interaction with the flow and with the walls is an effective guideline for the selection of the best injection strategy.
- A different injection orientation, featuring a steeper angle between the injector and the plane normal to the cylinder, was also investigated. In such a case, the mixing is mainly induced by the interaction between the jet and the tumble motion and also by the piston deflection. The injection event with this particular solution shows to be not always positive for the tumble since the jet would tend to generate an opposite tumble.

References

[1] King SR. The impact of natural gas composition on fuel metering and engine operational characteristics. SAE Paper 920593, 1992.

[2] Borges LH, Hollnagel C, Muraro W. Development of a Mercedes- Benz natural gas engine M366LAG with a lean-burn combustion system. SAE Paper 962378, 1996.

[3] Sobiesiak A, Zhang S. The first and second law analysis of spark ignition engine fuelled with compressed natural gas. SAE Paper 2003- 01-3091, 2003.

[4] Ting DSK, Checkel MD. The effects of turbulence on spark-ignited, ultra lean, premixed methane–air flame growth in a combustion chamber. SAE Paper 952410, 1995.

[5] Einewall P, Tunesta P, Johansson B. Lean burn natural gas operation vs. stoichiometric operation with EGR and a three way catalyst. SAE Paper 2005-01-0250, 2005.

[6] Ryan TW, Lestz SS. The laminar burning velocity of isooctane, n-heptane, methanol, methane, and propane at elevated temperatures and pressures in the presence of a diluent. SAE Paper 800103, 1980.

[7] Kataoka K, Hirooka S, Fukatani N, Kadota T. Combustion process of gaseous fuels in a closed vessel. JSAE Rev 1994;15:235–7.

[8] Yamamoto Y, Sato K, Matsumoto S (1994) Study of combustion characteristics of compressed natural gas as automotive fuel. SAE paper 940761

[9] Peters, Norbert. Turbulent combustion , ISBN 0-521-66082-3

[10] World energy outlook, 2016

[11] G.P. Beretta,M. Rashidi and K.C. Keck, Combustion and flame 52:217- 245 (1983)

[12] Theoretical and numerical combustion: Thierry Poinsot, D. Veynante

[13] Veynante, D.Vervisch, L. 2002 Turbulent combustion modeling. Prog. Energy Comb. Sci. 28, 193 - 266.

[14] Wheeler, R.V 1918 J. Chem. Soc. 113, 840

[15] Lafitte, P. 1939, La propagation des flames dans les melanges gezeux, Hermannn et Cie, PARIS

[16] Varde KS, Patro N, Drouillard K. Lean burn natural gas fueled SI engine and exhaust emissions. SAE Paper 952499, 1995.

[17] Kato T, Saeki K, Nishide H, Yamada T. Development of CNG fueled engine with lean burn for small size commercial van. JSAE Rev 2001;22:365–8.

[18] Das A, Watson HC. Development of a natural gas spark ignition engine for optimum performance. Proc Inst Mech Eng, Part D: J Automob Eng 1997;211:361–78.

[19] Chen SK, Beck N J. Gas engine combustion principles and applications. SAE 2001-01-2489, 2001.

[20] Segawa D, Kadota D, Mizobuchi T, Kataoka K, Fukano Y. Effect of fluid flow on combustion process of natural gas in a rapid compression combustor. SAE Paper 961937, 1996.

[21] Evans RL, Blaszczyk J, Matys P. An experimental and numerical study of combustion chamber for lean-burn natural gas engines. SAE Paper 961672, 1996.

[22] Kubesh JT, Podnar DJ, Colucci CP. Lean limit and performance improvements for a heavy-duty natural gas engine. SAE Paper 961939, 1996.

[23] Lancaster DR, Krieger RB, Sorenson S, Hull WL. Effects of turbulence on spark ignition engine combustion. SAE Paper 760160, 1976.

[24] Ting DSK, Checkel MD, Haley R, Smy PR. Early flame acceleration measurements in a turbulent spark-ignited mixture. SAE Paper 940687, 1994.

[25] Mirko Baratta , Daniela Misul, Ezio Spessa, Ludovico Viglione, Giorgio Carpegna, Francesco Perna (2017)-Experimental and numerical approaches for the quantification of tumble intensity in high-performance SI engines. In: ENERGY CONVERSION AND MANAGEMENT, vol. 138, pp. 435-451. - ISSN 0196-8904

[26] Jante A. Scavenging and other problems of two-stroke cycle spark-ignition engines. SAE Tech Paper 680468; 1968

[27] Xu H. Some critical technical issues on the steady flow testing of cylinder heads. SAE Paper 2001-01-1308; 2001.

[28] CD-Adapco, Star-CCM+ v. 8.06 User Guide; 2013.

[29] Amirnordin SH et al. Pressure drop prediction of square-cell honeycomb monolith structure. Int proc of chemical, biological and environmental eng 2011;8:281–5

[30] Lin M, Peng W. Steady flow test and numerical simulation of a GDI engine. In: Bo WU, editor. Proceedings of the 2nd international conference on electronic and mechanical engineering and information technology. Atlantis Press; 2012

[31] Basara B. An eddy viscosity transport model based on elliptic relaxation approach. AIAA J 2006;44(7):1686–90.

[32] Bianchi GM, Cantore G, Fontanesi S. Turbulence modelling in CFD simulation of ICE intake flows: the discharge coefficient prediction. SAE Tech Paper 2002-01- 1118, also in SAE 2002 Trans. J Engines 2003;111(3).

[33] Bianchi GM, Fontanesi S. On the applications of low-Reynolds cubic k-e turbulence models in 3D Simulations of ICE intake flows. SAE Tech Paper 2003- 01-0003, also in SAE 2003 Trans. J Engines 2004;112(3).

[34] Mariani F, Cavalletti M. Dependence of flow characteristics of a high performance S.I. Engine intake system on test pressure and tumble generation conditions - Part 2: numerical analysis. SAE Tech Paper 2004-01-1531; 2004

[35] Rodi W. Experience with two-layer models combining the k-e model with a one-equation model near the wall. In: 29th aerospace sciences meeting, January 7–10, Reno, NV, AIAA 91-0216

[36] Reichardt H. Vollstaendige Darstellung der turbulenten Geschwindigkeitsverteilung in glatten Leitungen. Z Angew Math Mech 1951;31(7):208–19.

[37] Shih TH, et al. A New k-e eddy viscosity model for high Reynolds number turbulent flows - model development and validation. NASA TM 106721; 1994.

[38] Lien FS, Chen WL, Leschziner MA. Low Reynolds number eddy-viscosity modeling based on non-linear stress-strain/vorticity relations. In: Proceedings of third symposium on engineering turbulence modeling and measurements, Crete, Greece

[39] Launder BE, Spalding DB. Lectures in mathematical models of turbulence. London: Academic Press; 1972.

[40] Reynolds WC. Modeling of fluid motions in engines — an introductory overview. Plenum, New York: Combustion modeling in reciprocating engines; 1980. p. 41–65.

[41] Craft TJ, Launder BE, Suga K. Development and application of a cubic eddy viscosity model of turbulence. Int J Heat Fluid Flow 1996;17:108–15.

[42] Yakhot V, Orszag SA. Development of turbulence models for shear flows by a double expansion technique. Phys Fluids A 1992;4(7):1510–20.

[43] Buhl S, Gleiss F, Koehler M, et al. A combined numerical and experimental study of the 3D tumble structure and piston boundary layer development during the intake stroke of a gasoline engine. Flow Turbulence Combust 2016:1–22

[44] Li Y, Jia M, Liu Y, et al. Numerical study on the combustion and emission characteristics of a methanol/diesel reactivity controlled compression ignition (RCCI) engine. Appl Energy 2013;106:184–97.

[45] Han Z, Reitz RD. Turbulence modeling of internal combustion engines using RNG k–epsilon models. Combust Sci Technol 1995;106(4–6):267–95

[46] Baratta M, Catania AE, Spessa E, Liu RL. Multidimensional predictions of incylinder turbulent flows: contribution to the assessment of k-e turbulence model variants for bowl-in-piston engines. ASME Trans, J Eng Gas Turb Power 2005;127:883–96.

[47] Harshavardhan B, Mallikarjuna JM. Effect of piston shape on in-cylinder flows and airefuel interaction in a direct injection spark ignition engine - A CFD analysis. Energy 2015;81:361–72.

[48] Grimaldi CN, Battistoni M, Postrioti L. Flow Characterization of a high performance S.I. engine intake system - Part 1: experimental analysis. SAE Tech Paper 2003-01-0623; 2003

[49] Wang T, Liu D, Tan B, Wang G, Peng Z. An investigation into in-cylinder tumble flow characteristics with variable valve lift in a gasoline engine. Flow Turbul Combust 2014;94:285–304.

[50] Angelberger C, Poinsot T, Delhay, B. Improving near-wall combustion and wall heat transfer modeling in SI engine computations. SAE Tech Paper 972881; 1997.

[51] Baratta M ,Misul D., Viglione L, “Turbulence and combustion modeling in a high-performance, high- CR NG engine”- ASME-ATI-UIT 2015 Conference on Thermal Energy Systems: Production, Storage, Utilization and the Environment 17 – 20 May, 2015, Napoli, Italy

[52] Best Practices Guide for I.C. Engines VERSION 4.20 - 2013 CD-adapco

[53] O. Colin, A. Benkenida and C. Angelberger -3d Modeling of Mixing, Ignition and Combustion Phenomena in Highly Stratified Gasoline Engines- Oil and Gas Science and Technology - Rev. IFP, 58 1 (2003) 47-62-DOI: https://doi.org/10.2516/ogst:2003004

[54] Gülder, O.L. 1990. ‘Turbulence premixed flame propagation models for different combustion regimes’, 23rd Symp. (Int.) on Combustion, The Combustion Institute, pp. 743-750

[55] Meneveau, C. and Poinsot, T. 1991. ‘Stretching and quenching of flamelets in premixed turbulent combustion’, Combust. Flame, 86,pp. 311-332.

[56] Brunt, M. and Emtage, A., "Evaluation of Burn Rate Routines and Analysis Errors," SAE Technical Paper 970037, 1997, doi:10.4271/970037.

[57] Mohammed SE et al. The effects of fuel-injection timing at medium injection pressure on the engine characteristics and emissions of a CNG-DI engine fueled by a small amount of hydrogen in CNG. Int J Hydrogen Energy 2011;36:11997-2006

[58] S.M. Prudhomme, H. Raj-Hariri. Investigation of supersonic underexpanded jets using adaptive unstructured finite elements

[59] FISER, Jan; JEDELSKY, Jan; VACHFORMAN, Tomas; FORMAN, Matej; JICHA, Miroslav. EPJ Web of Conferences; 2012, Issue 25, p01015-p.1

[60] Zhang, F.R., Okamoto, K., Morimoto, S. and Shoji, F., "Methods of increasing the BMEP (Power Output)for Natural Gas Spark Ignition Engines", SAE SP- 1371 ’Combustion Processes in Engines Utilizing Gaseous Fuels’, pp.11-19, 1998

[61] Douailler, B., Ravet, F., Delpech, V., Soleri, D. et al., “Direct Injection of CNG on High Compression Ratio Spark Ignition Engine: Numerical and Experimental Investigation,” SAE Technical Paper 2011-01-0923, 2011, doi:10.4271/2011-01-923.

[62] Baratta, M., Catania, A., Spessa, E., Herrmann, L. et al,. “Multi-Dimensional Modelling of Direct Natural-Gas Injection and Mixture Formation in a Stratified-Charge SI Engine with Centrally Mounted Injector,” SAE Int. J. Engines 1(1):607-626,2009, doi:10.4271/2008-01-0975.

[63] Baratta M. and Rapetto N., “Fluid-Dynamic and Numerical Aspects in the Simulation of Direct CNG Injection in Spark-Ignition Engines,” Computers and Fluids 103:215-233, 2014,doi:10.1016/j.compfluid.2014.07.028.